



**Max-Planck-Institut für Metallforschung**  
Stuttgart

---

## **Microstructural effects on stress in thin films**

Markus Albin Wohlschlägel

Dissertation  
an der  
**Universität Stuttgart**

---

Bericht Nr. 218  
September 2008









**Max-Planck-Institut für Metallforschung**  
Stuttgart

---

## **Microstructural effects on stress in thin films**

Markus Albin Wohlschlägel

Dissertation  
an der  
**Universität Stuttgart**

---

Bericht Nr. 218  
September 2008



# Microstructural effects on stress in thin films

Von der Fakultät Chemie der Universität Stuttgart  
zur Erlangung der Würde eines Doktors der Naturwissenschaften (Dr. rer. nat.)  
genehmigte Abhandlung

vorgelegt von

Markus Albin Wohlschlögel

aus Aschaffenburg

Hauptberichter:	Prof. Dr. Ir. E. J. Mittemeijer
Mitberichter:	Prof. Dr. F. Aldinger
Prüfungsvorsitzender:	Prof. Dr. E. Roduner

Tag der Einreichung:	23.06.2008
Tag der mündlichen Prüfung:	16.09.2008

MAX-PLANCK-INSTITUT FÜR METALLFORSCHUNG STUTTGART  
INSTITUT FÜR METALLKUNDE DER UNIVERSITÄT STUTTGART

Stuttgart, 2008





# Contents

<b>1. General introduction .....</b>	<b>9</b>
1.1. Global view and historical background.....	9
1.1.1. Technological relevance of thin films .....	9
1.1.2. Scientific relevance of thin film/layer systems .....	10
1.1.2.1. Thin film fabrication.....	10
1.1.2.2. Microstructure of thin films grown by deposition.....	11
1.1.2.3. Thin layers grown by gas nitriding of pure iron.....	11
1.1.2.4. Properties of thin film/layer systems; effects related to a nanocrystalline microstructure.....	16
1.2. Focus of the thesis .....	20
1.3. Methodology and interpretation strategies.....	20
1.4. Outline of the thesis.....	25
<b>2. Unexpected formation of <math>\epsilon</math> iron nitride by gas nitriding of nanocrystalline <math>\alpha</math>-Fe films.....</b>	<b>29</b>
2.1. Introduction .....	30
2.2. Experimental.....	30
2.3. Results and discussion.....	31
2.4. Conclusions .....	37
<b>3. Crystallite-size dependence of the coefficient of thermal expansion of metals .....</b>	<b>39</b>
3.1. Introduction .....	40
3.2. Experimental.....	41
3.3. Results and discussion.....	42
3.4. Conclusions .....	47

**4. Determination of depth gradients of grain interaction and stress in Cu thin films .....51**

4.1. Introduction ..... 52

4.2. Theoretical background ..... 53

4.2.1. Diffraction measurements at fixed penetration depth ..... 53

4.2.2. Refraction and surface-roughness effects..... 54

4.2.3. The  $f(\psi, hkl)$ -method; determination of effective grain interaction 55

4.3. Experimental..... 56

4.3.1. Specimen preparation ..... 56

4.3.2. Focused ion beam microscopy ..... 56

4.3.3. Surface topography..... 57

4.3.4. X-ray diffraction measurements ..... 57

4.4. Results and Discussion ..... 59

4.4.1. Grain morphology and film thickness ..... 59

4.4.2. Surface roughness ..... 60

4.4.3. Crystallographic texture ..... 60

4.4.4. Stresses and grain interaction as function of depth ..... 62

4.5. Conclusions ..... 68

**5. Residual stress and strain-free lattice-parameter depth profiles in a  $\gamma'$ -Fe<sub>4</sub>N<sub>1-x</sub> layer on an  $\alpha$ -Fe substrate measured by X-ray diffraction stress analysis at constant information depth .....73**

5.1. Introduction ..... 74

5.2. Theoretical background ..... 76

5.2.1. X-ray residual stress analysis (XRSA) ..... 76

5.2.2. Grain-interaction models ..... 77

5.2.3. Determination of real-space depth profiles from XRSA at constant penetration/information depth ..... 78

5.3. Experimental.....	80
5.3.1. Specimen preparation .....	80
5.3.2. Metallography.....	80
5.3.3. X-ray diffractometry.....	81
5.4. Results and discussion.....	82
5.4.1. Microstructure and phase analysis.....	82
5.4.2. Diffraction analysis at constant penetration depth .....	84
5.4.2.1. Lattice-parameter and nitrogen-concentration depth profiles.....	85
5.4.2.2. Residual stress depth profile.....	90
5.5. Conclusions .....	91
<b>6. Application of a single-reflection collimating multilayer optic for X-ray diffraction experiments employing parallel-beam geometry ..</b>	<b>97</b>
6.1. Introduction .....	99
6.2. Background.....	100
6.2.1. Geometry conventions.....	100
6.2.1.1. Frames of reference .....	100
6.2.1.2. Diffraction geometry .....	101
6.2.2. Instrumental aberrations in parallel-beam X-ray diffraction.....	102
6.2.2.1. Illuminated and detected areas .....	102
6.2.2.2. Defocusing.....	103
6.2.3. Functional principle of a single-reflection collimating X-ray mirror .....	103
6.2.3.1. Two dimensional beam shaping by mirror optics .....	104
6.2.3.2. Single-reflection mirrors .....	105
6.3. Ray-tracing simulations.....	106
6.4. Experimental.....	111
6.5. Experimental results and discussion .....	112
6.5.1. Beam divergence and beam shape.....	112
6.5.2. Primary beam intensity and brilliance .....	114

6.5.3. Instrumental effects in XRD experiments employing parallel-beam geometry .....	117
6.5.3.1. Peak shape .....	117
6.5.3.2. Peak intensity .....	119
6.6. Comparative discussion.....	120
6.6.1. Simulation versus experiment .....	120
6.6.2. X-ray mirrors versus X-ray lenses.....	120
6.7. Summary.....	123
<b>7. Kurzfassung der Dissertation in deutscher Sprache.....</b>	<b>127</b>
7.1. Einleitung .....	127
7.2. Unerwartete Bildung von $\epsilon$ -Eisennitrid beim Gasnitrieren nanokristalliner $\alpha$ -Fe-Schichten.....	127
7.3. Kristallitgrößenabhängigkeit des thermischen Ausdehnungskoeffizienten von Metallen.....	128
7.4. Bestimmung von Gradienten effektiver Kornwechselwirkung und Spannung in dünnen Cu-Schichten .....	130
7.5. Tiefenprofile von Eigenspannung und dehnungsfreiem Gitterparameter in einer $\gamma'$ -Fe <sub>4</sub> N <sub>1-x</sub> -Schicht .....	133
7.6. Anwendung einer kollimierenden Einfachreflektions-Multilagenoptik für Röntgenbeugungsexperimente in Parallelstrahlgeometrie.....	135
<b>8. Summary.....</b>	<b>137</b>
8.1. Introduction .....	137
8.2. Unexpected formation of $\epsilon$ -iron nitride by gas nitriding of nanocrystalline $\alpha$ -Fe films .....	137

8.3. Crystallite-size dependence of the coefficient of thermal expansion of metals .....	138
8.4. Determination of gradients of effective grain interaction and stress in Cu thin films .....	140
8.5. Residual stress and strain-free lattice parameter depth profiles in a $\gamma'$ -Fe <sub>4</sub> N <sub>1-x</sub> -layer .....	142
8.6. Application of a collimating single reflection multilayer optic for X-ray diffraction experiments in parallel-beam geometry .....	144



# 1. General introduction

## 1.1. Global view and historical background

### 1.1.1. Technological relevance of thin films

Miniaturisation is one of the key issues of today's technology and thin films are a vital part of it. The rapid development of highly integrated electronic devices is a direct result of the substantial progress in thin film research which has led to a spectrum of applications ranging from conductor paths to compound semiconductor epitaxial thin film structures.

Moreover, thin films are essential components of many micro-electro-mechanical systems, where they serve as sensors or actuators. For instance, piezoelectric or piezoresistive thin films deposited on a silicon membrane are employed to detect a deflection of this membrane as a result of a pressure change electronically. Such a device can be used as a microphone in hearing aids [1].

Other major fields of application of thin films are coatings for optical, decorative, environmental or wear resistant use. As application examples anti-reflective coatings for camera lenses and glasses, metallic coatings for the creation of shiny surfaces, thermal barrier coatings in gas turbine engines and titanium nitride wear-protective coatings for tools are mentioned here.

Thin film technology is, however, not employed as recently as in the industrialised age: Already in ancient Egypt thin film coatings made of hammered gold were used for ornamentation and protection purposes: Gold leaf coatings from Luxor dating to the 18<sup>th</sup> dynasty (1567 – 1320 B.C.) exhibited thicknesses in the range of a few 100 nm's [2].

### 1.1.2. Scientific relevance of thin film/layer systems

Many actual applications of thin film systems are the result of fundamental research activities dealing with their fabrication as well as their interesting properties which can significantly differ from those of bulk materials.

#### 1.1.2.1. Thin film fabrication

Two major thin film fabrication procedures are physical vapour deposition (PVD) and chemical vapour deposition (CVD). Whereas PVD-processes rely on the transfer of condensed matter into the gas phase by physical mechanisms as evaporation or sputtering, CVD-processes are characterized by the chemical reaction of a volatile compound of a material to be deposited with other compounds in the gas phase to produce a non-volatile solid which then deposits on a suitably placed substrate [3]. The earliest experiments on PVD-processes date back to the 19<sup>th</sup> century: In 1852 Grove found metal deposits which were sputtered from a cathode as a result of a glow discharge plasma [4] and in 1857 Faraday evaporated thin films while he was experimenting with exploding metal wires in an inert atmosphere [5]. Because of the fact that CVD-processes do not require vacuum or exceptional amounts of electric power they were commercially employed earlier than PVD-processes. Thus, already at the end of the 19<sup>th</sup> century CVD-processes were employed to deposit protective refractory metal coatings onto carbon wires which were used as illuminants in electric lamps at that time [6]. For more details on thin film deposition techniques the reader is referred to the book of Ohring [3].

Apart from deposition (i.e. creating a thin film structure on a usually much thicker substrate) thin layers on thick substrates can also be generated by reactions and phase transformations at surfaces. As an example the reaction of iron with nitrogen to form iron nitrides is mentioned here, as it plays an important role in this work. In this context nitrogen is provided by a mixture of ammonia and hydrogen in the gas phase which is referred to as gas- or gaseous nitriding [7]. One major difference to thin film deposition techniques is that in the case of nitriding the thin layer grows *into* the substrate, whereas the result of a PVD- or CVD-process is a thin film structure grown *onto* a substrate.



### **1.1.2.2. Microstructure of thin films grown by deposition**

The microstructure of thin films deposited onto a substrate as well as that of thin layers grown into a substrate has been studied extensively as its features affect the mechanical behaviour of the films and the layers, respectively.

For deposited thin films the results of these works are structure-zone models describing the film microstructure as function of various deposition parameters. For the case of deposited thin films the scope will be limited to the PVD-processes sputtering and evaporation as they constitute the deposition techniques employed in this work. The earliest structure-zone model has been devised by Movchan and Demchishin in 1969 based on experimental investigations on thick evaporated metal and oxide coatings with various thicknesses [8]. Eight years later Thornton proposed a four-zone model describing the microstructure of sputtered thin films as a function of working gas pressure and substrate temperature [9]. More sophisticated structure-zone models have been developed since then conducting a systematic study of several evaporated elemental films with constant thickness [10] and taking into account the effect of ion bombardment in sputtered thin films [11].

### **1.1.2.3. Thin layers grown by gas nitriding of pure iron**

Due its technological importance as hardening mechanism for steel, gas nitriding and the microstructure of nitrided iron have also been investigated extensively (see, for example Refs. [7,12,13] and references therein). Depending on nitriding temperature and composition of the nitriding gas atmosphere, and thus the activity of nitrogen in the gas phase, quantified by the nitriding potential (for details see below and, for example, [12]), compound layers composed of different phases can develop and/or nitrogen can react with iron forming iron nitride precipitates and can be interstitially dissolved in the iron matrix building a diffusion zone (see Figure 1.1). The compound layer is characterised by enhanced hardness and resistance to corrosion and wear, whereas the diffusion zone improves the fatigue properties of the nitrided workpiece [7].

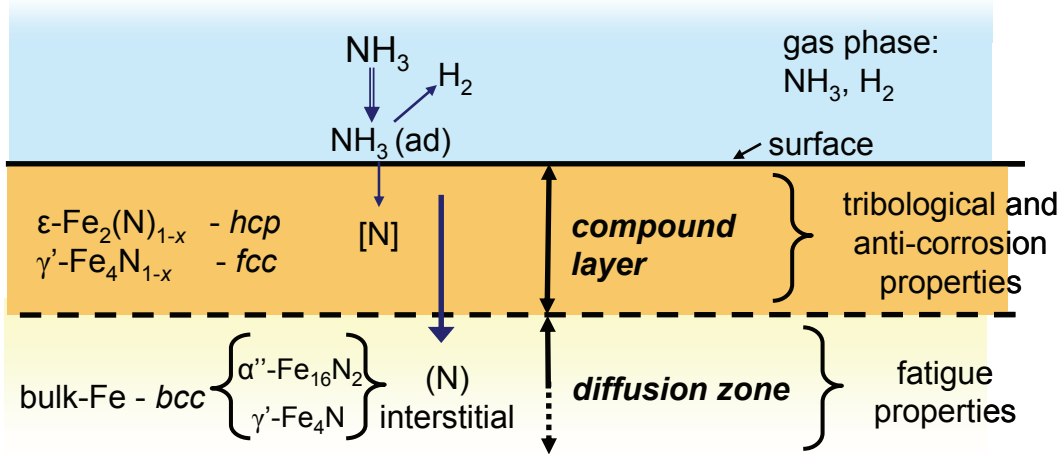
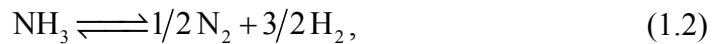
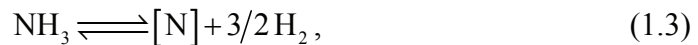


**Figure 1.1.** Schematic representation of the development of compound layer and diffusion zone as a result of gas nitriding of pure iron. Ammonia provided by an ammonia/hydrogen mixture in the gas phase is adsorbed at the surface of the workpiece and subsequently dissociates into atomic nitrogen ([N]) and hydrogen. By inward diffusion nitrogen reacts with iron forming a compound layer composed of iron nitrides and/or a diffusion zone, where iron nitride precipitates as well as interstitially dissolved nitrogen compose the diffusion zone.

A direct reaction of iron with nitrogen to form iron nitrides is thermodynamically unfavourable at atmospheric pressure. A reaction of iron with ammonia to form iron nitrides, however, produces at 773 K and  $10^{-5}$  Pa a release of Gibbs free energy of about 20 kJ/mol [12]. Thus, in typical gas nitriding processes temperatures between 700 and 860 K and atmospheric pressures are applied to form iron nitrides. The (hypothetical) chemical reactions taking place during the gas nitriding treatment of pure iron can be summarized as follows:



resulting in



where [N] denotes atomic nitrogen dissolved in the ferrite matrix.

Due to the equality of the chemical potentials of nitrogen in the gas and in the solid phase and as a consequence of thermodynamic equilibrium it follows for the nitrogen activity,  $a_N$ , in the solid at the solid/gas interface:

$$a_{\text{N}} = (p_{\text{N}_2}^0)^{-1/2} K \left( \frac{p_{\text{NH}_3}}{p_{\text{H}_2}^{3/2}} \right), \quad (1.4)$$

where  $p_{\text{N}_2}^0$  denotes the reference pressure (1 atm) of the (hypothetical) nitrogen gas as present in equations (1.1) and (1.2),  $K$  is the equilibrium constant for equation (1.2) and  $p_i$  are the partial pressures of the constituents of the nitriding gas atmosphere. This ratio of partial pressures is called the nitriding potential,  $r_{\text{N}}$ :

$$r_{\text{N}} \equiv \frac{p_{\text{NH}_3}}{p_{\text{H}_2}^{3/2}}. \quad (1.5)$$

From equations (1.4) and (1.5) it is clear that the nitriding potential is directly proportional to the activity (and thus to the chemical potential) of nitrogen in the gas phase. Besides temperature the nitriding potential therefore serves as a crucial parameter controlling the nitriding process. The binary system Fe-N can thus not only be represented by the conventional phase diagram (see Figure 1.3), but by a modified phase diagram, where the phase fields are drawn as function of temperature and nitriding potential, which is known as the Lehrer diagram [14] (see Figure 1.2).

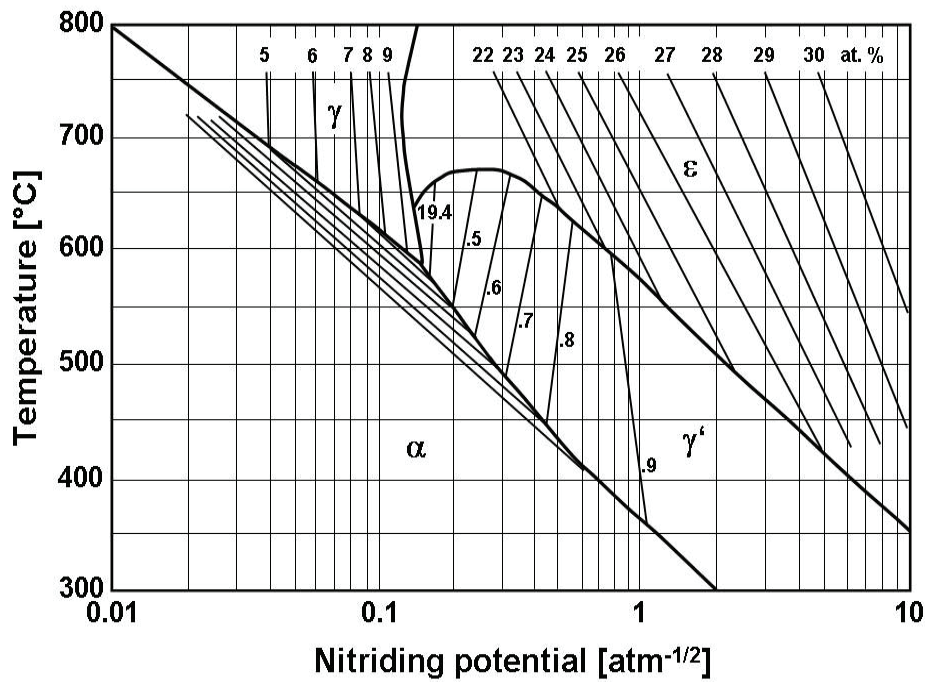


**Figure 1.2.** Lehrer diagram for gas nitriding of pure iron, including nitrogen iso-concentration lines in at.% (redrawn after [15]). Depending on nitriding temperature and nitriding potential nitrogen can either be interstitially dissolved in ferrite ( $\alpha$ ) or austenite ( $\gamma$ ) building the diffusion zone, or  $\gamma'$  and/or  $\epsilon$  iron nitrides are formed constituting the compound layer.

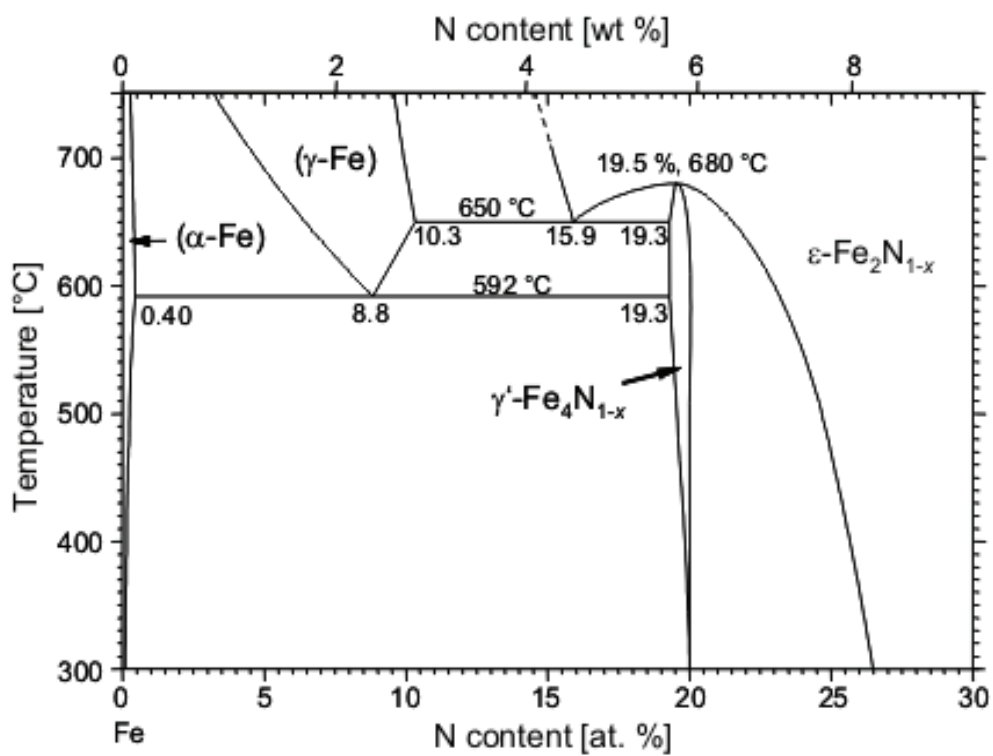


**Figure 1.3.** Section of the metastable Fe-N phase diagram (redrawn after [16]).

The maximum solubility of nitrogen in ferrite is as low as 0.4 at.% and it is reached at a temperature of 865 K. At this temperature ferrite is in equilibrium with  $\gamma'$  iron-nitride ( $\gamma'$ -Fe<sub>4</sub>N<sub>1-x</sub>). The homogeneity range of  $\gamma'$  Fe<sub>4</sub>N<sub>1-x</sub> is quite low with nitrogen concentrations ranging from 19.3 to 20 at.%. Its crystal structure (see Figure 1.4 left) consists of a face-centered cubic (fcc) arrangement of iron atoms with the nitrogen atoms occupying octahedral interstitial sites [17,18]. At larger nitrogen concentrations the phase  $\epsilon$  iron-nitride ( $\epsilon$ -Fe<sub>2</sub>N<sub>1-x</sub>) exists. This phase is characterized by a wide homogeneity range extending for example at 823 K from 24.05 at.% nitrogen up to almost 33 at.% nitrogen. Its crystal structure (see Figure 1.4 right) is composed of a hexagonally close-packed (hcp) arrangement of the iron atoms with the nitrogen atoms again occupying octahedral interstitial sites [17,18]. In both iron nitride phases the nitrogen atoms are arranged maintaining a long-range ordering [17-22]. Their lattice parameters show a significant variation with nitrogen concentration [23-25].

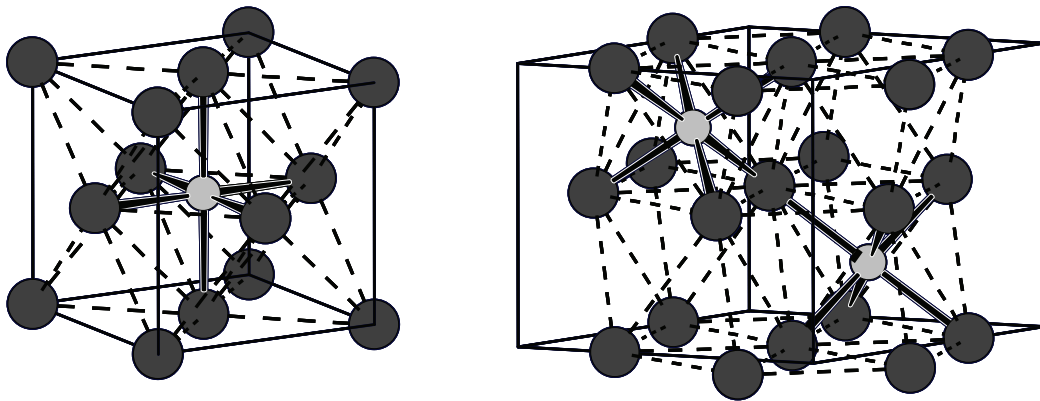


**Figure 1.4.** Crystal structures of  $\gamma'$ -Fe<sub>4</sub>N<sub>1-x</sub> (left) and  $\epsilon$ -Fe<sub>2</sub>N<sub>1-x</sub> (right). The dark grey spheres represent the iron atoms and the light grey spheres denote the nitrogen atoms. Fe-Fe bonds are drawn by dashed lines and Fe-N bonds are represented by solid bold lines.

The effect on thermodynamics of the Fe-N system in case of a nanocrystalline microstructure is investigated in chapter 2. Furthermore, iron-nitride layers exhibit complicated stress depth profiles which are investigated in chapter 5.

#### **1.1.2.4. Properties of thin film/layer systems; effects related to a nanocrystalline microstructure**

The properties of materials are directly related to their microstructure. As far as thin films are concerned, they generally exhibit mechanical residual stresses [26]. The magnitude of residual stresses can be very high, even exceeding the yield stress of the corresponding bulk material considerably [27,28]. Residual stresses can be created by various sources: Thermal residual stresses are built up as a consequence of the difference of the coefficients of thermal expansion (CTEs) of film and substrate, respectively, when the film is deposited at non-ambient temperature [29]. Additionally, intrinsic residual stresses occur as a result of lattice parameter mismatch [29], crystallite coalescence [30], densification [29], sputtering gas pressure [31,32], variation of interatomic spacing with crystallite size [33], recrystallization [34], void networks between columnar grains [35] and phase transformations during deposition [33].

Residual stresses can be beneficial or detrimental for the material or workpiece affected by them: For workpieces significantly affected by friction and wear compressive residual stresses in the surface region are an advantage as they prevent crack formation and propagation. For this reason various techniques have been developed to maximize the compressive residual stress close to the surface of a wear-affected workpiece such as (i) shot-peening, (ii) case hardening by nitriding or nitrocarburizing or (iii) the deposition of wear-resistant coatings. All methods rely on an increase of the specific volume of the surface region, thus leading to compressive stresses. In the first case, compressive stresses are introduced by plastic deformation of the surface, thus increasing the number of defects, in the second case by inward diffusion of interstitials (as nitrogen and carbon, respectively), and in the third case compressive stresses are created by deposition of coatings of a different material exhibiting a larger specific volume than the substrate material.

Compressive stresses can be on the other hand also detrimental, particularly for coatings or thin films in general, as they may lead to delamination if their magnitude gets too large. Tensile stresses close to the surface are in most cases a disadvantage as they can lead to an enhancement of crack formation and growth and thus to a reduced fatigue strength.

Another consequence of its microstructure is the type of elastic grain interaction within a thin film. Generally, each crystallite in a polycrystalline thin film behaves elastically anisotropic (as an exception to this rule tungsten is mentioned here as an example – in case of tungsten each crystallite behaves elastically isotropic). The mechanical stress state of a polycrystal composed of elastically anisotropic crystallites then results from the type of elastic grain interaction acting within the polycrystal. If the polycrystal consists of a sufficient number of crystallites, all crystallites are oriented randomly (i.e. in the absence of crystallographic texture) and direction-dependent grain interaction does not occur, the whole body can still behave elastically isotropic, which is generally referred to as ‘quasi-isotropy’ [36]. For quasi-isotropic specimens the Voigt [37] and Reuss [38] models represent the bounds for the mechanical elastical properties as well as the limits within which elastic grain interaction occurs. In the Voigt model it is assumed that in a polycrystal subject to a stress state all crystallites have the same strain whereas the Reuss model involves the assumption that all crystallites have the same stress. Neither of both models is compatible with reality as the adoption of the Voigt model leads to stress discontinuities and the application of the Reuss model leads to strain discontinuities at grain boundaries, respectively. A good approximation of the real elastic behaviour of a quasi-isotropic polycrystal is the Neerfeld-Hill model [39,40] which is characterized by arithmetic averaging of the grain interaction according to the Voigt and Reuss models. If a specimen features crystallographic texture, the orientation distribution of the crystallites, quantified by the orientation distribution function, has to be included in the grain-interaction model applied [36,41]. If a specimen exhibits direction dependent grain interaction [42] due to either morphological texture [43] or surface anisotropy [44] or combinations of them, other, more sophisticated grain interaction models have to be adopted.

Neither residual stress nor elastic grain interaction in thin films or layers are generally constant over the film/layer thickness. Residual stress gradients occur for example as a consequence of a variation of the lattice parameter with depth due to a concentration gradient or as a result of a variation of deposition parameters during film growth. Moreover, even if a stress gradient is not introduced intentionally, a decrease of residual stress generally occurs close to the surface due to surface relaxation mechanisms. The analysis of such gradients forms a focal point of this thesis.

Gradients of elastic grain interaction occur as a consequence of the fabrication technique and the resulting microstructure of the thin film or layer. If a thin film is deposited onto a thick substrate it often exhibits a rather columnar microstructure (see, for example Ref. [9]), whereas a layer grown into a substrate as the result of a phase transformation as in the case of gas nitriding exhibits a more globular microstructure. The grain boundaries in sputter-deposited thin films are conceived to have a rather open, voided structure in the vicinity of the film surface [3] which leads to the conclusion that crystallites can deform more freely and thus should have rather equal stress than equal strain leading to Reuss-type grain interaction near the surface (see Figure 1.5, top). At the film/substrate interface the film is conceived to be firmly attached to the substrate, which, particularly as a consequence of thermal stresses, leads to the assumption of equally-strained crystallites and thus to Voigt-type grain interaction close to the film/substrate interface. For an iron nitride layer on an iron substrate this situation can be quite different: As the layer grows into the ground and polished substrate as a result of a phase transformation it will develop an interface to the substrate exhibiting a certain roughness. Provided that the substrate exhibits a larger compliance than the layer, crystallites within the layer which contribute to this roughness can adapt the stress of the neighbouring crystallites by individual deformation towards the substrate, leading to a more Reuss-type of grain interaction at the interface layer/substrate. The crystallites near the surface on the other hand can be regarded as dense without exhibiting any voided structure (see above), separated by grain boundaries which are oriented more or less perpendicular to the specimen surface and the thermal strain imposed on them as a result of layer fabrication can be estimated equal for all crystallites (if layer and substrate have a cubic crystal structure the thermal expansion is isotropic). Thus, in this case a rather Voigt-like type of grain interaction is expected close to the surface (see Figure 1.5, bottom).



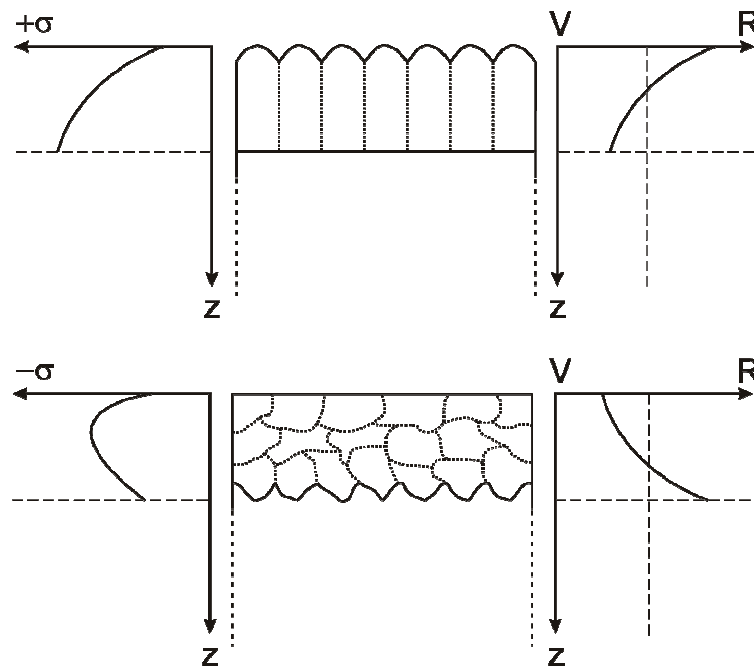


**Figure 1.5.** Different gradients of residual stress (left) and elastic grain interaction (right, V: Voigt, R: Reuss; the vertical dashed line denotes the arithmetic average grain interaction between Voigt and Reuss, known as the Neerfeld-Hill model) occurring as a result of different film/layer fabrication techniques. Top: Thin film deposited onto a thick substrate, bottom: thin layer grown into a thick substrate.

The microstructure of a specimen exhibiting an average crystallite size in the nanometre-range is generally referred to as ‘nanocrystalline’. The thermodynamics of nanocrystalline materials differ from those of bulk materials as surface contributions to thermodynamic quantities play an increased role compared to bulk contributions. As a consequence, for example the Gibbs free energy of a nanocrystalline material can be increased due to the surface curvature of the crystallites – an effect which is known as the Gibbs-Thompson effect [45]. This may even lead to phase equilibria deviating from those predicted by bulk thermodynamics. Another physical property which is influenced by crystallite size is the CTE. Theoretical works have found that the CTE should increase with decreasing crystallite size; experimental studies on this subject however have resulted in different, mutually contradicting findings (for details see chapter 3 and references therein).

## 1.2. Focus of the thesis

The contribution of this thesis concentrates on providing understanding of (i) thermal and chemical effects of a nanocrystalline microstructure, as in thin films and (ii) the development of gradients of stress and grain interaction in thin films.

Effects resulting from a nanocrystalline microstructure on phase formation in the system Fe-N and on the CTE of metals have been studied in detail. The Gibbs-Thompson-effect has been found to be responsible for the unexpected formation of  $\epsilon$  iron nitride during gas nitriding of nanocrystalline iron thin films and theoretical findings concerning the CTE of nanocrystalline materials could be proven conclusively.

Depth profiles of residual stress and effective grain interaction have been studied for a sputter-deposited Cu thin film, where the deposition parameters have been changed during film fabrication, and for a  $\gamma'$  iron nitride layer grown on top of an  $\alpha$  iron substrate obtained by gas nitriding. In case of the Cu thin film specimen the influence of the specimen surface roughness on the refraction of the incident beam has been studied and errors for residual stress values and grain interaction parameters related to the application of a refraction correction [46] in connection with the surface roughness have been identified. For the  $\gamma'$  iron nitride layer the variation of nitrogen concentration with depth could be elaborated successfully by separating the effect of residual stress on the  $\gamma'$  lattice parameter at each penetration depth and utilizing a relationship between the  $\gamma'$  lattice parameter and the nitrogen concentration from literature [23]. By an indirect method it was also possible to estimate the variation of elastic grain interaction over the layer thickness. Furthermore, real-space depth profiles were determined from measured Laplace-space depth profiles.

## 1.3. Methodology and interpretation strategies

In order to study microstructural effects on stress in thin films it is desirable to adopt an approach capable of studying several features of thin films simultaneously and, preferably, non-destructively. For this reason, X-ray diffraction (XRD) complemented by focused ion beam (FIB) microscopy were selected as most appropriate choice. XRD allows phase identification as well as the determination of lattice parameters crystallite size, microstrain, crystallographic texture, lattice strain and thus residual

stress at the same time without destroying the sample and FIB microscopy serves as suitable additional technique as selected microstructural results from XRD can be conveniently complemented. For a detailed work on the methodology of the diffraction analysis of the microstructure of materials the reader is referred to the book of Mittemeijer & Scardi [47].

The FIB method offers the advantage that the microstructure of thin films can be prepared firstly by cutting a cross section employing a focused Ga-ion beam and afterwards visualized using secondary electrons excited by the same ion beam (but with a much smaller current).

To perform temperature-dependent in-situ analyses on the one hand and to investigate gradients of residual stress, lattice parameter and grain interaction on the other hand using XRD it is essential to perform fast measurements (for in-situ analyses) and to employ a beam with a well-defined incidence angle (for maintaining a constant penetration depth; for details, see Ref. [48]), respectively. For this reason the XRD analyses concerned with these topics have been performed using a parallel-beam laboratory diffractometer, equipped with a copper rotating anode X-ray source, collimating X-ray mirror, Eulerian cradle, parallel plate collimator and scintillation counter, which has been characterized in detail in chapter 6 of this work (see Figure 1.6) and two synchrotron beamlines (for details see chapter 4 and chapter 5). For temperature-dependent in-situ measurements a commercially available heating/cooling chamber was mounted on the sample stage of the laboratory diffractometer (for details see chapter 3).

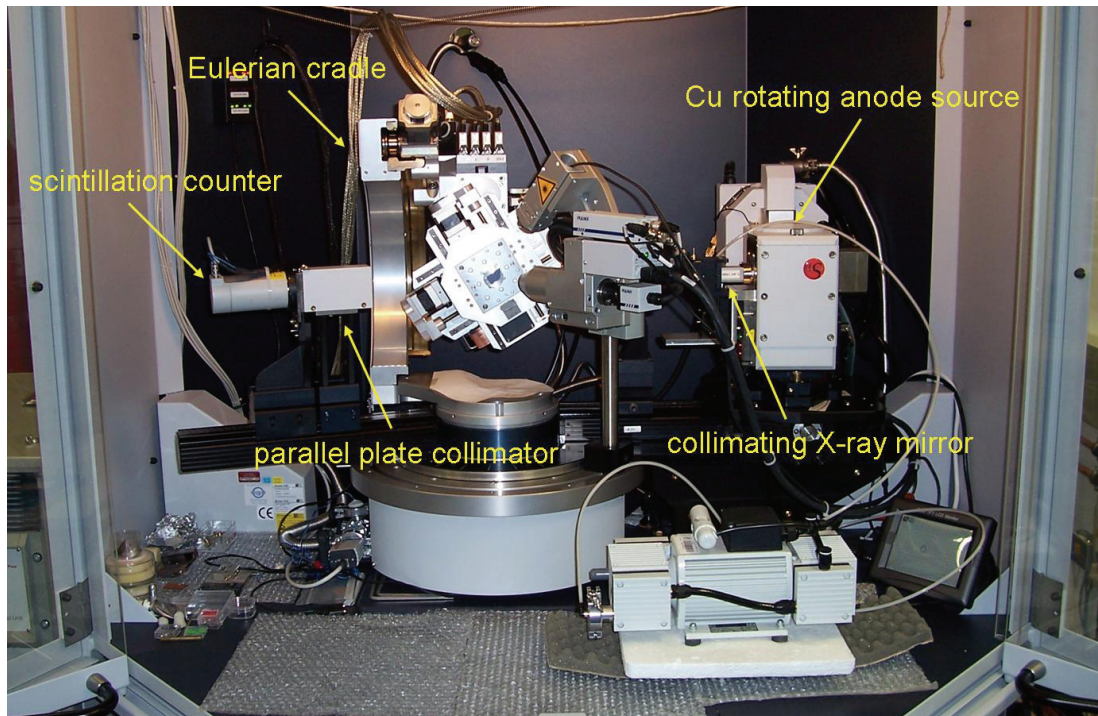


**Figure 1.6.** Laboratory diffractometer employed for in-situ and depth-dependent XRD measurements.

In-situ cooling experiments have been found mandatory for the determination of the CTE of nanocrystalline metal thin films as it is thus possible to exclude thermally activated processes like grain growth or defect annihilation which have been identified as actually affecting the CTE.

The determination of residual stresses, lattice parameters and elastic grain interaction has been carried out using dedicated analyses like the  $\sin^2\psi$ -method [36,41,49-51] and the  $f(\psi, hkl)$ -method [36,52,53]. These methods in principal allow the full assessment of the mechanical stress state of a sample from the spacing of one or more families of lattice planes  $hkl$  measured by XRD at various angles  $\psi$  and  $\varphi$  describing the orientation (tilt and rotation, respectively) of the diffraction vector with respect to the specimen frame of reference (for details see also Ref. [36]). As a prerequisite for the determination of mechanical stresses from measured lattice strains of a polycrystalline sample, suitable elastic constants for the material under investigation have to be known. These can be either determined experimentally by applying a known load to a specimen with known stress and measuring the thus resulting lattice strain or by calculation from single-crystal elastic constants adopting a suitable grain-interaction model (see, for example Refs. [36,41,49,51] and references therein).

The determination of gradients of residual stress, lattice parameter and elastic grain interaction has been realized by XRD measurements at constant penetration depth (for details see Ref. [48]). Adopting this method it is possible to obtain the above-mentioned gradients within the limit given by the X-ray absorption coefficient of the material under investigation. To increase the accessible depth-range it is necessary to vary the X-ray wavelength, e.g. by using a synchrotron beamline. Due to the exponential attenuation of the radiation within the investigated material (see Figure 1.7) it is practical to define two different measures in Laplace-space for the investigated real-space specimen depth  $z$ : The penetration depth  $\tau$  is defined as the centre of gravity of the distribution of diffracted intensity versus specimen depth  $z$  for an infinitely thick specimen. It is fully determined by the incident and diffracted beam angles and by the linear absorption coefficient of the material under investigation. About 63 % of the total diffracted intensity stem from a specimen volume confined by  $\tau$ . Equivalent to the penetration depth  $\tau$  is the information depth  $\xi$ , valid for finite specimen thickness, which is obtained by weighing each depth  $z$  with an absorption factor denoting an intensity reduction due to absorption of the diffracted signal from depth  $z$ . It has to be noted that  $\xi$  is always smaller than  $\tau$ . For a small value of  $\tau$  compared to the specimen thickness,  $\xi$  is almost equal  $\tau$  and the value of  $\xi$  approaches the limit of half of the specimen thickness for a value of  $\tau$  much larger than the specimen thickness. For more details on these quantities, see Refs. [48,54].

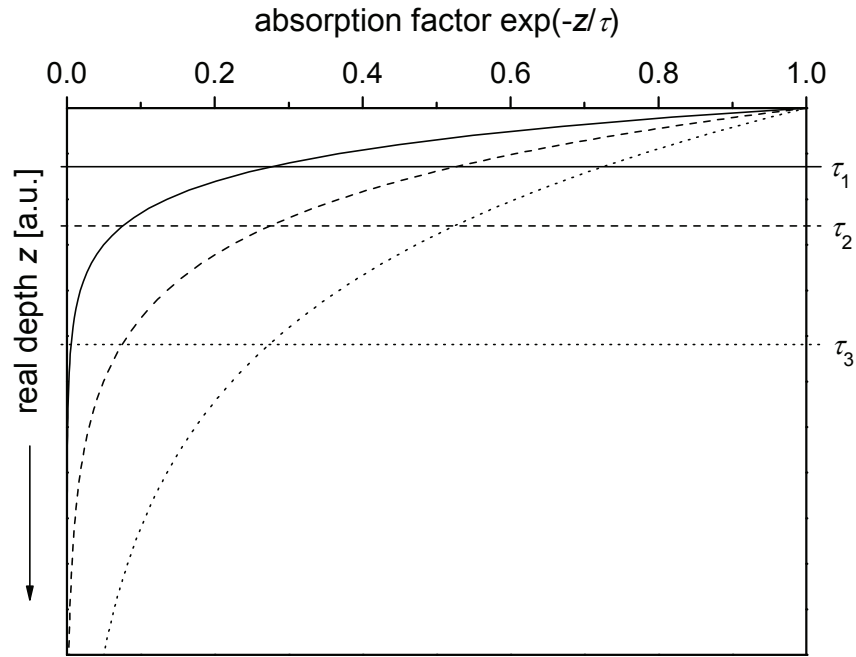


**Figure 1.7.** Intensity reduction due to absorption within the material under investigation. The straight, dashed and dotted lines belong to different penetration depths,  $\tau_1$ ,  $\tau_2$ ,  $\tau_3$ , respectively. It holds:  $\tau_1 < \tau_2 < \tau_3$ .

As a result of the XRD analysis at constant penetration depth, Laplace-space gradients of residual stress, lattice parameter and elastic grain interaction are obtained. In order to transform the measured gradients into real space an inverse Laplace-transformation has to be performed in principle, which however cannot be carried out directly in most cases. On the other hand it is straightforward to apply a Laplace-transformation to any real-space gradient. Thus, in this work the following method has been adopted: A real-space gradient described by a cubic spline interpolation through supporting nodes distributed in the real-space regime of interest is assumed. Subsequently, the real-space gradient is Laplace-transformed and compared with the measured Laplace-gradient. By least-squares minimization of the difference between measured and calculated Laplace-gradient the true real-space gradient is approximated. In order to arrive at an as realistic as possible description of the real-space gradient, penalty functions are imposed on the cubic spline interpolation of the assumed real-space gradient to avoid oscillatory disturbances of the real-space gradient.

## 1.4. Outline of the thesis

This thesis is divided in three principal parts: In the first part, the microstructure of nanocrystalline thin films and its effect on their thermodynamic and thermal properties is investigated. It has been found that phase transformations within nanocrystalline materials as well as their CTE of can be considerably different from the according bulk properties (see chapter 2 and chapter 3, respectively). The second part deals with grain interaction gradients and their effect on residual stress gradients. In chapter 4 the corresponding gradients in a copper thin film, where the deposition conditions have been changed during film fabrication, have been measured by XRD analysis at constant penetration depth making use of the  $f(\psi, hkl)$ -method. In chapter 5 depth profiles of residual stress, strain-free lattice parameter and elastic grain interaction in a  $\gamma'$  iron nitride layer grown on top of an  $\alpha$  iron substrate have been analyzed by XRD measurements at constant penetration depth employing the  $\sin^2\psi$  method. The third part of the thesis constitutes the characterization of the parallel-beam laboratory diffractometer which has been applied in all laboratory XRD measurements at constant penetration depth (chapter 6).

## References

- [1] Freund, L.B. & Suresh, S. (2006). *Thin Film Materials - Stress, Defect Formation and Surface Evolution*. Cambridge, UK: University Press.
- [2] Nicholson, E.D. (1979). *Gold Bull.* **12**, 161.
- [3] Ohring, M. (2002). *The Materials Science of Thin Films*. New York: Academic Press.
- [4] Grove, W.R. (1852). *Philos. Trans. R. Soc. London, A* **142**, 87.
- [5] Faraday, M. (1857). *Philos. Trans. R. Soc. London, A* **147**, 145.
- [6] Sherwood, E.M. & Blocher Jr., J.M. (1965). *J. Metals* **17**, 594.
- [7] Knerr, C.H., Rose, T.C. & Filkowski, J.H. (1991). *Gas Nitriding*, in: *ASM Handbook*, edited by S. R. Lampman & T. B. Zorc, Vol. 4, pp. 387. ASM.
- [8] Movchan, B.A. & Demchishin, A.M. (1969). *Fiz. Met. Metalloved.* **28**, 653.
- [9] Thornton, J.A. (1977). *Annu. Rev. Mater. Sci.* **7**, 239.
- [10] Hentzell, H.T.G., Grovenor, C.R.M. & Smith, D.A. (1984). *J. Vac. Sci. Technol. A* **2**, 218.
- [11] Messier, R., Giri, A.P. & Roy, R. (1984). *J. Vac. Sci. Technol. A* **2**, 500.
- [12] Mittemeijer, E.J. & Somers, M.A.J. (1997). *Surf. Eng.* **13**, 483.
- [13] Colijn, P.F., Mittemeijer, E.J. & Rozendaal, H.C.F. (1983). *Z. Metallkd.* **74**, 620.
- [14] Lehrer, E. (1930). *Z. Elektrochem.* **36**, 383.
- [15] Hoffmann, R. (1996). *Härtereitech. Mitt.* **51**, 5.
- [16] Wriedt, H.A., Gokcen, N.A. & Nafziger, R.H. (1987). *Bull. Alloy Phase Diagr.* **8**, 355.
- [17] Jack, K.H. (1948). *Proc. R. Soc. London, A* **195**, 34.
- [18] Jacobs, H., Rechenbach, D. & Zachwieja, U. (1995). *J. Alloys Compd.* **227**, 10.
- [19] Jack, K.H. (1952). *Acta Cryst.* **5**, 404.
- [20] Kooi, B.J., Somers, M.A.J. & Mittemeijer, E.J. (1996). *Metall. Mater. Trans. A* **27A**, 1063.
- [21] Leineweber, A. & Jacobs, H. (2000). *J. Alloys Compd.* **308**, 178.
- [22] Leineweber, A., Jacobs, H., Hüning, F., Lueken, H. & Kockelmann, W. (2001). *J. Alloys Compd.* **316**, 21.



- [23] Somers, M.A.J., van der Pers, N.M., Schalkoord, D. & Mittemeijer, E.J. (1989). *Metall. Trans. A* **20A**, 1533.
- [24] Somers, M.A.J., Kooi, B.J., Maldzinski, L., Mittemeijer, E.J., van der Horst, A.A., van der Kraan, A.M. & van der Pers, N.M. (1997). *Acta Mater.* **45**, 2013.
- [25] Liapina, T., Leineweber, A., Mittemeijer, E.J. & Kockelmann, W. (2004). *Acta Mater.* **52**, 173.
- [26] Janssen, G.C.A.M. (2007). *Thin Solid Films* **515**, 6654.
- [27] Arzt, E. (1998). *Acta Mater.* **46**, 5611.
- [28] Balk, T. J., Dehm, G. & Arzt, E. (2003). *Acta Mater.* **51**, 4471.
- [29] Nix, W. D. (1989). *Metall. Trans. A* **20A**, 2217.
- [30] Hoffman, R.W. (1976). *Thin Solid Films* **34**, 185.
- [31] Hoffman, D.W. & Thornton, J.A. (1982). *J. Vac. Sci. Technol.* **20**, 355.
- [32] Hoffman, D.W. (1994). *J. Vac. Sci. Technol. A* **12**, 953.
- [33] Koch, R. (1994). *J. Phys.: Condens. Matter* **6**, 9519.
- [34] Doerner, M. F. & Nix, W. D. (1988). *Crit. Rev. Solid State* **14**, 225.
- [35] Windischmann, H. (1992). *Crit. Rev. Solid State* **17**, 547.
- [36] Welzel, U., Ligot, J., Lamparter, P., Vermeulen, A.C. & Mittemeijer, E.J. (2005). *J. Appl. Cryst.* **38**, 1.
- [37] Voigt, W. (1910). *Lehrbuch der Kristallphysik*. Leipzig: Teubner.
- [38] Reuss, A. (1929). *Z. Angew. Math. Mech.* **9**, 49.
- [39] Neerfeld, H. (1942). *Mitt. K.-Wilh.-Inst. Eisenforsch.* **24**, 61.
- [40] Hill, R. (1952). *P. Phys. Soc. Lond. A* **65**, 349.
- [41] Hauk, V. (1997). Editors. *Structural and Residual Stress Analysis by Nondestructive Methods*, Amsterdam: Elsevier.
- [42] Welzel, U. & Mittemeijer, E.J. (2003). *J. Appl. Phys.* **93**, 9001.
- [43] Koch, N., Welzel, U., Wern, H. & Mittemeijer, E.J. (2004). *Philos. Mag.* **84**, 3547.
- [44] Welzel, U., Leoni, M. & Mittemeijer, E. J. (2003). *Philos. Mag.* **83**, 603.
- [45] Porter, D.A. & Easterling, K.E. (2001). *Phase Transformations in Metals and Alloys*. Cheltenham, UK: Nelson Thornes.
- [46] Genzel, C. (2005). *Mater. Sci. Technol.* **21**, 10.
- [47] Mittemeijer, E.J. & Scardi, P. (2004). Editors. *Diffraction Analysis of the Microstructure of Materials*, Berlin: Springer.

- 
- [48] Kumar, A., Welzel, U. & Mittemeijer, E. J. (2006). *J. Appl. Cryst.* **39**, 633.
- [49] Noyan, I. C., Huang, T. C. & York, B. R. (1995). *Crit. Rev. Solid State* **20**, 125.
- [50] Macherauch, E. & Müller, P. (1961). *Z. Angew. Physik* **13**, 305.
- [51] Noyan, I.C. & Cohen, J.B. (1987). *Residual Stress: Measurements by Diffraction and Interpretation*. New York: Springer.
- [52] Kamminga, J.-D., de Keijser, Th. H., Mittemeijer, E.J. & Delhez, R. (2000). *J. Appl. Cryst.* **33**, 1059.
- [53] Quaeys, C., Knuyt, G. & Stals, L. M. (1995). *Surf. Coat. Technol.* **74-75**, 104.
- [54] Delhez, R., de Keijser, Th. H. & Mittemeijer, E. J. (1987). *Surf. Eng.* **3**, 331.

## 2. Unexpected formation of $\epsilon$ iron nitride by gas nitriding of nanocrystalline $\alpha$ -Fe films

*M. Wohlschlägel, U. Welzel and E.J. Mittemeijer*

### **Abstract**

Polycrystalline iron thin films exhibiting different crystallite sizes, which were deposited on  $\alpha$ -Al<sub>2</sub>O<sub>3</sub> substrates by molecular beam epitaxy, were nitrided in a NH<sub>3</sub>/H<sub>2</sub> gas mixture. After different nitriding treatments the specimens were prepared and analyzed by focused ion beam microscopy and X-ray diffraction. It was found that formation of  $\epsilon$ -Fe<sub>2</sub>N<sub>1-x</sub> occurs upon nitriding of specimens exhibiting a small crystallite size at values of the thermodynamic nitriding parameters for which pure  $\gamma'$ -Fe<sub>4</sub>N<sub>1-x</sub> is predicted to form according to bulk thermodynamics. This unexpected phenomenon is explained as a consequence of the nanocrystalline nature on the thermodynamics of the binary system iron - nitrogen.

## 2.1. Introduction

Iron nitrides have attracted great interest in the past decades due to their interesting magnetic properties [1] as well as their distinct resistance to corrosion and wear [2]. Iron-nitride thin films have been produced by a number of techniques including molecular beam epitaxy, laser nitriding and reactive sputtering [3-6]. This work introduces a technique, where gas through-nitriding of iron thin films is employed to obtain iron-nitride thin films on an inert substrate. The paper focuses on the preparation of iron-nitride thin films by gas nitriding of  $\alpha$ -Fe thin films in dependence on the  $\alpha$ -Fe grain size.

## 2.2. Experimental

The deposition of  $\alpha$ -Fe thin films on  $\langle 001 \rangle$  oriented  $\alpha$ -Al<sub>2</sub>O<sub>3</sub> single crystalline wafers (thickness 350  $\mu$ m) was performed by molecular beam epitaxy in an ultra-high vacuum chamber. The film thickness was about 200 nm. Two different iron films were produced: One film showing an average lateral crystallite size of 80 nm and one film exhibiting an average lateral crystallite size of 400 nm. The larger lateral crystallite size was achieved by a two-step annealing process at a temperature of 700 °C during and after the deposition [7]. After deposition the wafers were cut into pieces (area about 15 mm  $\times$  25 mm) by a diamond cutter. Gas nitriding of the  $\alpha$ -Fe thin films was performed in a furnace with a continuous flow of a mixture of NH<sub>3</sub> and H<sub>2</sub> at various temperatures, times and nitriding potentials. The nitriding potential,  $r_N$ , is directly proportional to the nitrogen activity in the nitriding reaction and it is defined by the partial pressures  $p_j$  of the gas components  $j$  involved in the nitriding reaction (cf. chapter 1.1.2.3 and see, for example, Ref. [8]):

$$r_N = p_{\text{NH}_3} / p_{\text{H}_2}^{3/2} \quad (2.1)$$

In order to adjust a certain nitriding potential a constant flow of a NH<sub>3</sub>/H<sub>2</sub> gas mixture has been employed by means of commercially available flow controllers. The total flow rate has been set to 500 ml/min which corresponds to a linear flow rate of 13.5 mm/s at room temperature. The nitriding temperature as well as the nitriding potential was thoroughly calibrated prior to the nitriding experiments. The applied nitriding parameters and the thus produced specimens have been listed in Table 2.1.

**Table 2.1.** Overview of the produced specimens.

specimen	$T$ [°C]	$t$ [min]	$r_N$ [atm <sup>-1/2</sup> ]	average $\alpha$ -Fe crystallite size	treatment after nitriding
A	550	10	1	80 nm	quenched
B	550	10	0.4	80 nm	quenched
C	450	10	1	80 nm	quenched
D	550	10	0.4	80 nm	cooled in NH <sub>3</sub> /H <sub>2</sub> flow
E	550	10	1	400 nm	cooled in NH <sub>3</sub> /H <sub>2</sub> flow

Qualitative phase analysis was performed employing a Philips (now: PANalytical) X'pert MRD diffractometer equipped with a half-circle Eulerian cradle. Co K $\alpha$  radiation emerging from the point focus of a sealed tube operated at 40 kV and 40 mA was converted into a quasi parallel-beam by an X-ray lens. The beam cross section has been set to 4 mm  $\times$  4 mm by crossed slits. The diffracted beam passed a parallel plate collimator (acceptance angle 0.18°) and a flat graphite monochromator before being detected by a gas proportional counter. A spinner was attached to the sample stage to improve crystallite statistics by rotation of the specimen around the surface normal (about 2 rev./s). For the phase-identification measurements of the thin film specimens an incident beam offset of 0.5° was applied in order to suppress the high-intensity single-crystal diffraction peaks from the substrate.

Cross sections of the iron-nitride thin films were cut and investigated employing a FEI FIB 200 focused ion beam microscope.

### 2.3. Results and discussion

Diffraction patterns collected from the thin film specimens produced under various conditions (cf. Table 2.1) are presented in Figure 2.1.

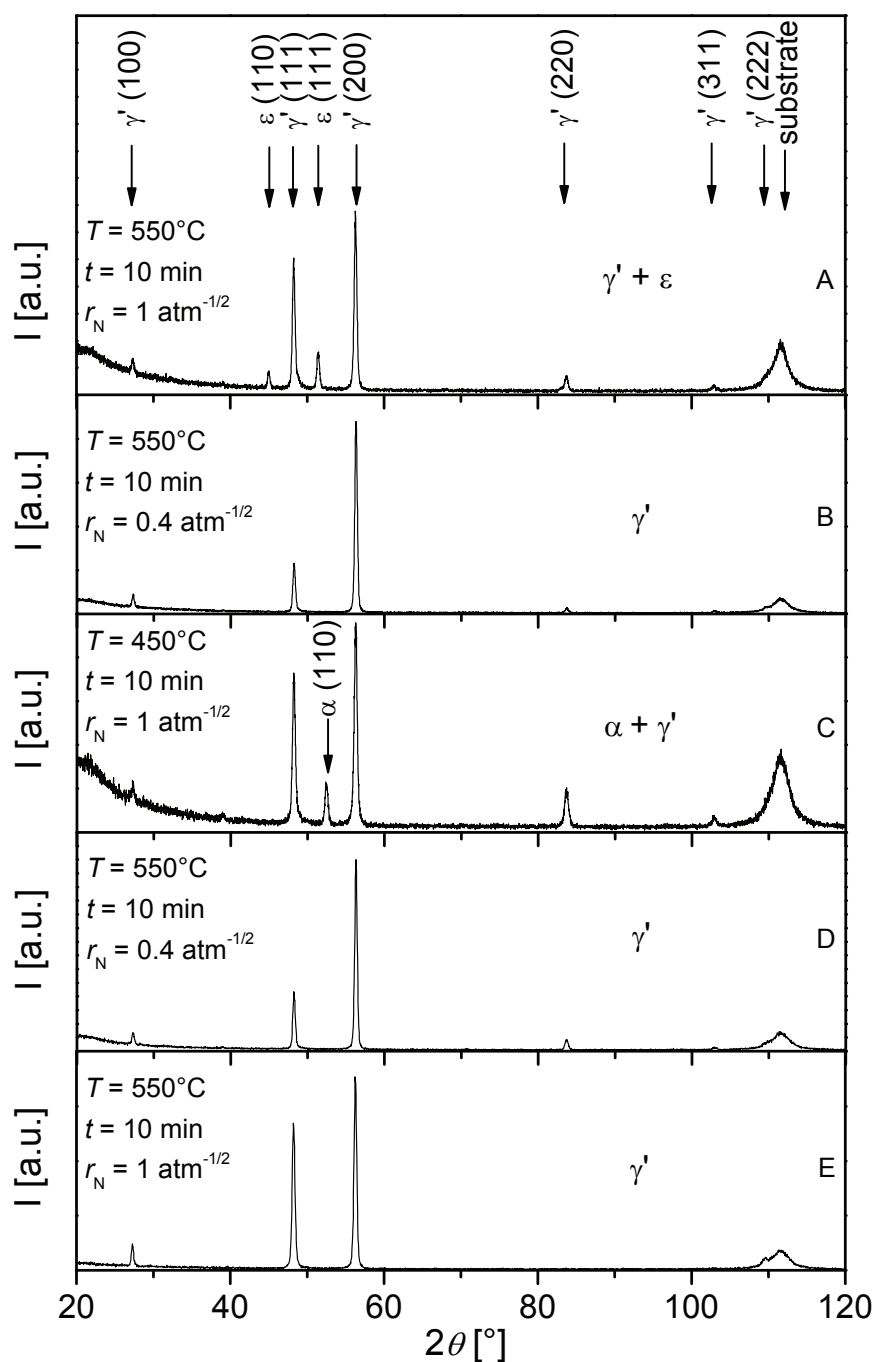


**Figure 2.1.** Diffraction patterns collected from specimen A, B, C, D and E (from top to bottom). The notion “substrate” refers to the  $\alpha$ - $\text{Al}_2\text{O}_3$  (00 12) reflection.

According to the established and generally accepted “Lehrer diagram” [9,10], under the conditions applied only the  $\gamma'$  iron nitride ( $\gamma'$ - $\text{Fe}_4\text{N}_{1-x}$ ; fcc iron lattice with nitrogen in octahedral interstitial sites) could form. Indeed,  $\gamma'$  iron nitride has formed for all specimens. However, strikingly the phase  $\varepsilon$  iron nitride ( $\varepsilon$ - $\text{Fe}_2\text{N}_{1-x}$ ; hcp iron lattice with nitrogen in octahedral interstitial sites) has formed additionally upon

nitriding of specimen A (The reflection, which specimen C shows between the  $\gamma'$  (111) and (200) reflections, does not occur at the position of  $\epsilon$  (111) and can be attributed to the  $\alpha$ -Fe (110) reflection.). This unexpected formation of  $\epsilon$  iron nitride has been confirmed in two additional experiments, where two iron thin film specimens exhibiting the same average crystallite size as specimen A have been nitrided for 30 minutes employing the same temperature and nitriding potential as in the case of specimen A. After nitriding one specimen has been quenched and the other has been slowly cooled. In both cases the formation of  $\epsilon$  iron nitride could be clearly observed.

Micrographs of cross sections of unnitrided and nitrided iron films are shown in Figure 2.2 to Figure 2.6.

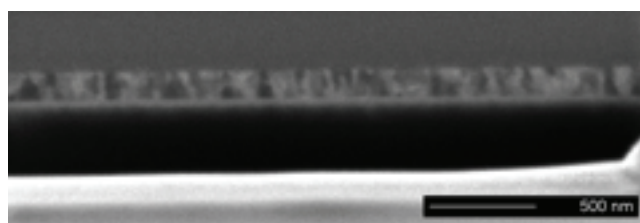


**Figure 2.2.** Focused ion beam micrograph of a cross section of the iron film which has been used for the production of specimens A-D. A tungsten capping layer has been deposited on top of the film.

The as-deposited iron film, as used for specimens A-D (Figure 2.2), has a columnar microstructure with an average lateral grain size of about 80 nm. The surface of the as-deposited layer shows a very low roughness.

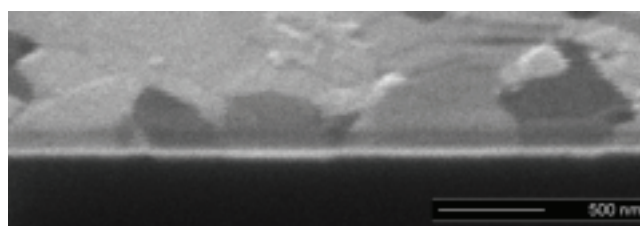


**Figure 2.3.** Focused ion beam micrograph of a cross section of the iron film which has been used for the production of specimen E. No capping layer has been deposited on the film surface.

The as-deposited iron film used for the production of specimen E (Figure 2.3) has a microstructure with a deliberately large (see above) average lateral grain size of

about 400 nm. The surface roughness is comparable with the roughness of the specimen shown in Figure 2.2.

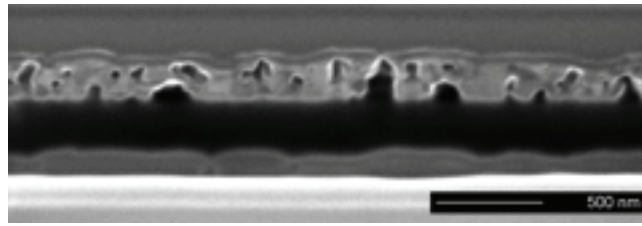


**Figure 2.4.** Focused ion beam micrograph of a cross section of specimen A. A tungsten capping layer has been deposited on top of the film.

The cross section of the nitrated specimen A (Figure 2.4) reveals a considerable porosity within the film. The nitride-grain shape is more globular than columnar. The average lateral nitride-grain size can be estimated as about 140 nm. The pore formation within the film results in an increased surface roughness.

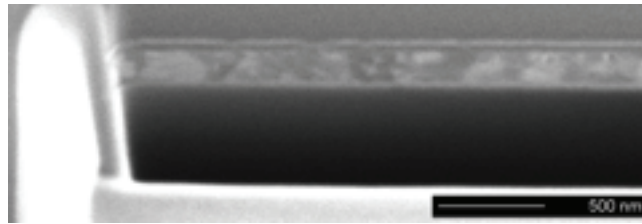


**Figure 2.5.** Focused ion beam micrograph of a cross section of specimen D. A tungsten capping layer has been deposited on top of the film.

The microstructure of specimen D (Figure 2.5) appears to be nearly pore-free making the specimen surface smooth and flat. The crystallites feature a globular morphology and the average lateral nitride-grain size can be estimated as about 80 nm.



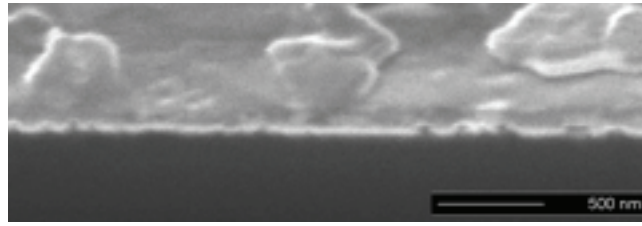


**Figure 2.6.** Focused ion beam micrograph of a cross section of specimen E. No capping layer has been deposited on the film surface.

The cross section of specimen E (Figure 2.6) reveals that during nitriding pore formation has taken place, but to a lower extent than in the case of specimen A. The average lateral nitride-grain size can be estimated as about 160 nm.

Note that specimens A and E have been nitrided under exactly the same conditions. The only difference is the (lateral) grain size of the initial thin iron film. This leads to the supposition that a very tiny grain size (specimen A) may be the origin of the unexpected occurrence of  $\epsilon$  iron nitride (the specimen cooling procedure after nitriding cannot be responsible for the unexpected formation of the  $\epsilon$  phase as both quenching and cooling in nitriding gas flow could only lead to the re-formation of  $\alpha$ -Fe according to the iron-nitrogen phase diagram [9]). Indeed, a polycrystalline  $\alpha$ -Fe bulk specimen (thickness 1 mm) with an average grain size of about 15  $\mu\text{m}$ , which has been nitrided under the same conditions as specimens A and E, did also exclusively show formation of the  $\gamma'$  phase and no formation of the  $\epsilon$  phase. In this case the thickness of the nitride layer was about 5  $\mu\text{m}$ .

The appearance of the  $\epsilon$  phase under the conditions pertaining to specimen A is incompatible with the thermodynamics of the Fe-N system [9]. It should however be realized that the available thermodynamic data on Fe-N pertain to (relatively) coarse-grained specimens. In order to provide a thermodynamical explanation for the observed differences in nitriding behaviour of  $\alpha$ -Fe specimens with different grain sizes the Gibbs energy,  $G$ , of  $\alpha$ ,  $\epsilon$  and  $\gamma'$  has been calculated for a temperature of 550  $^{\circ}\text{C}$  and a pressure of 1 atm as a function of the atom fraction nitrogen,  $x_{\text{N}}$ , using thermodynamical data provided by Refs. [11-13] (see Figure 2.7). For the calculation of the chemical potential of nitrogen in the gas phase at  $r_{\text{N}} = 1 \text{ atm}^{-1/2}$  the reader is referred to Ref. [14].

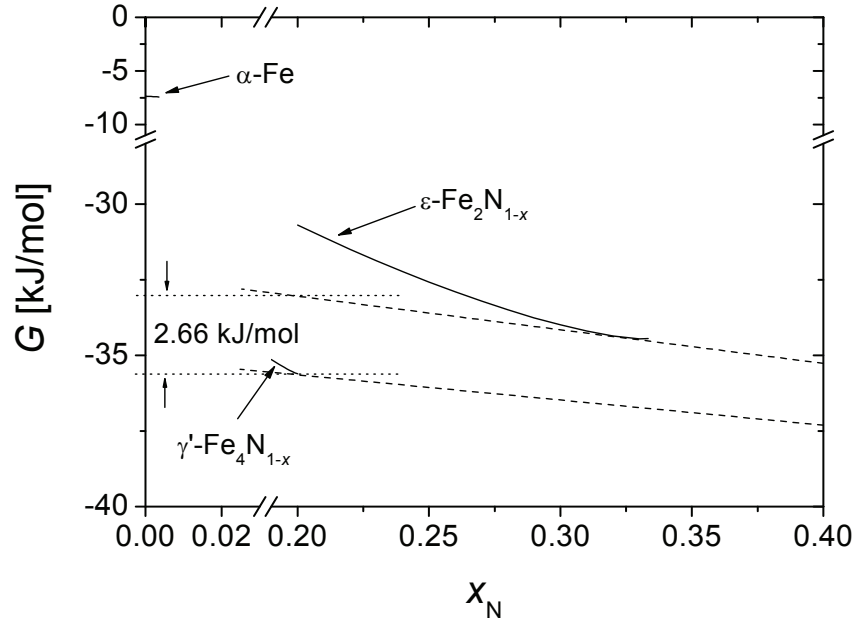


**Figure 2.7.** Gibbs energy,  $G$ , as function of the atom fraction nitrogen,  $x_N$ , for  $\alpha$ -Fe,  $\gamma'$  and  $\epsilon$  at  $T = 550$  °C,  $p = 1$  atm and  $r_N = 1$  atm<sup>-1/2</sup>. The double tangents (dashed) to the  $G(x_N)$  curves of  $\gamma'$  and  $\epsilon$  pass through  $x_N = 1$  corresponding to the chemical potential of nitrogen in the gas phase,  $\mu_{N,g}$ , which has been calculated as  $-42.19$  kJ/mol for the parameters  $T$ ,  $p$  and  $r_N$  stated above. The  $x_N$ -axis range has been restricted for the sake of clarity.

The double tangent constructions applied to the ( $\alpha$ /gas,)  $\gamma'$ /gas and  $\epsilon$ /gas equilibria make clear that, for the Fe-N system at a temperature of 550 °C and a nitriding potential of 1 atm<sup>-1/2</sup> (corresponding to specimens A and E), as solid phase only  $\gamma'$  iron nitride is thermodynamically stable.

The above thermodynamics ignores the effect of grain size. It is suggested below that the increase of Gibbs energy by the Gibbs-Thomson effect due to the very small grain size of  $\gamma'$  iron nitride (small radius of grain-boundary curvature) can be responsible for the unexpected stability of  $\epsilon$  iron nitride.

Due to the curvature of a (spherical) nanocrystalline particle an extra pressure

$$\Delta p = \frac{2\gamma}{r}, \quad (2.2)$$

with  $\gamma$  as the interfacial energy and  $r$  as the radius of the particle, acts on it giving rise to an increase in Gibbs energy

$$\Delta G = \frac{2\gamma V_m}{r}, \quad (2.3)$$

where  $V_m$  is the molar volume [15].

In order to raise the  $G(x_N)$  curve of  $\gamma'$  such that the slope of the double tangent for the  $\gamma'$ /gas equilibrium becomes larger than the slope of the  $\epsilon$ /gas equilibrium, it follows (see Figure 2.7) that a Gibbs energy increase of  $\Delta G = 2.66$  kJ/mol is necessary. An estimate for the radius of the  $\gamma'$  crystallites developing upon nitriding of a nanocrystalline  $\alpha$ -Fe thin film is about 40 nm (see Figure 2.5). It then follows that the interfacial energy of the  $\gamma'$  phase equals about  $1.6$  J/m<sup>2</sup>, which is a realistic value [15]. In the above it has been assumed that the  $\epsilon$  grain size is significantly larger than the  $\gamma'$  grain size, which is supported by the difference in grain size between specimens A ( $\gamma' + \epsilon$ ) and D ( $\gamma'$ ). Additionally it is remarked that the great difference in homogeneity range for  $\epsilon$  and  $\gamma'$  will make the effect of a decrease of grain size on the stability of the nitride/gas equilibrium less pronounced for  $\epsilon$ , as the composition of  $\epsilon$  in equilibrium with gas is variable over a large range, which is not at all the case for  $\gamma'$ .

It has been proposed in Ref. [16] that an increased Gibbs energy of nanocrystalline  $\alpha$ -Fe promotes the formation of  $\epsilon$  iron nitride where  $\gamma'$  iron nitride should form instead according to bulk thermodynamics. However, the thermodynamic analysis given above invalidates such a statement, as upon an increase of the Gibbs energy of  $\alpha$ -Fe still the  $\alpha/\gamma'$  equilibrium should occur; an equilibrium of  $\alpha$  and  $\epsilon$  is impossible (see Figure 2.7).

## 2.4. Conclusions

It has been shown that the thermodynamics of the binary system iron – nitrogen can be influenced significantly by effects resulting from small grain size, such that the formation of  $\epsilon$  iron nitride occurs at thermodynamic parameters where the formation of  $\gamma'$  iron nitride is expected according to bulk thermodynamics.

## Acknowledgements

The authors gratefully acknowledge Dr G. Richter and Mr A.S. Schneider for preparing the iron thin films, Mrs B. Heiland for help with the focused ion beam microscopy. In particular we are indebted to Dr A. Leineweber for helpful discussion.

## References

- [1] Coey, J.M.D. & Smith, P.A.I. (1999). *J. Magn. Magn. Mater.* **200**, 405.
- [2] Knerr, C.H., Rose, T.C. & Filkowski, J.H. (1991). *Gas Nitriding*, in: *ASM Handbook*, edited by S. R. Lampman & T. B. Zorc, Vol. 4, pp. 387. ASM.
- [3] Borsa, D.M., Grachev, S., Boerma, D.O. & Kerssemakers, W.J. (2001). *Appl. Phys. Lett.* **79**, 994.
- [4] Schaaf, P., Lieb, K.P., Carpena, E., Han, M. & Landry, F. (2001). *Czech J. Phys.* **51**, 625.
- [5] Rissanen, L., Neubauer, M., Lieb, K.P. & Schaaf, P. (1998). *J. Alloys Compd.* **274**, 74.
- [6] Schaaf, P. (2002). *Prog. Mater. Sci.* **47**, 1.
- [7] Schneider, A.S., Richter, G. & Arzt, E. *unpublished*.
- [8] Mittemeijer, E.J. & Slycke, J.T. (1996). *Heat Treat. Met.* **23**, 67.
- [9] Mittemeijer, E.J. & Somers, M.A.J. (1997). *Surf. Eng.* **13**, 483.
- [10] Lehrer, E. (1930). *Z. Elektrochem.* **36**, 383.
- [11] Fernández Guillermet, A. & Du, H. (1994). *Z. Metallkd.* **85**, 154.
- [12] Lehrstuhl für Theoretische Hüttenkunde RWTH Aachen (1999). Editors. *Thermodynamic Properties of Inorganic Materials compiled by SGTE*, Berlin: Springer.
- [13] Lehrstuhl für Theoretische Hüttenkunde RWTH Aachen (1999). Editors. *Thermodynamic Properties of Inorganic Materials compiled by SGTE*, Berlin: Springer.
- [14] Kooi, B.J., Somers, M.A.J. & Mittemeijer, E.J. (1996). *Metall. Mater. Trans. A* **27A**, 1063.
- [15] Porter, D.A. & Easterling, K.E. (2001). *Phase Transformations in Metals and Alloys*. Cheltenham, UK: Nelson Thornes.
- [16] Tong, W.P., Tao, N.R., Wang, Z.B., Zhang, H.W., Lu, J. & Lu, K. (2004). *Scripta Mater.* **50**, 647.

### **3. Crystallite-size dependence of the coefficient of thermal expansion of metals**

*Y. Kuru, M. Wohlschlägel, U. Welzel and E.J. Mittemeijer*

#### **Abstract**

The coefficients of thermal expansion (CTEs) of polycrystalline Ni and Cu thin films have been investigated employing temperature-dependent X-ray diffraction measurements of lattice parameters. Great care has been taken to exclude effects of in particular microstructural relaxation and mechanical stresses on the dependences of the lattice parameters on temperature. The CTEs determined in the as-deposited condition, characterised by grain sizes in the range of 25-35 nm, are considerably (about 10 %) larger than the corresponding literature values of bulk materials. Heat treating the specimens at moderate temperatures induced grain growth and a decrease of the crystalline imperfection. After the heat treatment, the CTEs determined for the thin films had reduced considerably and had become equal to (Ni) or approached (Cu) the corresponding literature data for bulk materials.

### 3.1. Introduction

Nanocrystalline materials are of fundamental scientific interest as their physical properties can differ considerably from those of corresponding bulk materials [1-7]. The coefficient of thermal expansion (CTE) of nanocrystalline materials has been investigated both theoretically and experimentally in a number of studies. The findings can be reviewed as follows: Whereas theoretical studies generally conclude that the CTE should increase, from the value for coarse-grained materials, with decreasing crystallite size [8,9], inconsistent experimental results have been obtained: (i) the CTE would be independent of the crystallite size [10-14]; (ii) the CTE would increase with decreasing crystallite size [15-17]; (iii) the CTE would depend on the crystallite size (and, possibly, additional microstructural parameters) and could be both smaller and larger than the CTE of coarse-grained materials [18].

This inconclusive nature of the previous results about the crystallite-size dependence of the CTE may be related to the following experimental, not always recognized, pitfalls: (i) The presence of residual stresses and their variation with temperature in a thin film specimen or in a specimen prepared by techniques like severe plastic deformation and consolidation under an ultrahigh pressure, can affect significantly the lattice parameter as measured in (X-ray) diffraction investigations (e.g. in Refs. [19] and [20]). (ii) For (non-cubic) materials with anisotropic CTEs the occurrence of crystallographic texture affects the macroscopic, mechanical CTE as measured by a technique as dilatometry (e.g. in the case of Se) [21]. (iii) Compositional changes (e.g. in multi-phase systems) and microstructural changes (as grain growth) can occur for a specimen investigated at elevated temperatures (e.g. in Ref. [16]). (iv) (Change of) porosity can be a source of error for CTE values measured by techniques involving the detection of macroscopic, mechanical length changes as dilatometry.

In this work, the following strategy has been adopted to avoid the above mentioned sources of error: X-ray diffraction measurements, insensitive to porosity, have been employed for measuring CTEs. Residual stresses have been considered and their effect on the measured diffraction line position has been separated from the effect of the thermal lattice expansion. High purity specimens consisting of cubic materials (for which the CTE is isotropic) have been used in order to avoid composition changes and complications arising from the presence of crystallographic

texture. The measurements have been carried out below room temperature, to exclude the occurrence of thermally activated processes as grain growth, which has been shown here to be of cardinal importance.

### 3.2. Experimental

Ni and Cu thin films were deposited at room temperature on Si(100) wafers covered with thin amorphous SiO<sub>2</sub> and Si<sub>3</sub>N<sub>4</sub> barrier layers (each 50 nm thick) by DC magnetron sputtering (base pressure about  $1 \times 10^{-10}$  mbar) employing Ar (at  $2 \times 10^{-4}$  mbar) as a sputter gas. Each of the thin films had a thickness of 50 nm.

The as-deposited layers were mounted on a heating/cooling chamber for X-ray diffraction investigations (Anton Paar DCS350; for temperature calibration and further details, see Ref. [22]) attached to the Eulerian cradle of a Bruker D8 Discover parallel-beam diffractometer equipped with a rotating-anode Cu K $\alpha$  X-ray source (Bruker TXS), a collimating X-ray mirror (Xenocs) and a scintillation counter (see Ref. [23] and chapter 6). The specimens were cooled from room temperature (25 °C) to -100 °C with temperature steps of 25 °C. Residual stresses (i.e. the stress, planar and rotationally symmetric, parallel to the specimen surface  $\sigma$ ) were measured at every temperature step employing the crystallite group method (CGM) making use of the {111} reflection. The CGM, allowing direct use of the intrinsic single crystal elastic constants (SEC), was preferred over the traditional  $\sin^2\psi$ -analysis ( $\psi$  is the angle between the diffraction vector and the specimen surface normal) involving X-ray elastic constants, as both layers had strong and sharp {111} fibre textures [24]. The strain free lattice parameter ( $a_0$ ) at a given temperature was calculated from the interplanar spacing of the {111} lattice planes by interpolating at the strain-free direction  $\sin^2\psi_0$  calculated from the SEC [24]. This approach presupposes that the value of  $\sin^2\psi_0$  is neither affected by the temperature-dependence nor by a possibly occurring grain-size dependence of the SEC. This can be made likely considering that: (i)  $\sin^2\psi_0$  depends upon the ratio of sums and differences of the individual SEC (temperature/size-dependent changes then cancel at least partially); (ii) no significant grain-size dependence of the SEC is expected for grain sizes exceeding 20 nm [25,26].

For every temperature step, the {111} reflections were recorded at two tilt angles,  $\psi = 0^\circ$  and  $\psi = 70.54^\circ$ . The time required for one stress measurement was 22 minutes. A waiting time of 5 minutes was adopted upon arriving at the temperature of each temperature step in order to guarantee temperature homogenization.

### 3.3. Results and discussion

The average CTE values of the layers for the temperature range between 25 °C and -100 °C were obtained from the slope of plots of the (thermal) lattice strain ( $\varepsilon_{\text{th}} = \Delta a_0 / a_0^{25^\circ\text{C}}$ ) versus temperature. The results obtained in the as-deposited conditions have been gathered in Figure 3.1. For the strain calculation, the strain at ambient temperature (25 °C) was taken as zero. It follows that the CTEs for the Ni and Cu layers in as-deposited condition are considerably larger than the CTE value according to the literature for the same temperature range (cf. Table 3.1).

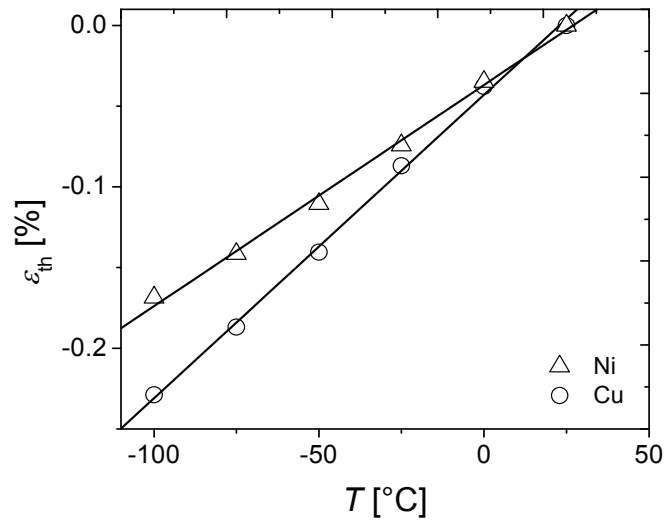


**Figure 3.1.** The thermal strain,  $\varepsilon_{\text{th}}$  ( $=\Delta d/d_0$ , where  $d_0$  is the spacing of certain lattice planes at room temperature and  $\Delta d$  is the change in lattice-plane spacing when the temperature is changed by  $\Delta T$ ) for nickel (Ni) and copper (Cu) layers in the as-deposited nanocrystalline state as a function of temperature,  $T$ . The CTEs are the slopes of the fitted straight lines.



**Table 3.1.** The measured CTE values of the Ni and Cu thin films and the corresponding literature values [27,28]. TF: Thin film specimen, CG: Coarse-grained specimen.

	CTE of Ni [ $10^{-6}/^{\circ}\text{C}$ ]	CTE of Cu [ $10^{-6}/^{\circ}\text{C}$ ]
As-deposited (TF)	$13.7 \pm 0.4$	$18.8 \pm 0.4$
After heat treatment (TF)	$12.6 \pm 0.2$	$17.4 \pm 0.4$
Literature value (CG)	12.4	15.7
	$D$ of Ni [nm]	$D$ of Cu [nm]
As-deposited (TF)	37	26
After heat treatment (TF)	59	41

After the cooling cycles, the layers were heat treated according to a temperature cycle between room temperature and 250 °C (heating and cooling with temperature steps of 25 °C). This temperature cycle was repeated four times for both layers to establish a stabilized microstructure (as evidenced by achieved constancy of diffraction-line position and shape). It was verified that the heating cycles did not lead to a significant change of the strain-free lattice constant at room temperature. The evolution of the stress state during the thermal cycles was measured employing the CGM (for details see above; results not shown). Annealing the specimens at elevated temperatures during the heating cycles resulted even in a slight increase of the texture strength. Changes of crystallite size and microstrain during the thermal cycles were monitored by single line broadening analysis with the diffraction vector oriented perpendicular to the specimen surface (i.e.  $\psi = 0^{\circ}$ ) [29-31]. Results are shown in Figure 3.2. Whereas an increase of the crystallite size and a decrease of the microstrain were detected during the first temperature cycle, the crystallite size and microstrain did not show any further changes in the subsequent cycles. The increase of the crystallite size during the first heating cycle was paralleled by the emergence of a considerable tensile stress contribution in both layers superimposed upon the stress evolution resulting from the mismatch of the coefficients of thermal expansion of substrate and layer. Adopting a simple treatment proposed by Doerner and Nix [32] (extending the treatment by Chaudhari [33]), that ascribes the generation of tensile stress to the elimination of excess volume in the grain boundaries during grain growth, it was shown here that the amounts of tensile stress arising during the first heating cycle in both layers (700 MPa and 300 MPa for Ni and Cu layers,

respectively) are well compatible with the increases of grain size as determined from the diffraction-line broadening analyses, if the excess volume per unit area of the grain boundary is taken about half of an atomic diameter.

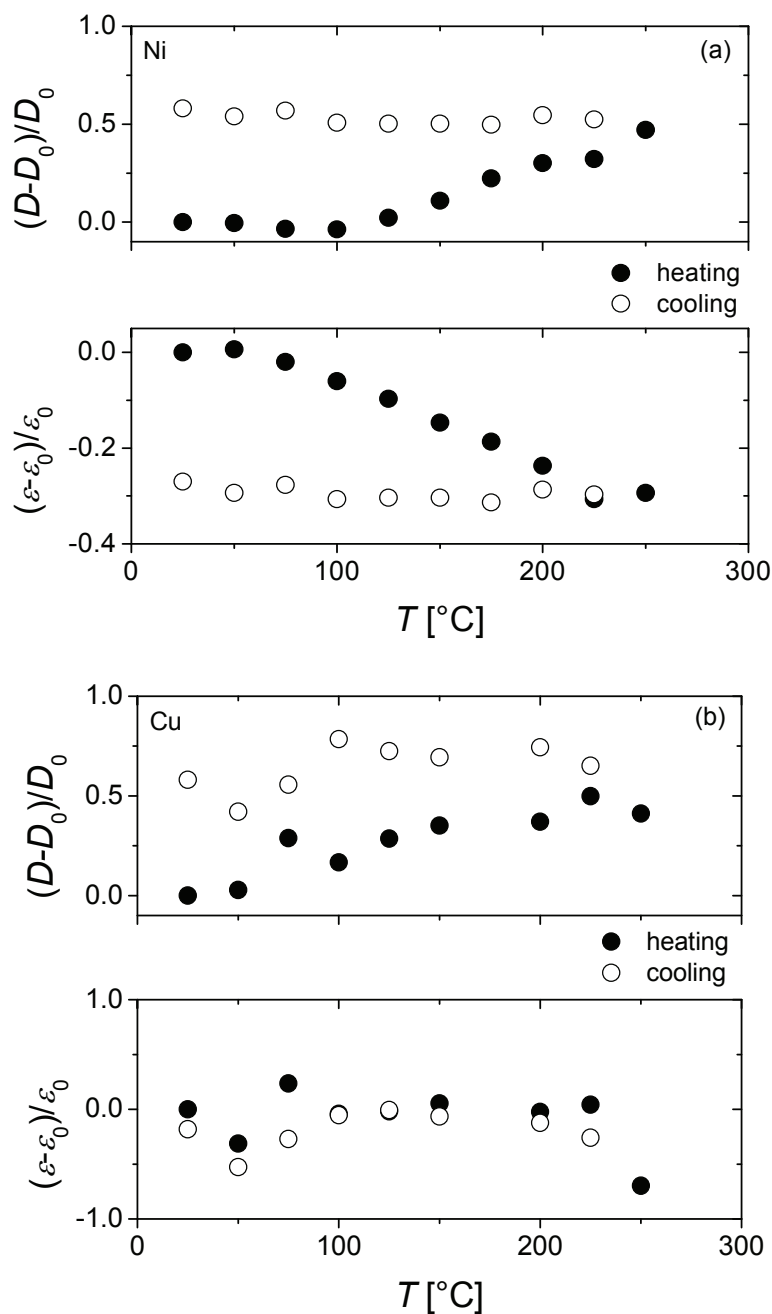


**Figure 3.2.** Variation in crystallite size,  $(D-D_0)/D_0$ , and variation in microstrain,  $(\varepsilon-\varepsilon_0)/\varepsilon_0$ , versus temperature,  $T$ , for (a) Ni ( $D_0 = 37$  nm,  $\varepsilon_0 = 0.3$  %) and (b) Cu ( $D_0 = 26$  nm,  $\varepsilon_0 = 0.17$  %) layers during the first heating cycle between 25 °C and 250 °C.

After completing the heating cycles, the CTE values of the layers were again obtained for the temperature range between 25 °C and -100 °C from the slope of plots of the strain  $\varepsilon_{th}$  versus temperature. The results are shown in Figure 3.3 (see also Table 3.1). It follows that upon heat treatment the CTEs for the Ni and Cu layers had reduced significantly: In accordance with an increase of the crystallite size of the Ni layer from about 35 nm to about 50 nm, a decrease of the CTE occurred from  $13.7 \times 10^{-6} \text{ 1/}^\circ\text{C}$  to  $12.6 \times 10^{-6} \text{ 1/}^\circ\text{C}$ . This last value is equal to the corresponding literature value within experimental accuracy (see Table 3.1) for the temperature range considered. In accordance with an increase of the crystallite size of the Cu layer from 25 nm to about 40 nm, a decrease of the CTE occurred from  $18.8 \times 10^{-6} \text{ 1/}^\circ\text{C}$  to  $17.4 \times 10^{-6} \text{ 1/}^\circ\text{C}$ . This last value is closer to but still larger than the corresponding literature value. Evidently, the crystallite size of the Cu layer at the end of the heat treatment is smaller than that of the Ni layer, which may explain that the CTE of the Cu film after the heat treatment is still larger than the literature value.

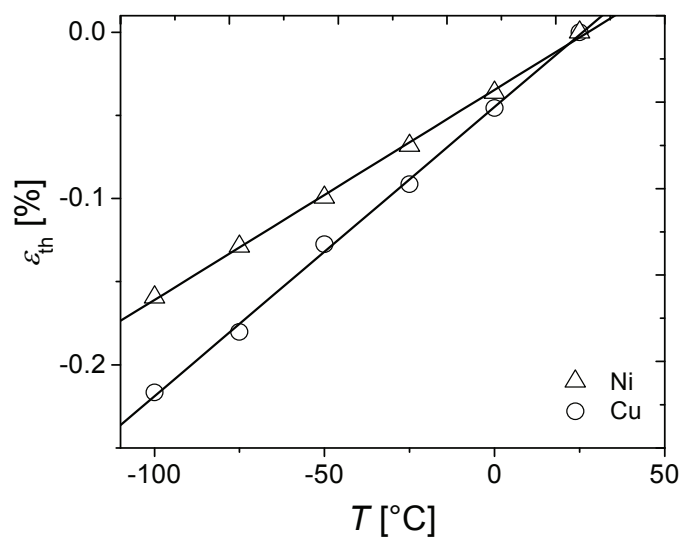


**Figure 3.3.** The thermal strain,  $\varepsilon_{th}$ , for nickel (Ni) and copper (Cu) layers as a function of temperature,  $T$ , after four heating cycles between 25 °C and 250 °C. The CTEs are the slopes of the fitted straight lines.

The findings obtained for the CTEs can be understood as follows: Atoms at the surface of a crystal or at an (incoherent) interface (grain boundary) are not saturated with respect to their state of bonding: their coordination number (i.e. the number of nearest neighbours) is less than for bulk atoms. As a consequence the curve of potential energy per atom versus interatomic distance for a surface/interface atom

shows a less deep potential energy minimum well than for a bulk atom (cf. Figure 3.4). The effect of a similar vibrational kinetic energy for surface/interface and bulk atoms now has consequences of different extent. Evidently, the less deep potential energy minimum for the surface/interface atom, as compared to the bulk atom, leads to a larger atomic position variation due to thermal vibration for the surface/interface atom than for the bulk atom. Consequently, in view of the asymmetry of the potential energy minimum wells, the thermal expansion for the surface/interface atoms of the crystal is larger than for the bulk atoms (Experimental proof, that the above discussed potential energy well is less deep and moreover more asymmetric for surface atoms than for bulk atoms, has been provided in Ref. [34].). The smaller a crystal, the larger the ratio of the number of surface/interface atoms and the number of bulk atoms. Hence, the smaller a crystal, the larger its *average* CTE.

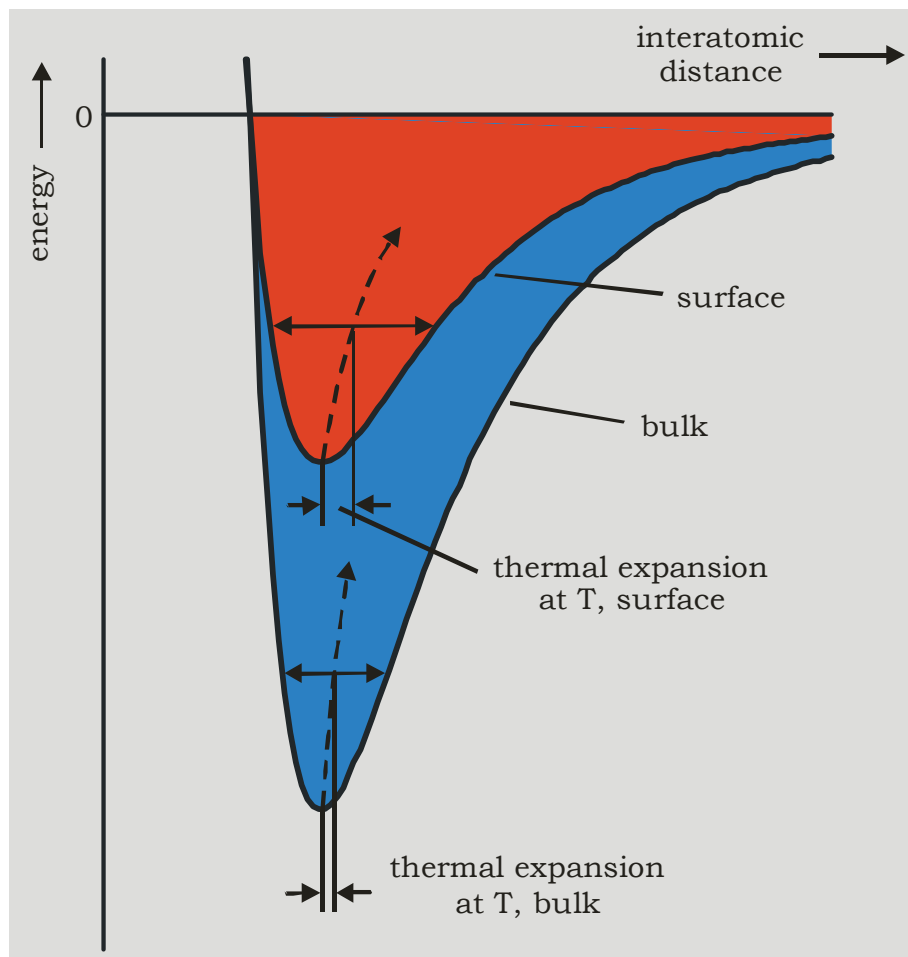


**Figure 3.4:** Potential energy as a function of interatomic distance for bulk and surface atoms.

Thus, the dependence of the CTE on crystallite size has been proven finally, by avoiding interference of effects of porosity, preferred orientation and, in particular, residual stress and microstructural changes (occurring at and above room temperature in nanocrystalline thin films of metals). By an increase of crystallite size from 35 nm to 50 nm in a Ni thin film the CTE decreased by 8.0 %, thereby attaining its value for coarse-grained bulk material. For a Cu thin film, an increase of crystallite size from 25 nm to 40 nm led to a 7.4 % reduction in its CTE which then is closer to but still larger than the value for coarse-grained material. The initially larger difference with the CTE for coarse-grained, bulk material for the Cu layer, as compared with the Ni layer, and, after heat treatment, the remaining, although pronouncedly reduced, difference with the CTE for coarse-grained bulk material in case of only the Cu layer, may be related to smaller initial and final crystallite sizes for the Cu layer.

### **3.4. Conclusions**

It is concluded that the CTE of a material with a grain size in the nanometre range will generally be distinctly larger than the CTE of its conventional coarse-grained counterpart. This can have grave consequences for the interpretation of thermoelastic properties (e.g. biaxial modulus) of thin films; at the same time the possibility is now given to tune the CTE of a thin film by modifying its microstructure.

### **Acknowledgements**

We thank Mr F. Thiele and Dr G. Richter (Max Planck Institute for Metals Research, Stuttgart, Germany) for the specimen production.

## References

- [1] Birringer, R. & Gleiter, H. (1988). *Nanocrystalline Materials*, in: *Encyclopedia of Materials Science and Engineering*, edited by R. W. Cahn, Vol. 1 (Suppl.), Oxford: Pergamon Press.
- [2] Budrovic, Z., van Swygenhoven, H., Derlet, P.M., van Petegem, S. & Schmitt, B. (2004). *Science* **304**, 273.
- [3] Gleiter, H. (1990). *Phase Transit.* **24-26**, 15.
- [4] Nix, W. D. (1989). *Metall. Trans. A* **20A**, 2217.
- [5] Shan, Z., Stach, E.A., Wiezorek, J.M.K., Knapp, J.A., Follstaedt, D.M. & Mao, S.X. (2004). *Science* **305**, 654.
- [6] van Swygenhoven, H., Derlet, P.M. & Frøseth, A.G. (2004). *Nature Mater.* **3**, 399.
- [7] Yakamov, V., Wolf, D., Phillpot, S.R., Mukherjee, A.K. & Gleiter, H. (2002). *Nature Mater.* **1**, 45.
- [8] Fecht, H.J. (1990). *Phys. Rev. Lett.* **65**, 610.
- [9] Wagner, M. (1992). *Phys. Rev. B* **45**, 635.
- [10] Eastman, J.A., Fitzsimmons, M.R. & Thompson, L.J. (1992). *Philos. Mag. B* **66**, 667.
- [11] Eastman, J.A., Fitzsimmons, M.R., Thompson, L.J., Lawson, A.C. & Robinson, R.A. (1992). *Nanostruct. Mater.* **1**, 465.
- [12] Harada, J. & Oshima, K. (1981). *Surf. Sci.* **106**, 51.
- [13] Panigrahi, B.B., Dabhade, V.V. & Godkhindi, M.M. (2005). *Mater. Lett.* **59**, 2539.
- [14] Turi, T. & Erb, U. (1995). *Mater. Sci. Eng. A* **204**, 34.
- [15] Lee, J.-G. & Mori, H. (2005). *Eur. Phys. J. D* **34**, 227.
- [16] Lu, K. & Sui, M.L. (1995). *Acta Metall. Mater.* **43**, 3325.
- [17] Zhao, Y.H. & Lu, K. (1997). *Phys. Rev. B* **56**, 14330.
- [18] Fang, W. & Lo, C.-Y. (2000). *Sensor Actuat. A-Phys.* **84**, 310.
- [19] Zhang, K., Alexandrov, I.V., Valiev, R.Z. & Lu, K. (1998). *J. Appl. Phys.* **84**, 1924.
- [20] Zoo, Y., Adams, D., Mayer, J.W. & Alford, T.L. (2006). *Thin Solid Films* **513**, 170.

- [21] Zhang, H. & Mitchell, B.S. (1999). *Mater. Sci. Eng. A* **270**, 237.
- [22] Wohlschlägel, M., Welzel, U., Maier, G. & Mittemeijer, E. J. (2006). *J. Appl. Cryst.* **39**, 194.
- [23] Wohlschlägel, M., Schüllli, T.U., Maier, G., Welzel, U. & Mittemeijer, E.J. (2007). *Z. Kristallogr. Suppl.* **26**, 147.
- [24] Welzel, U., Ligot, J., Lamparter, P., Vermeulen, A.C. & Mittemeijer, E.J. (2005). *J. Appl. Cryst.* **38**, 1.
- [25] Latapie, A. & Farkas, D. (2003). *Scripta Mater.* **48**, 611.
- [26] Shen, T.D., Koch, C.C., Tsui, T.Y. & Pharr, G.M. (1995). *J. Mater. Res.* **10**, 2892.
- [27] Touloukian, Y. S., Kirby, R. K., Taylor, R. E. & Desai, P. D. (1975). *Thermal Expansion, Metallic Elements and Alloys*. New York: IFI/Plenum.
- [28] Altman, H.W., Rubin, T. & Johnston, H.L. (1954). *Cryogenic Laboratory Report OSU-TR-267-27*. Ohio State University. Columbus, OH.
- [29] de Keijser, Th. H., Langford, J.I., Mittemeijer, E.J. & Vogels, A.B.P. (1982). *J. Appl. Cryst.* **15**, 308.
- [30] Delhez, R., de Keijser, Th. H. & Mittemeijer, E. J. (1982). *Fresenius. J. Anal. Chem.* **312**, 1.
- [31] Mittemeijer, E.J. & Scardi, P. (2004). Editors. *Diffraction Analysis of the Microstructure of Materials*, Berlin: Springer.
- [32] Doerner, M. F. & Nix, W. D. (1988). *Crit. Rev. Solid State* **14**, 225.
- [33] Chaudhari, P. (1972). *Vac. Sci. Technol.* **9**, 520.
- [34] Kiguchi, M., Yokoyama, T., Matsumura, D., Kondoh, H., Endo, O. & Ohta, T. (2000). *Phys. Rev. B* **61**, 14020.





## 4. Determination of depth gradients of grain interaction and stress in Cu thin films

*M. Wohlschlägel, W. Baumann, U. Welzel and E.J. Mittemeijer*

### Abstract

Grain-interaction and residual stress depth gradients in a sputter-deposited Cu thin film (thickness 4  $\mu\text{m}$ ) were determined employing X-ray diffraction stress measurements at constant information depths in the range between 200 and about 1500 nm. A novel procedure, which allows the determination of an effective grain-interaction parameter on the basis of the  $f(\psi, hkl)$ -method and the Voigt and Reuss models of elastic grain interaction was employed. The range of accessible penetration depths was maximised by employing different photon energies using a laboratory diffractometer with Cu  $K\alpha$  radiation and a diffractometer at a synchrotron beamline. The variation of grain interaction with depth could be successfully related to the specimen's microstructure. The tensile residual stress in the film parallel to its surface decreases with decreasing depth. By measuring the lattice spacing for several reflections at one penetration depth with two different photon energies (i.e. using small and large incident beam angles) it was found that the surface roughness of the specimen counteracts the effect of beam refraction to some degree. As a consequence, irrelevant of applying or neglecting a refraction correction for the low-incidence angle measurement, erroneous results are obtained for lattice spacings derived from reflections at small incidence angles; reliable grain-interaction and stress analysis requires measurements at high incidence angle.

## 4.1. Introduction

The analysis of depth gradients of grain interaction and stress is highly important for materials frequently used in thin film devices, as copper thin films. Such gradients can develop as a consequence of the production process, for example when deposition parameters are changed during deposition.

(X-ray) Diffraction is frequently employed in the analysis of stress and microstructure of materials [1-3]. For this purpose diffraction lines of one or more  $hkl$  reflections are measured at various tilt angles,  $\psi$ , and, depending on the complexity of the stress state, rotation angles,  $\varphi$ . From the angular positions of the diffraction lines lattice spacings and thus (elastic) lattice strains can be calculated.

In order to calculate mechanical stresses from lattice strains measured employing diffraction methods, the use of a suitable grain-interaction model is of cardinal importance [4]. In the past, a number of grain-interaction models have been developed. Grain-interaction models permit the calculation of (polycrystal) mechanical and X-ray elastic constants (X-ray stress factors for macroscopically elastically anisotropic materials) from single crystal elastic data [5] (see also [3] and references therein). The various existing grain-interaction models differ in the assumptions made concerning the elastic behaviour of the polycrystal in the specimen frame of reference. For example, the Voigt model [6] involves the assumption that all crystallites of the polycrystal exhibit the same state of strain, whereas in the Reuss model [7] it is assumed that all crystallites have the same state of stress. These two models represent mutually extreme cases and both of them are incompatible with the real elastic behaviour of a polycrystal at its grain boundaries. For this reason, so-called effective grain-interaction models have been devised [8-10]. A simple effective grain-interaction model traditionally employed is the Neerfeld-Hill model [11,12]. In this model the arithmetic average of the X-ray elastic constants according to the Voigt and the Reuss models is employed to obtain the (X-ray) elastic constants. It can be proposed to adopt a weighing factor for the Voigt and Reuss models, in a linear combination, to improve the description of the real-elastic behaviour of the polycrystal [3,8,9,13].

In this work, a new procedure, on the basis of the so-called  $f(\psi, hkl)$ -method [3,14,15], has been employed in order to obtain an optimized grain-interaction

parameter, i.e. the weighing factor expressing the relative contributions of the Voigt- and Reuss-type interactions. The data collection has been performed by X-ray diffraction measurements at constant penetration depth, thus allowing depth-resolved analysis of grain interaction and stress. The range of accessible penetration depths has been maximized by applying different photon energies using a laboratory diffractometer with Cu Ka radiation and a diffractometer at a synchrotron beamline. Special attention has been paid to the effects of surface roughness and refraction at low-incidence angle measurements. It has been found for the present specimen that the refraction effect on the diffraction angle is reduced by the surface roughness. Neglecting this effect in the application of a refraction correction (see, for example [16]) can lead to unreliable results for measurements at small incidence angles ( $< 2.5^\circ$ ).

## **4.2. Theoretical background**

### **4.2.1. Diffraction measurements at fixed penetration depth**

The penetration depth  $\tau$  is defined by the centre of gravity of the distribution of measured diffracted intensity versus depth for an infinitely thick, homogeneous specimen (see, for example, [17]). From the total diffracted intensity an amount of about 63% originates from depths confined by  $\tau$  below the specimen surface. In a (X-ray) diffraction measurement the penetration depth is fully determined by the incidence ( $\alpha$ ) and exit ( $\beta$ ) angles of the primary beam and the diffracted beam, respectively, and the linear absorption coefficient  $\mu$  (see, for example, [18] and [19]):

$$\tau = \frac{\sin \alpha \sin \beta}{\mu(\sin \alpha + \sin \beta)}. \quad (4.1)$$

The information depth  $\xi$  is an average depth below the surface of a particular specimen, which is obtained by weighing (the signal originating from) the depth  $z$  with an absorption factor which accounts for the intensity reduction of the incident and diffracted beams due to absorption of (see, for example, [17]). For a specimen with thickness  $t$  it thus follows:

$$\xi(t) = \langle z \rangle = \frac{\int_0^t z \exp(-z/\tau) dz}{\int_0^t \exp(-z/\tau) dz} = \tau - \frac{t \exp(-t/\tau)}{1 - \exp(-t/\tau)}, \quad (4.2)$$

where brackets ' $\langle \rangle$ ' indicate (depth) averaging.

In order to keep the penetration depth constant during a measurement, involving variation of the diffraction angle, the incidence and exit angles have to be selected appropriately by adjusting the instrumental angles of the diffractometer. As a consequence the range of specimen-tilt,  $\psi$ -angles accessible for diffraction from a family of  $hkl$  lattice planes at a certain photon energy and at fixed penetration/information depth is limited. It is advisable to select parallel-beam geometry as experimental setup for diffraction measurements at constant penetration depth, as the low residual divergence of the incident beam allows the adjustment of a well-defined incidence angle. For further details, see Ref. [19].

#### 4.2.2. Refraction and surface-roughness effects

For the investigation of very small penetration depths, small incident beam angles  $\alpha$  (or exit angles  $\beta$ ) have to be chosen for a given absorption coefficient  $\mu$  (cf. equation (4.1)). If the angle  $\alpha$  decreases and approaches the critical angle for total external reflection (some tenths of a degree) equation (4.1) no longer holds:  $\tau$  varies more strongly with  $\alpha$  than indicated by equation (4.1), because refraction of the incident beam significantly influences the penetration depth. Such refraction effects are already considerable for incidence angles smaller than about  $2.5^\circ$  (see, for example Ref. [20] or [21] and, in particular for analysis at constant penetration depth, Ref. [19]). Refraction corrections have been performed in this work for the refraction-induced deviation of the diffraction angle [20]. The refraction-induced deviation of the orientation of the diffraction vector can be neglected [20].

It has to be recognized that the above mentioned correction of the diffraction angle for refraction is only valid for ideally flat specimen surfaces. With increasing surface roughness the refraction effect decreases, as the fraction of actual incidence (and exit) angles much larger than the set (with respect to an ideally flat surface) values increases. This phenomenon has been investigated experimentally in Ref. [21].

Until today, a theoretical implementation of the surface-roughness effect on refraction lacks.

#### 4.2.3. The $f(\psi, hkl)$ -method; determination of effective grain interaction

For the analysis of a rotationally symmetric, biaxial state of stress of cubic materials the traditional  $\sin^2\psi$  method boils down to application of the formula (see, for example, [2,3,15]):

$$\varepsilon_{\psi}^{hkl} = \frac{d_{\psi}^{hkl} (h^2 + k^2 + l^2)^{1/2} - a_0}{a_{\text{ref}}} = \left( 2S_1^{hkl} + \frac{1}{2}S_2^{hkl} \sin^2 \psi \right) \langle \sigma_{\parallel}^S \rangle, \quad (4.3)$$

where  $\varepsilon_{\psi}^{hkl}$  is the lattice strain and  $d_{\psi}^{hkl}$  is the spacing of a set of lattice planes  $hkl$  ( $hkl$  are the Miller indices) at the angle  $\psi$ ,  $a_0$  and  $a_{\text{ref}}$  are the strain-free and reference lattice parameter, respectively. The value for  $a_{\text{ref}}$  can be any value close to  $a_0$ , as a slight difference between these two values is of minor importance (see [15]).  $S_1^{hkl}$  and  $1/2 S_2^{hkl}$  are the X-ray elastic constants which can be calculated from single-crystal elastic constants applying a suitable grain-interaction model (see, for example [3]). To this end the Voigt [6] and Reuss [7] models yield two extreme cases of grain interaction. The mechanical in-plane residual stress is denoted by  $\langle \sigma_{\parallel}^S \rangle$ . Measuring the lattice spacing of several crystallographic lattice planes of a cubic material at various angles  $\psi$  one can plot  $d_{\psi}^{hkl} (h^2 + k^2 + l^2)^{1/2}$  versus  $f(\psi, hkl)$  (referred to as  $f(\psi)$ -plot, hereafter), where

$$f(\psi, hkl) = a_{\text{ref}} \left( 2S_1^{hkl} + \frac{1}{2}S_2^{hkl} \sin^2 \psi \right), \quad (4.4)$$

which according to equation (4.3) yields a straight line with the stress as slope [3,14,15]. Using this approach it is possible to determine an effective grain-interaction parameter  $w$  by substitution of  $S_1^{hkl}$  and  $1/2 S_2^{hkl}$  in equations (4.3) and (4.4) according to

$$S_{1,2}^{hkl} = wS_{1,2}^{hkl,V} + (1-w)S_{1,2}^{hkl,R}, \quad (4.5)$$

where the superscripts ‘V’ and ‘R’ indicate the Voigt and Reuss models, respectively. A least-squares fit to the data in the  $f(\psi)$ -plot yields values for the stress  $\langle \sigma_{\parallel}^S \rangle$  and the grain-interaction parameter  $w$ .

It has to be noted that, whereas in the traditional  $\sin^2\psi$  analysis *relative* values for the lattice parameter (i.e. lattice strains) are used, in the  $f(\psi, hkl)$ -method *absolute* values for the lattice parameter are employed to evaluate stress and grain interaction. As a consequence, the  $f(\psi, hkl)$ -method is more prone to errors associated with instrumental aberrations. Thus, for the X-ray diffraction experiments in this kind of analysis it is beneficial to employ parallel-beam geometry as, besides the offset in diffraction angle, it is insensitive to other instrumental aberrations [10,22,23] (see also chapter 6). The instrumental offset in the diffraction angle is included as an additional fit parameter in the evaluation of the  $f(\psi)$ -plot.

### 4.3. Experimental

#### 4.3.1. Specimen preparation

A Cu thin film with a thickness of about 4  $\mu\text{m}$  was sputter-deposited onto a thermally oxidized Si <100> wafer (thickness 500  $\mu\text{m}$ ) by a planar direct-current magnetron equipped with a copper target in an ultra high vacuum (UHV) chamber. The base pressure in the ultra high vacuum chamber was of the order of  $10^{-8}$  mbar. Before the deposition the substrate was cleaned by Ar ion bombardment with an ion gun. The magnetron was operated at 100 W using precleaned Ar 6.0 with a pressure of approximately  $3 \times 10^{-3}$  mbar as a sputter gas. About half of the film thickness was deposited at a substrate temperature of 400 °C. After that the specimen was cooled in UHV to room temperature and the second half of the film thickness was deposited at room temperature. From the Cu coated wafer pieces with a size of 14 mm  $\times$  14 mm were cut by a diamond cutter.

#### 4.3.2. Focused ion beam microscopy

Microstructural investigations were carried out employing a FEI Nova 600 Nanolab DualBeam-workstation. Before cross sections were cut and visualized with a focused Ga-ion beam a thin platinum layer was deposited onto the specimen in order to protect its surface during cutting. The beam-current during imaging was 10 pA.

### 4.3.3. Surface topography

The surface topography of the specimens was visualized employing a Topometrix Explorer atomic force microscope (AFM) in contact mode. As a result of the AFM investigation two roughness values were determined:

$$\text{average roughness: } R_a = \frac{1}{n} \sum_{i=1}^n |z_i - \bar{z}|, \quad (4.6)$$

$$\text{root-mean-square roughness: } R_{\text{ms}} = \sqrt{\frac{1}{n} \sum_{i=1}^n (z_i - \bar{z})^2}, \quad (4.7)$$

where  $n$  is the number of measured data points,  $\bar{z}$  is the arithmetic mean of the measured heights and  $z_i$  are the absolute values of the measured heights.

Three measurements were performed, scanning an area of  $20 \mu\text{m} \times 20 \mu\text{m}$  at three different locations on the surface. The arithmetic means of these three measurements of the above defined roughness values were determined.

### 4.3.4. X-ray diffraction measurements

Laboratory X-ray diffraction measurements were carried out at a Philips X'Pert MRD Pro diffractometer for pole-figure measurements and at a Bruker AXS D8 Discover diffractometer for all other laboratory diffraction experiments, both equipped with an Eulerian cradle.

At the X'Pert MRD Pro diffractometer Cu  $K\alpha$  radiation emerging from the point focus of sealed tube operated at 40 kV and 45 mA was converted to a quasi-parallel beam (divergence  $0.3^\circ$ ) by an X-ray lens with an aperture of approximately 7 mm. The size of the beam was set to  $4 \text{ mm} \times 4 \text{ mm}$  with the help of crossed slits. The diffracted beam passed a parallel-plate collimator with an acceptance angle of  $0.27^\circ$  and a flat graphite analyzer before being detected by a gas proportional counter. The integrated intensities of the 111 reflection were collected as function of the angles  $\varphi$  and  $\psi$  in steps of  $2^\circ$  from  $1^\circ$  to  $359^\circ$  and  $0^\circ$  to  $88^\circ$ , respectively. For the generation of the pole figure the software package X'pert Texture 1.0a (Philips Electronics NV, Almelo, The Netherlands) was employed.

At the D8 Discover diffractometer Cu  $K\alpha$  radiation emerging from the point focus with a size of  $0.1 \text{ mm} \times 0.1 \text{ mm}$  of a rotating anode operated at 50 kV and 20 mA was converted to a quasi-parallel beam (divergence  $0.03^\circ$ ) by cross-coupled

Göbel mirrors. The beam size at the mirror exit was approximately  $1 \text{ mm} \times 1 \text{ mm}$ . The diffracted beam passed a parallel-plate collimator with an acceptance angle of  $0.23^\circ$  before being detected by a scintillation counter.

The use of parallel beam geometry at both diffractometers made it possible to collect diffraction patterns without considerable aberrations with respect to peak shape and peak position at large tilt angles [22,23].

Synchrotron X-ray diffraction measurements were carried out at the surface diffraction beamline at the Ångström-Quelle Karlsruhe (ANKA). The X-ray source is a dipole bending magnet with a critical energy of 6.2 keV. For the adjustment of equatorial divergence and wavelength a rhodium-coated silicon X-ray mirror and a double-crystal silicon monochromator were employed, respectively. For details about the setup of this beamline, see Ref. [24]. The photon energy was preset to a value of about 10 keV (see Figure 4.1). At this energy the linear absorption coefficient of Cu is relatively high, thus allowing access to very small penetration depths without using small beam incidence angles and corrections for refraction.

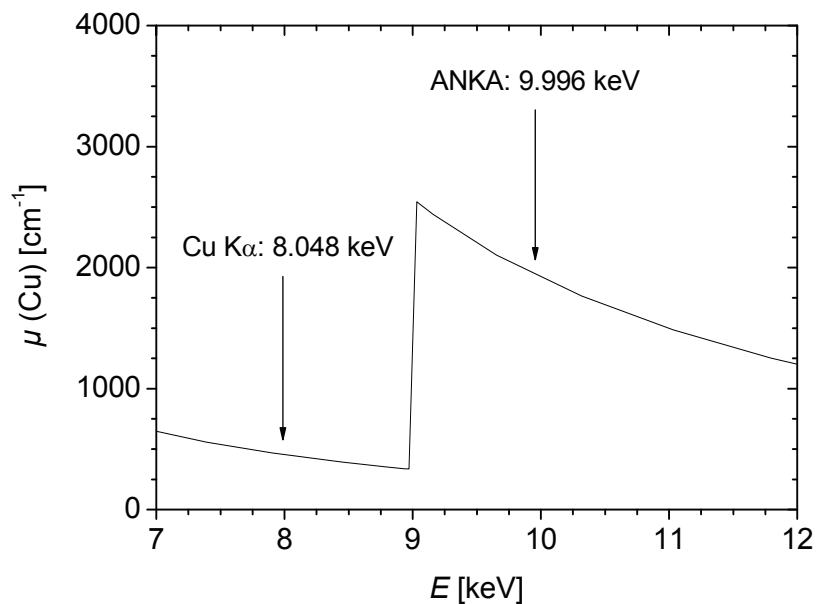


**Figure 4.1.** Linear absorption coefficient of copper as a function of photon energy (data from Ref. [25]) The K-absorption edge lies at 8.9789 keV. Measurements at the surface diffraction beamline at ANKA were performed at a photon energy of 9.996 keV; the laboratory diffraction measurements were carried out at a photon energy of 8.048 keV.



Five different diffraction lines were collected: 111, 200, 220, 311 and 222. At the synchrotron beamline measurements at penetration depths of 200 nm and 500 nm (corresponding to information depths of 200 and 498 nm) were performed, whereas at the laboratory diffractometer measurements were carried out at penetration depths of 500, 1000, 1500, 2000 and 2500 nm (corresponding to information depths of 498, 912, 1170, 1330 and 1430 nm). Diffraction patterns were evaluated by fitting Pearson VII functions (for a definition of the profile function, see Ref. [26]), using a custom peak fitting program. Peak positions, peak intensities, full-widths at half maximum and shape parameters were refined. For the laboratory measurements, the  $K\alpha_2$  component was taken into account by fitting two profile functions, one for each radiation component. A  $K\alpha_2$  to  $K\alpha_1$  intensity ratio of 0.5 was assumed. For each diffraction peak a linear background was fitted.

## 4.4. Results and Discussion

### 4.4.1. Grain morphology and film thickness

A micrograph obtained from the cut cross section is shown in Figure 4.2.

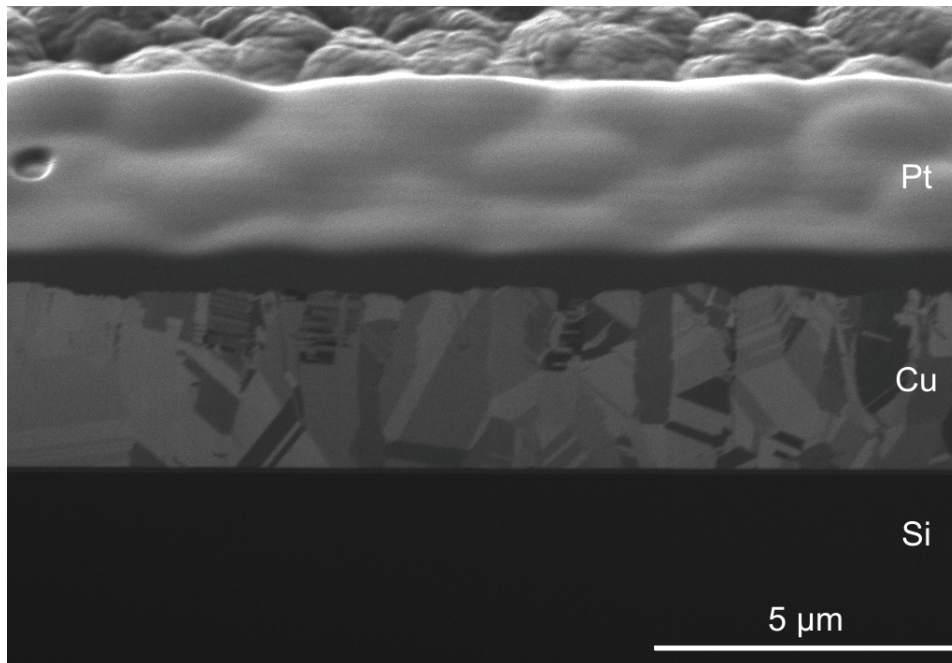


**Figure 4.2.** Focused ion beam image of the cross-section of the Cu thin film.

In the micrograph the protective platinum-layer, which was deposited onto the surface of the film, can be seen. Below this layer the microstructure of the film is well visible in the cross-section: Near the Si substrate the crystallites are rather large; some columnar grains extend almost from the substrate to the surface, but equiaxed grains occur also throughout the film. The mean effective film thickness was determined using image analysis software as  $t = 3.79 \mu\text{m}$ .

#### 4.4.2. Surface roughness

A three-dimensional perspective image of the specimen surface, as calculated from an AFM scan over an area of  $50 \mu\text{m} \times 50 \mu\text{m}$ , is shown in Figure 4.3. From the AFM analysis the following roughness values were obtained:

$$R_a = 63.9(4) \text{ nm}$$

$$R_{\text{ms}} = 80.9(6) \text{ nm}$$

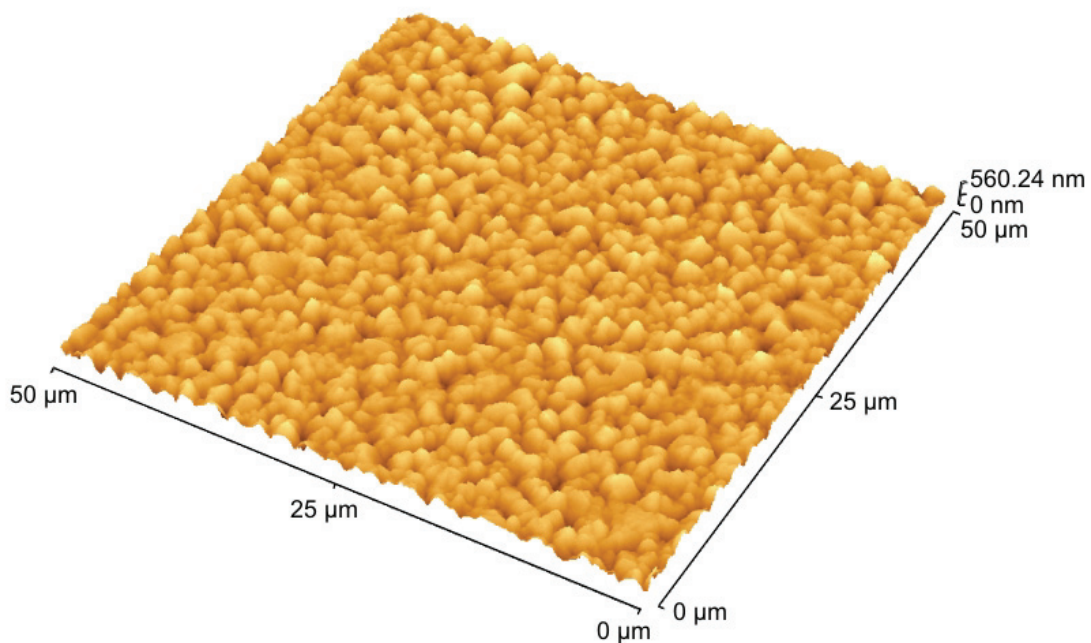


**Figure 4.3.** Perspective image of the specimen surface as measured by AFM.

#### 4.4.3. Crystallographic texture

Application of the  $f(\psi, hkl)$ -method requires a *macroscopically* elastically isotropic specimen which exhibits a rotationally symmetric state of stress. Thus, the degree of crystallographic texture of the specimen should be negligible (for details, see Ref.

[3]). A pole figure of the 111 reflection and the corresponding section at  $\varphi = 0^\circ$  are displayed in Figure 4.4.

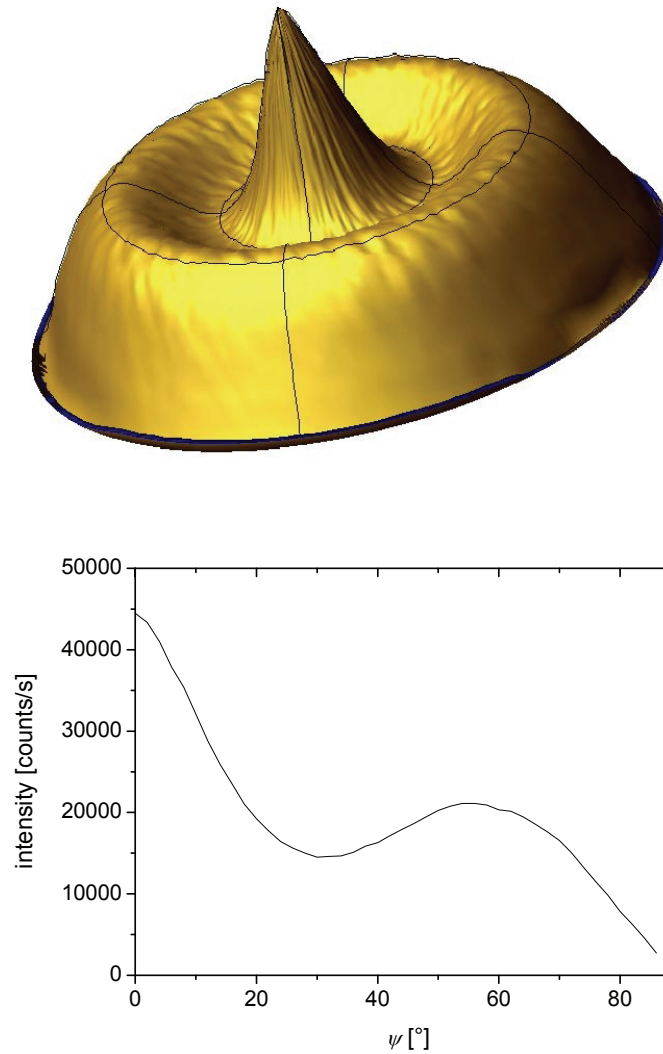


**Figure 4.4.** Measured  $\{111\}$  pole figure of the Cu specimen (top) and the corresponding pole-figure section at  $\varphi = 0^\circ$  (bottom).

It follows that the specimen exhibits a rather weak  $\{111\}$  fibre texture. It is thus concluded that the texture of the specimen can be neglected in the further analysis.

#### 4.4.4. Stresses and grain interaction as function of depth

Due to the film deposition process and due to the fibre nature of the (rather weak) texture a rotationally symmetric state of stress prevails. Evaluations of the diffraction data obtained in the laboratory and at the synchrotron are presented in Figure 4.5 and Figure 4.6, respectively. The straight lines shown in the figures represent least-squares fits of  $d_{\psi}^{hkl} (h^2 + k^2 + l^2)^{1/2}$ , with  $\langle \sigma_{\parallel}^S \rangle$ ,  $w$ , and an instrumental offset in the  $2\theta$ -scale as fitting parameters, according to the  $f(\psi, hkl)$ -method for different grain interaction models.

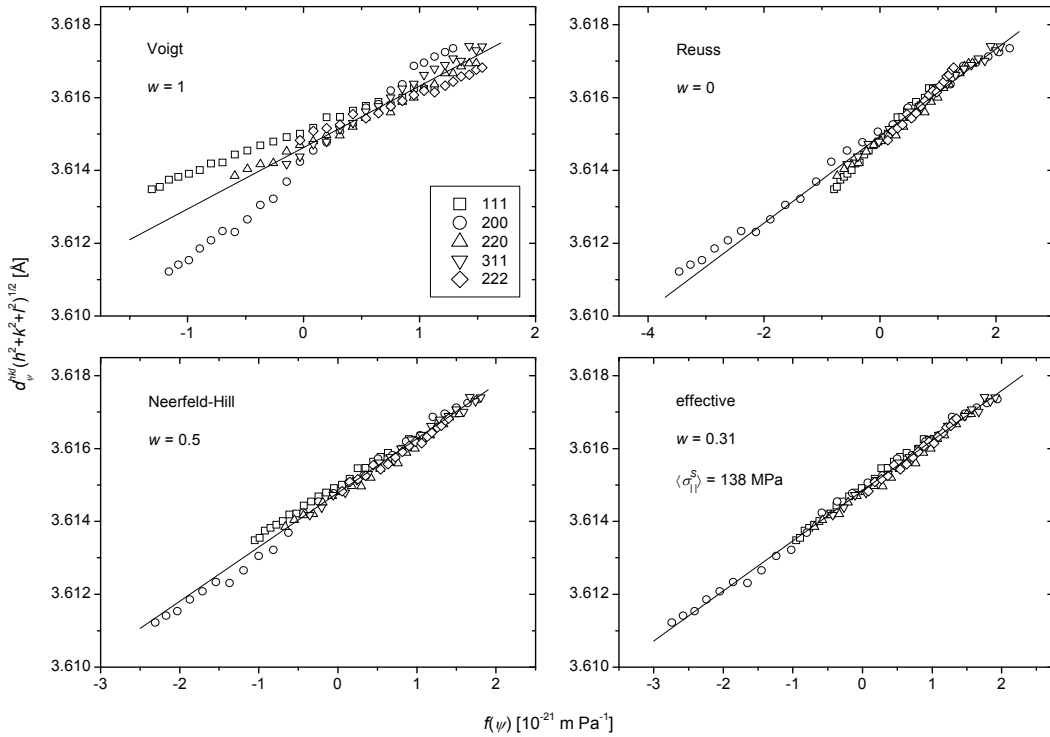


**Figure 4.5.** Plot of  $d_{\psi}^{hkl} (h^2 + k^2 + l^2)^{1/2}$  values measured in the laboratory at a penetration depth of  $\tau = 1500 \text{ nm}$  versus  $f(\psi)$  for the Voigt, Reuss, Neerfeld-Hill and the effective grain-interaction model. The determined effective grain-interaction parameter is 0.31 and the stress is 138 MPa. Error bars have been omitted as their size is of the order of the symbol size.

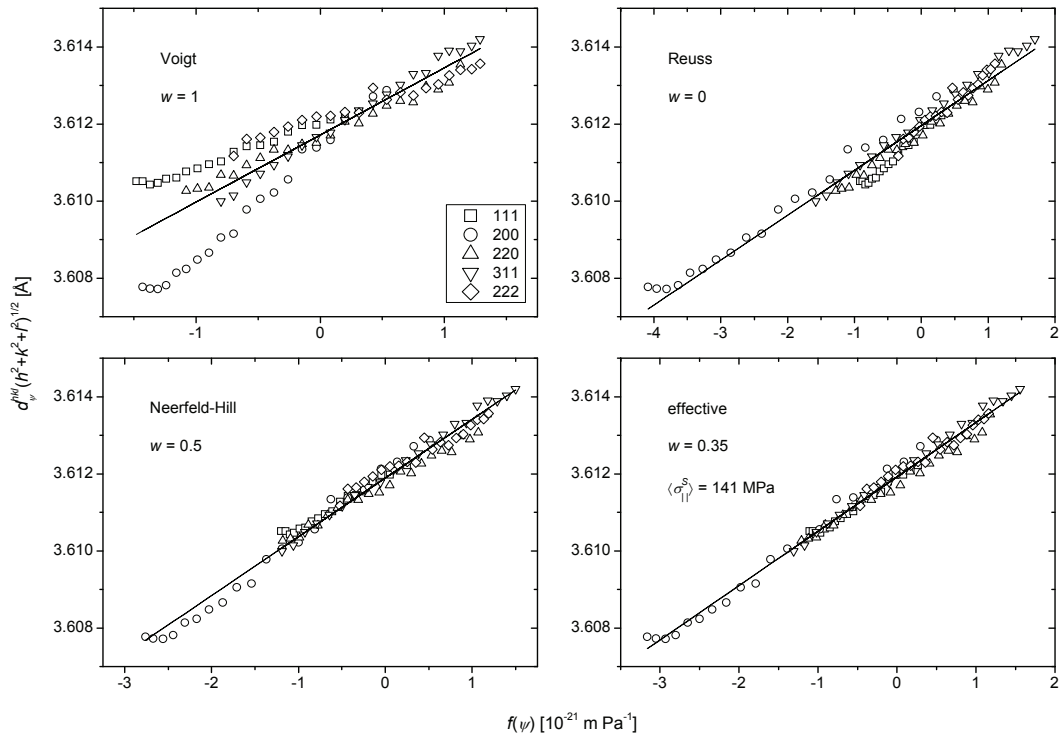


**Figure 4.6.** Plot of  $d_v^{hk} (h^2 + k^2 + l^2)^{1/2}$  values measured at the synchrotron at a penetration depth of  $\tau = 500$  nm versus  $f(\psi)$  for the Voigt, Reuss, Neerfeld-Hill and the effective grain-interaction model. The determined effective grain-interaction parameter is 0.35 and the stress is 141 MPa. Error bars have been omitted as their size is of the order of the symbol size.

It follows that the best fits result adopting the effective, intermediate grain-interaction model (see Figure 4.5 and Figure 4.6). The worst fit is obtained adopting the Voigt model for grain interaction. This implies that the Voigt model represents the least realistic description of the elastic behaviour of the polycrystalline aggregate (see also [15]). The determined instrumental offsets in the  $2\theta$ -scale were consistent with each other for each instrumental setup employed.

None of the  $f(\psi)$ -plots according to the effective grain-interaction model exhibits a distinct curvature, which is compatible with absence of additional effects due to direction-dependent grain interaction and crystallographic texture (see also chapter 4.4.3; for details about direction-dependent grain interaction, see Refs. [3,27]).

It has been shown previously for Ni thin films that the in-plane and out-of-plane grain-interaction parameters at a certain information depth do not differ substantially from each other when they are determined independently [28]. Hence in

this work the in-plane and out-of-plane grain-interaction parameters have been taken as equal. The excellent fit results obtained in the  $f(\psi)$ -plots employing the effective grain-interaction model confirm that the grain interaction could be well modelled in this way.

The residual stresses and the grain-interaction parameters, which have been determined by fitting in  $f(\psi)$ -plots as determined above and adopting the effective grain-interaction model, have been plotted versus the information depth  $\xi$  in Figure 4.7 and Figure 4.8, respectively. The laboratory measurement at  $\tau = 500$  nm involved the use of small angles of incidence (as low as  $1.4^\circ$ ). Whereas a correction for refraction is not required for the laboratory measurements at larger information depths, at incidence angles below about  $2.5^\circ$  refraction is no longer negligible and has to be corrected for. However, if the roughness of the specimen is relatively large application of the refraction correction method valid for a flat surface leads to an overestimation of the refraction correction (cf. chapter 4.2.2 and see also Ref. [29]). This is illustrated by the effect of the used refraction correction applied to the obtained stress and grain-interaction parameter for the laboratory measurement at  $\tau = 500$  nm and comparing the results obtained after such refraction correction of the laboratory measurements with the uncorrected (unnecessary because of high angles of incidence) synchrotron measurements at the same penetration depth (see Figure 4.7 and Figure 4.8). The synchrotron measurements at the same penetration depth yield values for the stress and the grain-interaction parameter which are compatible with the extrapolated trend derived from the laboratory measurements at larger penetration depths. Evidently, the overestimation of the refraction correction at small incident beam angles is due to the specimen roughness, which effectively reduces the actually occurring amount of refraction.

The results demonstrate that X-ray diffraction measurements at constant penetration depth should only be conducted at sufficiently large incidence angles ( $\alpha > 2.5^\circ$ ), unless the roughness of the specimen under investigation is very small (of the order of nm's). To investigate small penetration depths the X-ray penetration should be tuned, by varying the photon energy, such that the absorption coefficient (and thereby the required incidence angles) is (are) large enough.

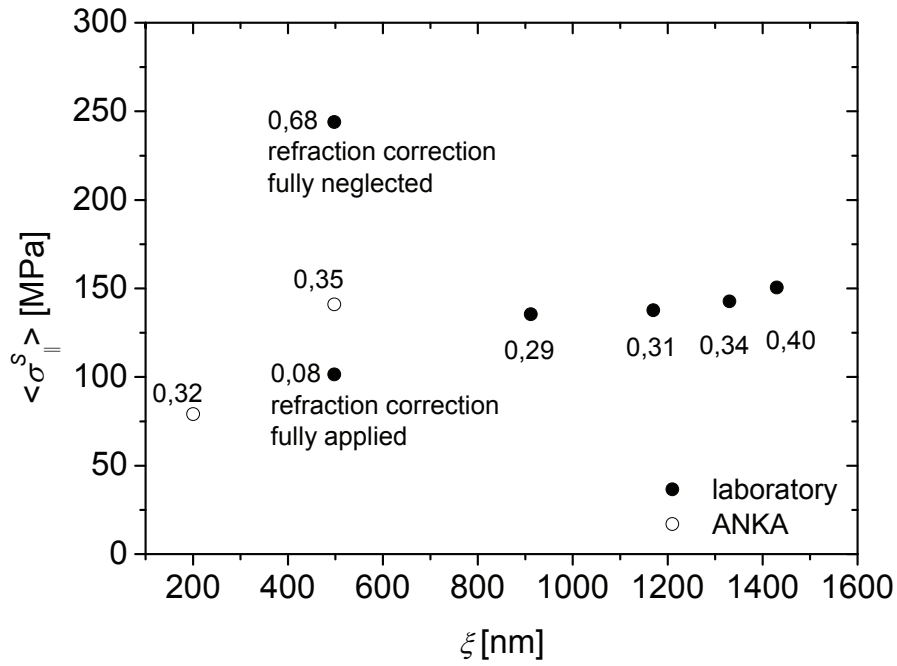


**Figure 4.7.** Residual stress as function of information depth, as derived from the effective grain-interaction model. The evaluation of the laboratory measurement at the smallest depth has been carried out twice – with and without applying the refraction correction. Error bars have been omitted as their size is of the order of the symbol size.

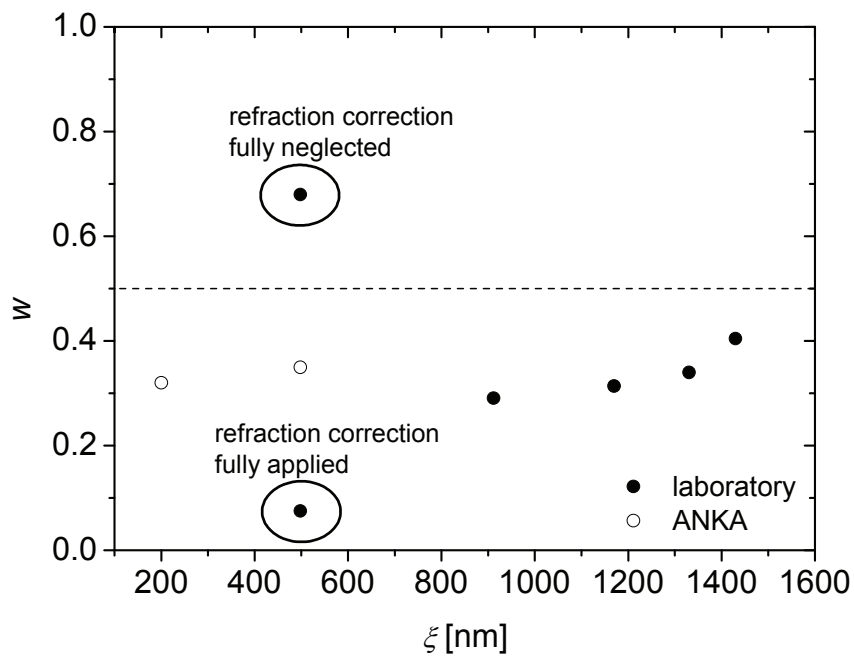


**Figure 4.8.** Grain-interaction parameter  $w$  as function of information depth  $\xi$ . The evaluation of the laboratory measurement at the smallest depth has been carried out twice – with and without applying the refraction correction. Error bars have been omitted as their size is of the order of the symbol size.

Evidently, the two-step deposition process generated a change of stress from about 80 MPa close to the surface to about 150 MPa in the middle of the film (see Figure 4.7). The tensile nature of the residual stress can be caused by the thermal misfit due to the difference between the coefficients of thermal expansion of thin film and substrate. The residual stress values measured up to an information depth of about 1500 nm (i.e. less than half of the total film thickness), however, are significantly lower than the theoretically expected thermal residual stress which would develop upon cooling to room temperature in a Cu film deposited on Si at 400 °C (about 1 GPa; [30,31]). This can be ascribed to (a combination of) various causes: (i) The deposition temperature was measured on the back of the substrate; a non-negligible temperature gradient through the thickness of the substrate cannot be excluded and thus the actual deposition temperature on top of the substrate during deposition of the bottom layer may have been lower than the preset deposition temperature. (ii) Compressive intrinsic stresses may occur as a result of the atomic peening effect [32], causing a reduction of the thermal tensile stress level. (iii) The thermal stress induced by cooling after deposition of the bottom layer may have been partially accommodated plastically during the cooling back to room temperature, particularly in the first stage of the cooling process, where the mobility of the atoms is still relatively high. This last mechanism indeed is very likely for the as-deposited bottom layer (thickness 2  $\mu\text{m}$ ), as the onset of plastic deformation for Cu thin films exhibiting a stabilized microstructure and comparable thickness (1  $\mu\text{m}$ ) has been found at stress levels between 150 and 200 MPa, depending on the type of atmosphere [33].

The tensile residual stress parallel to the surface becomes smaller close to the specimen surface. This can be considered as a consequence of the surface roughness: the in-plane residual stress can relax at outer edges, ridges, etc. on the surface.

As the maximum reachable information depth can only be half of the film thickness [19], the stress depth profile in the bottom layer can not be determined experimentally.

The results shown in Figure 4.8 indicate that for all depths investigated the effective grain interaction is more of Reuss-type ( $w = 0$ ) than of Voigt-type ( $w = 1$ ). Towards larger information depth there is a slight increase in  $w$ , indicating a more Neerfeld-Hill-type interaction ( $w = 1/2$ ) at larger depth. This can be understood for two types of grain morphology as follows:



(i) At the interface to the substrate the (thermal) misfit is transferred to the film, i.e. at the base of the grains the strain is likely to be equal for all grains. The columnar grain boundaries in thin films sputter-deposited at low and moderate homologous temperatures  $T_h$  ( $T_h \leq 0.5$ ; for details, see Ref. [32]) have a rather ‘open’ structure, i.e. the crystallites can deform more or less freely in the in-plane directions (perpendicular to the grain boundaries). Thus, with increasing distance from the interface between substrate and film, i.e. with decreasing information depth, a transition from equal in-plane strain (Voigt-type interaction) to equal in-plane stress (Reuss-type interaction) occurs for these columnar grains.

(ii) For a bulk polycrystal a different type of grain interaction is expected. In this case neither the grain boundaries constitute an ‘open’ structure nor does a rigid substrate transfer any misfit strain. Thus, the arithmetic average between the two extreme grain-interaction models after Voigt and Reus, i.e. the Neerfeld-Hill model, represents a realistic approximation of the elastic behaviour of a bulk polycrystal. Hence, the same (Neerfeld-Hill type of) elastic behaviour is expected for a dense thin film consisting of many equiaxed crystallites not traversing the film thickness. This implies that the grain interaction perpendicular to the thin film surface (i.e. across grain boundaries not consisting of an open structure) can be conceived to be also of Neerfeld-Hill type. With decreasing information depth the fraction of surface-adjacent crystallites probed increases. These crystallites are surrounded by other crystallites only in two dimensions separated by columnar grain boundaries. Consequently, they can deform more freely in the direction perpendicular to the film surface having equal stress values in this direction (= nil) and thus a more Reuss-type interaction occurs near the surface.

The actual grain morphology of the current Cu thin film can be interpreted as an intermediate of the two cases, (i) and (ii), considered above. The same trend for  $w$  is predicted in both cases (decrease of  $w$  with decreasing information depth), which is well compatible with the experimental results (Figure 4.8).

## 4.5. Conclusions

- A diffraction method to simultaneously determine the depth gradients of stress and grain interaction has been developed. To this end, a modified version of the  $f(\psi, hkl)$ -method has been employed allowing, at constant penetration/information depth, determination of the stress, the grain-interaction parameter and the instrumental  $2\theta$  offset, utilizing a series of  $hkl$  reflections.
- The two-step deposition process led to a change of stress from 80 MPa near the surface to 150 MPa in the middle of the Cu film.
- The amount and tensile nature of the residual stress in the Cu film are most likely explained by built-up of thermal residual stress during cooling and subsequent plastic deformation.
- The grain interaction is generally more of Reuss-type than of Voigt-type. With decreasing information depth the Reuss-type character of the grain interaction increases. This finding is explained by the specimen's microstructure: With increasing distance from interface with the substrate the grains can deform more independently either because the grain boundaries of the columnar grains have a rather 'open' structure due to the deposition process, or because, for the equiaxed grains, the fraction of surface-adjacent crystallites probed increases; such crystallites can additionally deform freely in the direction perpendicular to the surface. For both types of grains Reuss-type interaction is presumed near the surface.
- The specimen surface roughness reduces the effect of refraction such that for measurements employing small incidence angles, in order to realize small penetration/information depths, erroneous values for grain interaction and stress are obtained *without* and *with* application of a refraction correction. Diffraction measurements at small information depths should rather be

realized by enhancing the absorption, i.e. by variation of the wavelength; the use of small incidence angles (say,  $< 2.5^\circ$ ) should be avoided.

## **Acknowledgements**

The assistance given by Mr R. Weigel and Dr A. Stierle for the measurements using synchrotron radiation at ANKA is gratefully acknowledged.

## References

- [1] Noyan, I.C. & Cohen, J.B. (1987). *Residual Stress: Measurements by Diffraction and Interpretation*. New York: Springer.
- [2] Hauk, V. (1997). Editors. *Structural and Residual Stress Analysis by Nondestructive Methods*, Amsterdam: Elsevier.
- [3] Welzel, U., Ligot, J., Lamparter, P., Vermeulen, A.C. & Mittemeijer, E.J. (2005). *J. Appl. Cryst.* **38**, 1.
- [4] Welzel, U. & Mittemeijer, E.J. (2003). *J. Appl. Phys.* **93**, 9001.
- [5] Bollenrath, F., Hauk, V. & Müller, E.H. (1967). *Z. Metallkd.* **58**, 76.
- [6] Voigt, W. (1910). *Lehrbuch der Kristallphysik*. Leipzig: Teubner.
- [7] Reuss, A. (1929). *Z. Angew. Math. Mech.* **9**, 49.
- [8] Serruys, W., van Houtte, P. & Aernoudt, E. (1987). *X-ray measurement of residual stresses in textured materials with the aid of orientation distribution functions*, in: *Residual stresses in science and technology*, edited by E. Macherauch & V. Hauk, Vol. Oberursel: Deutsche Gesellschaft für Metallkunde.
- [9] Serruys, W., Langouche, F., van Houtte, P. & Aernoudt, E. (1989). *Calculation of X-ray elastic constants in isotropic and textured materials*, in: *Proceedings of ICRS 2*, edited by G. Beck, S. Denis & A. Simon, Vol. pp. 166. London: Elsevier Applied Science.
- [10] Welzel, U., Leoni, M. & Mittemeijer, E. J. (2003). *Philos. Mag.* **83**, 603.
- [11] Neerfeld, H. (1942). *Mitt. K.-Wilh.-Inst. Eisenforschg.* **24**, 61.
- [12] Hill, R. (1952). *P. Phys. Soc. Lond. A* **65**, 349.
- [13] Vermeulen, A. C. (2002). *Mater. Sci. Forum* **404-407**, 35.
- [14] Quaeysaegens, C., Knuyt, G. & Stals, L. M. (1995). *Surf. Coat. Technol.* **74-75**, 104.
- [15] Kamminga, J.-D., de Keijser, Th. H., Mittemeijer, E.J. & Delhez, R. (2000). *J. Appl. Cryst.* **33**, 1059.
- [16] Malhotra, S.G., Rek, Z.U., Yalisove, S.M. & Bilello, J.C. (1997). *Thin Solid Films* **301**, 55.
- [17] Delhez, R., de Keijser, Th. H. & Mittemeijer, E. J. (1987). *Surf. Eng.* **3**, 331.
- [18] Genzel, Ch. (1997). *Phys. Status Solidi A* **159**, 283.

- [19] Kumar, A., Welzel, U. & Mittemeijer, E. J. (2006). *J. Appl. Cryst.* **39**, 633.
- [20] Genzel, C. (2005). *Mater. Sci. Technol.* **21**, 10.
- [21] Ott, M. H. & Löhe, D. (2002). *Mater. Sci. Forum* **404-407**, 25.
- [22] Welzel, U. & Leoni, M. (2002). *J. Appl. Cryst.* **35**, 196.
- [23] Leoni, M., Welzel, U. & Scardi, P. (2004). *J. Res. Natl. Inst. Stand. Technol.* **109**, 27.
- [24] Stierle, A., Steinhäuser, A., Rühm, A., Renner, F.U., Weigel, R., Kasper, N. & Dosch, H. (2004). *Rev. Sci. Instrum.* **75**, 5302.
- [25] Chantler, C.T., Olsen, K., Dragoset, R.A., Chang, J., Kishore, A.R., Kotochigova, S.A. & Zucker, D.S. (2005). *X-ray Form Factor, Attenuation, and Scattering Tables (version 2.1)*, <http://physics.nist.gov/ffast> (February 27th, 2008). National Institute of Standards and Technology, Gaithersburg, MD.
- [26] Sonneveld, E. J., Delhez, R., De Keijser, Th. H. & Mittemeijer, E. J. (1991). *Mater. Sci. Forum* **79-82**, 85.
- [27] Welzel, U., Fréour, S. & Mittemeijer, E. J. (2005). *Philos. Mag.* **85**, 2391.
- [28] Kumar, A., Welzel, U. & Mittemeijer, E.J. (2006). *J. Appl. Phys.* **100**, 114904.
- [29] Leung, O. S., Munkholm, A., Brennan, S. & Nix, W. D. (2000). *J. Appl. Phys.* **88**, 1389.
- [30] Touloukian, Y. S., Kirby, R. K., Taylor, R. E. & Desai, P. D. (1975). *Thermal Expansion, Metallic Elements and Alloys*. New York: IFI/Plenum.
- [31] Touloukian, Y. S., Kirby, R. K., Taylor, R. E. & Lee, T. Y. R. (1977). *Thermal Expansion, Nonmetallic Solids*. New York: IFI/Plenum.
- [32] Ohring, M. (2002). *The Materials Science of Thin Films*. New York: Academic Press.
- [33] Keller, R.-M., Baker, S. P. & Arzt, E. (1999). *Acta Mater.* **47**, 415.



## **5. Residual stress and strain-free lattice-parameter depth profiles in a $\gamma'$ -Fe<sub>4</sub>N<sub>1-x</sub> layer on an $\alpha$ -Fe substrate measured by X-ray diffraction stress analysis at constant information depth**

*M. Wohlschlägel, U. Welzel and E.J. Mittemeijer*

### **Abstract**

The residual stress and lattice-parameter depth profiles in a  $\gamma'$ -Fe<sub>4</sub>N<sub>1-x</sub> layer (thickness 6  $\mu\text{m}$ ) grown on top of an  $\alpha$ -Fe substrate were investigated employing X-ray diffraction stress analysis at constant penetration depths. Three different reflections (220, 311 and 222) were recorded at six different penetration depths using three different wavelengths. At each penetration depth X-ray diffraction stress analysis was performed on the basis of the  $\sin^2\psi$  method. As a result the residual stress depth profile was obtained from the measured lattice strains. The lattice spacings measured in the strain-free direction were used to determine the (strain-free) lattice-parameter depth profile. The nitrogen concentration depth profile in the layer was calculated by applying a relationship between the (strain-free)  $\gamma'$  lattice parameter and the nitrogen concentration. It was found that the strain-free lattice-parameter depth profile as derived from the 311 reflections is best compatible with nitrogen concentrations at the surface and at the  $\gamma'/\alpha$  interface as predicted on the basis of local thermodynamic equilibrium. It could be shown that the 311 reflection is most suitable for the analysis of lattice-parameter and residual stress depth profiles because the corresponding X-ray elastic constants exhibit the least sensitivity to the type of and changes in grain interaction.

## 5.1. Introduction

Gas nitriding is a well known thermochemical treatment for workpieces made of iron and iron-based alloys. Depending on time, temperature and composition of the gas atmosphere the iron-nitride layer which develops on the surface of the workpiece during this treatment induces favourable properties like high hardness and enhanced resistance to corrosion and wear [1]. Typically such compound layers consist of  $\epsilon$ - $\text{Fe}_2\text{N}_{1-x}$  (hexagonally close packed arrangement of iron atoms) and  $\gamma'$ - $\text{Fe}_4\text{N}_{1-x}$  (face centred cubic arrangement of iron atoms). The nitrogen atoms in both phases occupy octahedral interstitial sites exhibiting specific long-range ordering [2-4]. For the phase  $\gamma'$  studied in this work the homogeneity range is rather small, i.e. at 823 K between 19.58 and 19.93 at.% N [5,6].

$\gamma'$  iron nitride has gained growing importance due to its interesting magnetic properties in the form of thin films [7-10]. Recently it has been shown that  $\gamma'$  possesses an elastic anisotropy which is abnormal for fcc-type materials: Its Zener anisotropy ratio is smaller than 1, yielding  $\langle 100 \rangle$  as stiffest and  $\langle 111 \rangle$  as most compliant direction [11].

In the past, a number of studies have been conducted concerning the growth kinetics of and the phase transformations occurring within the  $\gamma'$  iron-nitride layer [6,12-14]. Furthermore, the formation of  $\gamma'$  thin films has been studied in a number of works and different production processes as gas assisted molecular-beam epitaxy, reactive sputtering, laser nitriding of bulk-iron and gas nitriding of iron thin films have been investigated [8,10,15] (see also chapter 3).

Previous work identified the nitrogen concentration profile and thermal misfit as stress built-up mechanisms as well as pore development and phase transformations, like the precipitation of  $\alpha$ -Fe during slow cooling after nitriding, as stress relaxation mechanisms [16,17].

Residual stress gradients can be measured employing a number of different methods. The typical non-destructive stress measurement technique is (X-ray) diffraction, where lattice strains are measured and related to a residual macrostress (mechanical stress) employing suitable elastic constants as X-ray stress factors or, provided the specimen is macroscopically elastically isotropic (quasi-isotropic), X-ray elastic constants (XECs) [18-20]. XECs can be deduced from single crystal elastic



constants applying a suitable grain-interaction model. A common technique to obtain a realistic grain-interaction model is to mix two (or more) extreme grain-interaction models, like the Voigt- and the Reuss-model [20-24].

Traditionally, layer-removal techniques such as grinding and polishing, in combination with X-ray diffraction, have been adopted in order to determine the depth dependence of the residual stress [25,26]. By this approach it is possible to investigate practically every depth-range, thereby, however, destroying the specimen. A comprehensive description of this approach and its application to a  $\gamma'$  iron-nitride layer is provided by Ref. [16].

For the non-destructive analysis of residual stress depth profiles a number of diffraction methods has been proposed in the past [27-35]. These methods can generally be subdivided into two groups: In one group of methods it is recognized that the penetration depth varies during one diffraction stress measurement and the stress depth dependence is analyzed by utilizing the variation of the penetration depth during the stress measurement and thus obtaining information about the stress depth profile. In the other group of methods the penetration depth is kept constant during one diffraction stress measurement and information on the stress depth profile is obtained from several stress measurements at constant penetration depth.

Kumar *et al.* [36] recently proposed such a measurement strategy, where residual stress depth profiles can be determined non-destructively by (X-ray) diffraction tuned at (several) constant penetration depth(s). Adopting this approach it is possible to determine the residual stress depth profile within a specimen up to a certain depth which is determined by the linear absorption coefficient of the material. By a combination of different wavelengths, depending on the wavelengths corresponding to the absorption edges, the possible depth range can be extended.

In this work the residual stress depth profile in a  $\gamma'$ -Fe<sub>4</sub>N<sub>1-x</sub> layer grown on an  $\alpha$ -Fe substrate has been investigated by X-ray diffraction stress analysis (XRSA) at constant information depth. It has been shown that the type of grain-interaction within the layer changes from Voigt-type to Reuss-type with increasing depth. This finding has been made plausible considering the specimen microstructure. Moreover, the strain-free lattice parameter depth profile has been deduced from the measured data and related to the variation of nitrogen concentration with depth. It followed that the boundary concentrations of the thus obtained nitrogen concentration depth profile

match well those expected assuming local thermodynamic equilibrium at the layer surface and at the interface of layer and substrate.

## 5.2. Theoretical background

In the following subsections the theoretical principles employed in this work are described. Firstly, the fundamentals of X-ray residual stress analysis (XRSA) are indicated and, secondly, the two basic, isotropic models for elastic grain-interaction, namely the Voigt [21] and Reuss [22] models, are explained. Thirdly, the method of XRSA at constant penetration depth and the resulting determination of residual stress depth profiles are explained.

### 5.2.1. X-ray residual stress analysis (XRSA)

In general, the components of the mechanical stress tensor can be determined from X-ray diffraction measurements of lattice strains in several measurement directions ( $\varphi$ ,  $\psi$ ), where  $\varphi$  is the rotational angle of the diffraction vector around the sample surface normal and  $\psi$  is the tilt angle of the diffraction vector with respect to the sample surface normal, according to the  $\sin^2\psi$  method [18,20]. If certain simplifications with respect to the state of stress can be applied, the number of components of the stress tensor and thus the number of lattice strains necessary to determine the stress state is reduced and the corresponding  $\sin^2\psi$  law becomes simplified. In case of a macroscopically elastically isotropic specimen subjected to a planar, rotationally symmetric state of stress the  $\sin^2\psi$  law reads [20]:

$$\varepsilon_{\psi}^{hkl} = \frac{d_{\psi}^{hkl} - d_0^{hkl}}{d_0^{hkl}} = \left( 2S_1^{hkl} + \frac{1}{2}S_2^{hkl} \sin^2\psi \right) \sigma_{\parallel}, \quad (5.1)$$

where  $\varepsilon_{\psi}^{hkl}$  is the strain of the  $hkl$  lattice planes,  $d_{\psi}^{hkl}$  and  $d_0^{hkl}$  are the strained and strain-free lattice spacings of the  $hkl$  lattice planes, respectively,  $S_1^{hkl}$  and  $1/2S_2^{hkl}$  are the XECs,  $\psi$  denotes the measurement direction and  $\sigma_{\parallel} = \sigma_{11} = \sigma_{22}$  represents the mechanical in-plane residual stress. Hence, when  $d_{\psi}^{hkl}$  is plotted versus  $\sin^2\psi$ , the stress follows from the division of the slope of the interpolated straight line by  $d_0^{hkl}$  and  $1/2S_2^{hkl}$ .

The strain-free direction  $\sin^2 \psi_0$  is obtained when equation (5.1) is set equal to zero. It follows:

$$\sin^2 \psi_0 = \frac{-2S_1^{hkl}}{1/2 S_2^{hkl}}, \quad (5.2)$$

i.e. the strain-free lattice spacing  $d_0^{hkl}$  can be determined by linear interpolation of  $d_{\psi}^{hkl}$  versus  $\sin^2 \psi$  at  $\sin^2 \psi_0$ .

### 5.2.2. Grain-interaction models

In general the elastic interaction between individual grains in a polycrystalline aggregate is direction-dependent [19]. In the present study the grain interaction can be considered as isotropic (cf. chapter 5.4.2). Then the Voigt and Reuss models represent the two extreme types of grain interaction. In the specimen frame of reference the Voigt model assumes that all crystallites of a polycrystalline specimen are subjected to an equal state of strain, whereas the Reuss model is based on the postulation that all crystallites have the same state of stress. Both extremes of grain interaction lead to incompatibilities at the grain boundaries - in the Voigt model a stress mismatch occurs, whereas the Reuss model involves a strain mismatch. Hence, neither the Voigt model nor the Reuss model complies with the real elastic behaviour of a polycrystal. Thus, effective grain interaction models have been proposed to overcome these discrepancies [19,20,37-39]. An effective grain interaction model is constructed as the weighted sum of a number of extreme grain interaction models. In the present case of isotropic grain interaction the effective grain-interaction model implies that the actual XECs are given by:

$$S_i^{hkl} = wS_i^V + (1-w)S_i^{R,hkl}, \quad (5.3)$$

where  $S_i^{hkl}$  ( $i = 1, 2$ ) is the effective XEC,  $S_i^V$  and  $S_i^{R,hkl}$  are the XECs according to the Voigt model and the Reuss model, respectively and  $w$  is a weighing factor. Note that the XECs after Voigt are *isotropic*, i.e. they do not depend on  $hkl$ , whereas the XECs after Reuss are *anisotropic*, i.e. they do depend on  $hkl$ . A well known effective grain interaction model which is frequently employed is the Neerfeld-Hill model [23,24], which uses the arithmetic average of the Voigt and Reuss models (i.e.  $w = 0.5$ ) to describe the effective XECs. However, as shown in recent work (cf. chapter 4),

$w$  can take any value within  $w \in [0,1]$  and in thin films even a depth dependence of these weighing parameters can occur [40].

### 5.2.3. Determination of real-space depth profiles from XRSA at constant penetration/information depth

A typical XRSA on the basis of the  $\sin^2\psi$  method involves the measurement of lattice spacings at various angles  $\psi$  employing either the  $\omega$  mode or the  $\chi$  mode, where the angle  $\psi$  is set via the instrumental angles  $\omega$  and  $\chi$ , respectively [20]. Either of these methods involves a change of X-ray penetration depth during the course of one measurement, i.e. the data points obtained in the  $\sin^2\psi$  plot for a particular  $hkl$  reflection correspond to different penetration depths.<sup>a</sup> Thus, if stress gradients are present and their occurrence is not taken into account in the stress evaluation erroneous results will in general be obtained. Even in the absence of stresses a lattice-parameter depth profile can result in an apparent stress state (i.e. a  $\sin^2\psi$ -plot with a non-zero slope is obtained); this effect is often referred to as “ghost stresses” (see, for example Ref. [16] and references therein).

The *penetration depth*  $\tau$  is the centre of gravity of the distribution of measured diffracted intensity versus depth for an infinitely thick, homogenous specimen. About 63% of the diffracted intensity stems from a volume confined by  $\tau$  below the sample surface [36,42]. The penetration depth is given by incidence angle  $\alpha$  and exit angle  $\beta$  of incident and diffracted beam, respectively, and by the linear absorption coefficient  $\mu$  according to [31,36]:

$$\tau = \frac{\sin \alpha \sin \beta}{\mu(\sin \alpha + \sin \beta)}. \quad (5.4)$$

The *information depth*  $\xi$  is the centre of gravity of the distribution of diffracted intensity versus depth for a particular specimen with finite thickness  $t$ . The diffracted intensity originating from each depth  $z$  has to be weighted by an absorption factor. This absorption factor accounts for intensity reduction of both the incoming beam and the diffracted beam for the signal originating from depth  $z$ . It thus follows [42]:

---

<sup>a</sup> For (cumbersome) methods for the determination of real-space depth profiles on the basis of such  $\sin^2\psi$ -plots, see Refs. [28,34,41]

$$\xi(t) = \langle z \rangle = \frac{\int_0^t z \exp(-z/\tau) dz}{\int_0^t \exp(-z/\tau) dz} = \tau - \frac{t \exp(-t/\tau)}{1 - \exp(-t/\tau)}, \quad (5.5)$$

where brackets “ $\langle \rangle$ ” indicate averaging. The following limits hold:

$$\lim_{t/\tau \rightarrow 0} \xi(t) = \frac{1}{2}t \quad (5.6)$$

and

$$\lim_{t/\tau \rightarrow \infty} \xi(t) = \tau. \quad (5.7)$$

It follows that the maximum achievable information depth is half of the specimen thickness (cf. equation (5.6)).

Both the penetration depth and, consequently, the information depth can be kept constant during the course of a residual stress measurement by selection of appropriate incidence and exit angles (i.e. satisfying equation (5.4)) employing the so-called combined  $\omega/\chi$  mode proposed in Ref. [36], where the angle  $\psi$  is adjusted by a combination of the instrumental angles  $\omega$  and  $\chi$ . As a consequence of such measurements limitations with respect to the accessible  $\psi$ -range for a certain  $hkl$  reflection, penetration depth and wavelength occur [36].

The result of a diffraction analysis at constant information depth of any parameter, as residual stress, strain-free lattice-parameter and thus nitrogen concentration, is the Laplace transform of the corresponding real-space depth profile of this parameter (cf. equation (5.5)). In order to determine the real-space depth profiles of this parameter the following procedure has been employed:

A suitable real-space depth profile for the parameter concerned,  $\Xi(z)$ , is assumed and transformed into Laplace-space by application of:

$$\Xi(\tau) = \frac{\int_0^t \Xi(z) \exp(-z/\tau) dz}{\int_0^t \exp(-z/\tau) dz}, \quad (5.8)$$

To achieve high numerical accuracy, the assumed data points  $\Xi(z)$  are interpolated by a cubic spline and the integration in equation (5.8) is performed over the points returned by the spline function. The number of assumed data points  $\Xi(z)$  may only

exceed the number of measured points  $\Xi(\tau)$  if additional boundary conditions occur – of course, for the purpose of the numerical integration (equation (5.8)) the number of data points returned by the spline interpolation can be much higher.

Next, the resulting calculated Laplace-space depth profile,  $\Xi(\tau)$  is compared with the measured Laplace-space depth profile. The assumed points  $\Xi(z)$  are then adjusted successively such that the sum of squared differences between calculated and measured Laplace-space depth profile is reduced. This procedure is repeated until agreement of calculated and measured data in Laplace space occurs within a set limit of accuracy.

### 5.3. Experimental

#### 5.3.1. Specimen preparation

The specimen was prepared from a cold rolled  $\alpha$ -Fe (Alpha Aesar 99.98 wt%) cast rod in the form of a rectangular disc with an area of  $18 \times 25 \text{ mm}^2$  and a thickness of 1 mm. Before the nitriding treatment the specimen was recrystallized for 2 h at 973 K in a hydrogen atmosphere, mechanically polished up to 1  $\mu\text{m}$  diamond paste and ultrasonically cleaned in ethanol.

The nitriding treatment was performed in a vertical quartz-tube furnace at a temperature of 823 K using a gas mixture of  $\text{NH}_3$  (99.999 vol.%) and  $\text{H}_2$  (99.999 vol.%). The composition of the nitriding gas atmosphere was chosen as 43 vol.%  $\text{NH}_3$  / 57 vol.%  $\text{H}_2$  and the nitriding time was 5 h. Thus, a  $\gamma'$ - $\text{Fe}_4\text{N}_{1-x}$  compound layer with a thickness of about 6  $\mu\text{m}$  on top of the ferrite substrate was obtained [6]. After the nitriding process the specimen was quenched by dropping it into cold water flushed with nitrogen gas.

#### 5.3.2. Metallography

A cross section of the specimen was obtained by cutting using an Accutom-50 (Struers GmbH). The cut piece was galvanized with a protective nickel layer [43], embedded in Polyfast (Buehler GmbH), ground, polished down to 1  $\mu\text{m}$  diamond paste and etched in 1 vol.% Nital containing 0.1 vol.% HCl [44,45]. Optical microscopy was performed employing a Zeiss Axiophot microscope (Carl Zeiss

MicroImaging GmbH). Several micrographs of the specimen cross section were taken close to both faces of the specimen and the surface-layer thickness was determined as arithmetic average of multiple measurements using conventional image-analysis software.

### 5.3.3. X-ray diffractometry

Qualitative XRD phase analysis was performed using a Philips (now PANalytical) materials research diffractometer (MRD) equipped with an Eulerian cradle. Co K $\alpha$  radiation ( $\mu_{\text{Fe}_4\text{N,Cu}} \text{K}\alpha = 0.039 \text{ }\mu\text{m}^{-1}$ ; as calculated from data for Fe and N in Refs. [46,47]) emerging from the point focus of a sealed tube was converted into a quasi-parallel beam by an X-ray lens. The size of the incident beam was set to 4 mm  $\times$  4 mm by crossed slits. The residual divergence of the incident beam as conditioned by the X-ray lens was approximately 0.3°. The diffracted beam passed a parallel-plate collimator (acceptance angle 0.18°) before being detected by a gas proportional counter.

Near-surface XRD stress analysis was conducted employing a Bruker AXS D8 Discover diffractometer equipped with an Eulerian cradle. Cu K $\alpha$  radiation ( $\mu_{\text{Fe}_4\text{N,Cu}} \text{K}\alpha = 0.207 \text{ }\mu\text{m}^{-1}$ ; as calculated from data for Fe and N in Refs. [46,47]), emerging from the point focus of a rotating anode source (Bruker TXS) operating at 50 kV and 20 mA, was converted into a quasi-parallel beam by a single-reflection collimating X-ray mirror (XENOCs FOX2D CU 12\_INF; cf. chapter 6). The incident beam diameter was set to 0.8 mm by a circular pinhole collimator which, additionally, reduced the residual divergence of the beam as conditioned by the mirror (0.06°). The diffracted beam passed a parallel plate collimator (acceptance angle 0.23°) before being detected by an energy-dispersive detector (Bruker Sol-X).

XRD stress analysis at larger penetration depths was carried out at the synchrotron beamline B2 of HASYLAB, Hamburg, Germany, equipped with an Eulerian cradle. The beamline was used in direct, unmirrored beam configuration [48] (parallel-beam setup), the wavelength  $\lambda$  was adjusted to 0.8 Å ( $\mu_{\text{Fe}_4\text{N},0.8 \text{ \AA}} = 0.034 \text{ }\mu\text{m}^{-1}$ ; as calculated from data for Fe and N in Refs. [46,47]), and the incident beam size to 5 mm  $\times$  1 mm. The diffracted beam passed a Ge (111) analyzer crystal before being detected by a NaI scintillation counter.

During all measurements the specimen was rotated around its surface normal (about 2 rev./s) in order to attain better crystallite statistics. The rotational symmetry of the stress state was confirmed by additional stress measurements at different, constant, rotation angles  $\varphi$  around the specimen surface normal. The stress measurements were carried out in the combined  $\omega/\chi$  mode in order to keep the X-ray penetration depth  $\tau$  constant during the stress measurement [20,36]; due to the rotational symmetry of the stress state, only the angle  $\psi$  was controlled, whereas the angle  $\varphi$  varied.

The  $\gamma'$  220, 311 and 222 reflections were measured with a detector step size in  $2\theta$  varying between  $0.002^\circ$  and  $0.04^\circ$  depending on the instrument applied and on the  $hkl$  reflection investigated. A sufficient  $2\theta$  range was collected for each reflection in order to accurately describe peak tails and background. The diffraction-line positions were obtained by fitting Pearson-VII functions [49] to the measured data points. The  $\gamma'$  reflections were measured at constant penetration/information depths:  $\tau = 400$  nm, 700 nm and 1000 nm in the laboratory diffractometer and at  $\tau = 1000$  nm, 2000 nm, 3000 nm and 4000 nm at the synchrotron beamline. The coverable  $\psi$  range for XRSA at constant penetration depth varies with photon energy, diffraction angle and penetration depth [36]. For the measurements conducted in this work the width of the coverable  $\psi$  range varied between  $16^\circ$  and  $42^\circ$ . The absence of crystallographic texture could be verified by the analysis of reflection intensities as a function of  $\psi$ .

## 5.4. Results and discussion

### 5.4.1. Microstructure and phase analysis

A cross-sectional bright field optical micrograph of the specimen investigated is shown in Figure 5.1. The microstructure of the  $\gamma'$  layer consists of predominantly columnar grains with a considerable amount of twins. The average grain size in the direction of the surface normal and laterally is of the order of the layer thickness. Due to the substrate preparation procedure (cf. chapter 5.3.1) and because the layer grows inwardly the specimen surface is smooth, whereas the  $\gamma'/\alpha$  interface exhibits a considerable roughness.



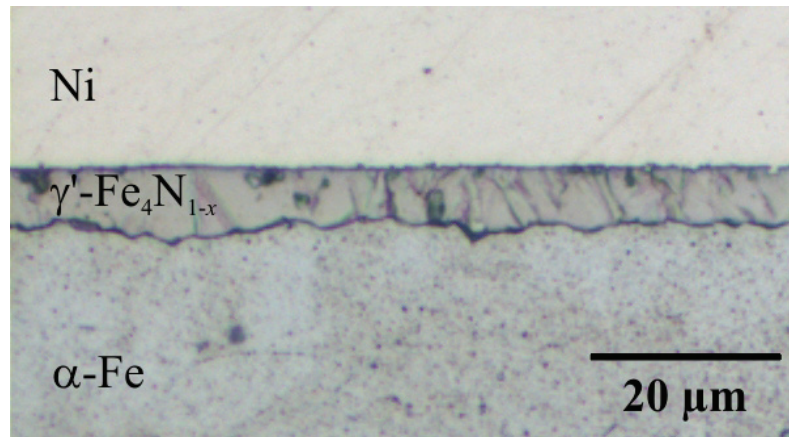


**Figure 5.1.** Optical micrograph of a cross section of the nitrided  $\alpha$ -Fe specimen.

Qualitative phase analysis of the nitrided specimen was performed by X-ray diffraction. The resulting diffraction pattern is shown in Figure 5.2. Evidently, the compound layer is composed exclusively of  $\gamma'$ -Fe<sub>4</sub>N<sub>1-x</sub>; as expected on the basis of the nitriding gas composition, pressure and temperature [6]. Due to the relatively low absorption of the X-ray radiation used (Co K $\alpha$  radiation was employed), additionally reflections from the  $\alpha$ -Fe substrate are visible.

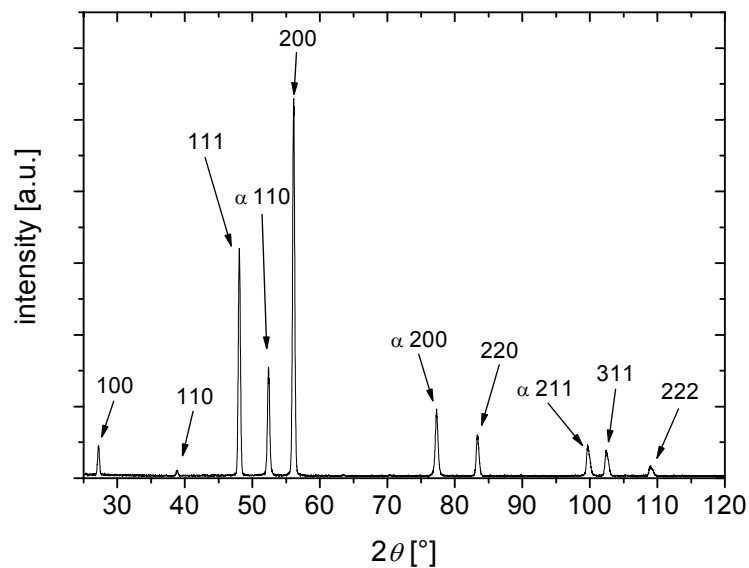


**Figure 5.2.** Diffraction pattern collected from the surface of the nitrided  $\alpha$ -Fe specimen employing the Philips MRD (Co K $\alpha$  radiation). Only reflections stemming from  $\gamma'$ -Fe<sub>4</sub>N<sub>1-x</sub> and  $\alpha$ -Fe (originating from the substrate; indicated by “ $\alpha$ ”) were detected.

### 5.4.2. Diffraction analysis at constant penetration depth

Due to the  $\psi$ -dependent asymmetry of the measured diffraction lines, which is indicative for the presence of a stress- and/or strain-free lattice-parameter gradient, the centroid has been employed for the determination of the diffraction-line position [50]. It is worth noting that the obtained  $\sin^2\psi$  plots (for an exemplary plot, see Figure 5.3) exhibit low scatter and no curvature, so that the measured data could be well fitted by a straight line (cf. equation (5.1)).

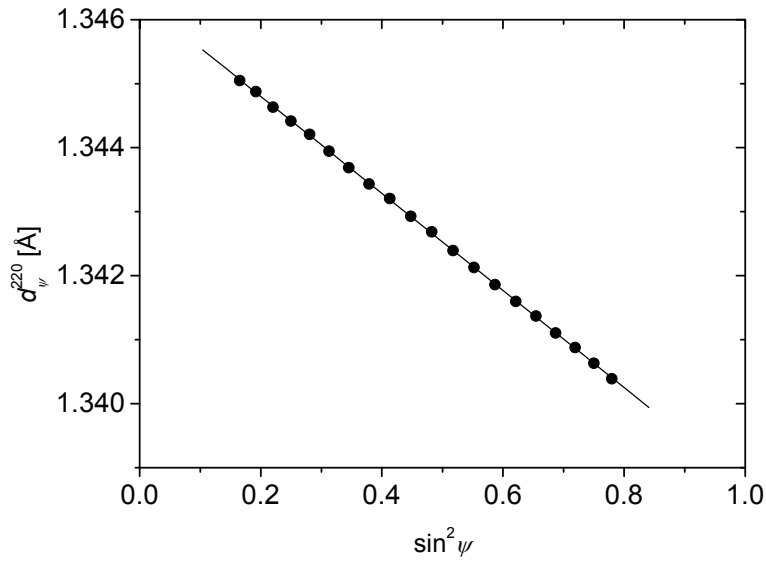


**Figure 5.3.** Measured  $\sin^2\psi$  plot; 220 lattice plane spacing  $d_{\psi}^{220}$  of  $\gamma'$ -Fe<sub>4</sub>N<sub>1-x</sub> versus  $\sin^2\psi$  at penetration depth  $\tau = 2000$  nm (Beamline B2, HASYLAB,  $\lambda = 0.8$  Å). The dots denote the measured data points and the straight line shows the linear fit to these data.

The linearity of the obtained  $\sin^2\psi$  plots on the one hand and the equiaxed nature of the specimen's microstructure (see Figure 5.1) both are consistent with an isotropic nature of the grain interaction (cf. begin of chapter 5.2.2).

The XECs of  $\gamma'$  employed in the calculation of lattice parameters (and thus of nitrogen concentration) and residual stresses (cf. chapters 5.4.2.1 and 5.4.2.2) have been listed in Table 5.1. These XECs have been adopted from a previous work, where single crystal elastic constants of  $\gamma'$  were determined by first-principles calculations and an effective grain interaction parameter  $w = 0.85$  (cf. chapter 5.2.2) was determined experimentally for the same specimen investigated in this work [11].

**Table 5.1.** XECs employed in this work for the determination of depth profiles of lattice parameter and residual stress [11].

$hkl$	$S_1^{hkl}$ [TPa <sup>-1</sup> ]	$1/2 S_2^{hkl}$ [TPa <sup>-1</sup> ]
220	-2.18	8.26
311	-2.11	8.05
222	-2.24	8.45

#### 5.4.2.1. Lattice-parameter and nitrogen-concentration depth profiles

The lattice-parameter depth profile follows from data obtained for the strain-free lattice spacing,  $d_0^{hkl}$ , as derived from the  $\sin^2\psi$  analysis at various constant penetration depths along the strain-free direction,  $\sin^2\psi_0$  (cf. equations (5.1) and (5.2)). Major instrumental aberrations in parallel-beam geometry as instrumental offsets in diffraction angle and photon energy (for the synchrotron measurements) were quantified by measuring a standard specimen. Thus, it was possible to correct the obtained diffraction-line positions for these offsets in the synchrotron measurements. The offset of the diffraction-angle scale in the laboratory diffractometer measurements was determined such that the lattice-parameter values determined in the laboratory and at the synchrotron *at the same information depth* coincide, as for the laboratory diffractometer a standard measurement was not available.

The thus determined strain-free lattice-parameter depth profiles in Laplace space, as derived from the strain-free directions of the 110, 311 and 111 lattice planes (220, 311 and 222 reflections), are shown in Figure 5.4.

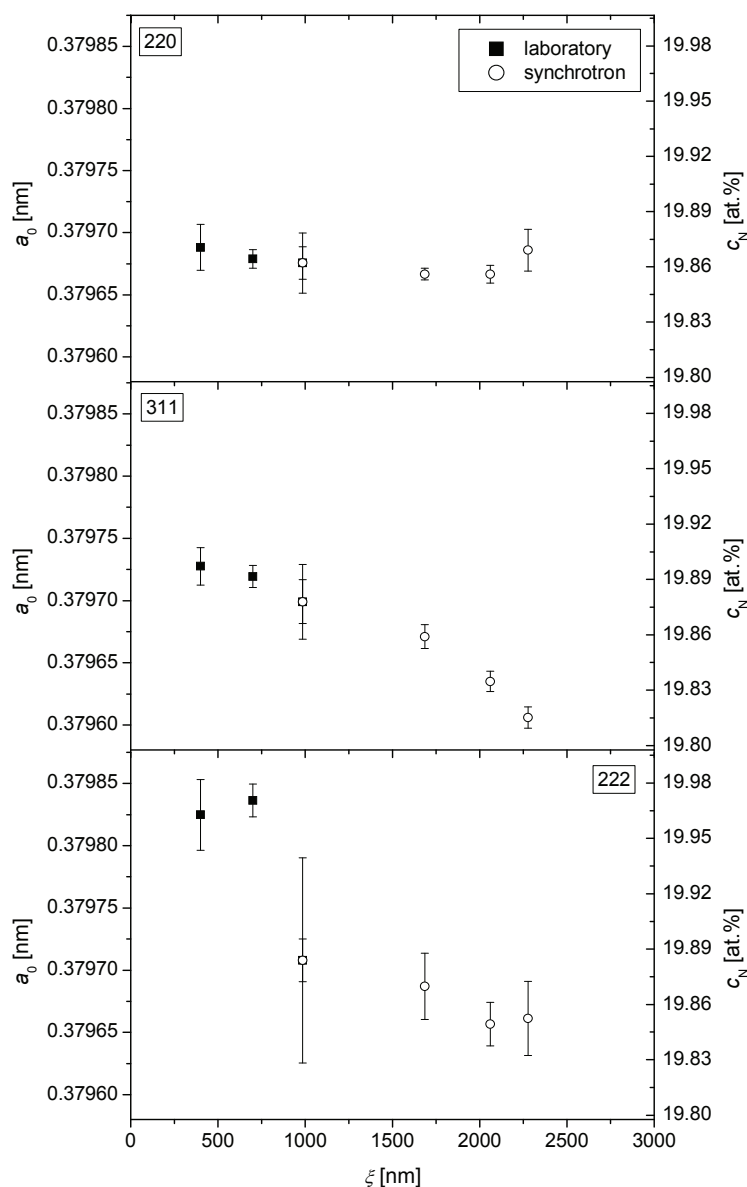


**Figure 5.4.** Strain-free lattice parameter,  $a_0$ , and nitrogen concentration,  $c_N$ , versus information depth as derived from lattice-parameter measurements along the strain-free direction of the 110, 311 and 111 lattice planes (220, 311 and 222 reflections) obtained in the laboratory (Bruker AXS D8, Cu  $K\alpha$  radiation) and at the synchrotron ( $\lambda = 0.8 \text{ \AA}$ ).

From thermodynamic data of the system Fe-N [6] it follows for the specimen-preparation conditions applied (cf. chapter 5.3.1) that the nitrogen concentration varies between 19.93 at.% at the surface ( $\gamma'$  in equilibrium with the gas atmosphere) and 19.58 at.% at the layer/substrate interface ( $\gamma'$  in equilibrium with  $\alpha$ -Fe). As a consequence of this concentration gradient also a (strain-free) lattice-parameter gradient exists. A relatively small change of nitrogen concentration,  $c_N$ , results in a

relatively large change of lattice parameter,  $a_0$ , for  $\gamma'$ -Fe<sub>4</sub>N<sub>1-x</sub>; see the relation given between  $a_0$  and  $c_N$  given in Ref. [51]. Because the layer grows by inward diffusion of nitrogen [14], a decreasing nitrogen concentration and thus lattice parameter with increasing information depth is expected. Such behavior is observed indeed for the data derived from the 311 and 222 reflections. However the gradient deduced from the 220 reflection is more or less zero. In order to explain this discrepancy the XECs used for the calculation of the strain-free directions for the three sets of lattice planes are considered detailed.

The XECs calculated according to the Voigt and Reuss models have been plotted in Figure 5.5 versus the orientation parameter for cubic materials [33],

$$\Gamma_{hkl} = \frac{h^2k^2 + h^2l^2 + k^2l^2}{(h^2 + k^2 + l^2)^2}. \quad (5.9)$$

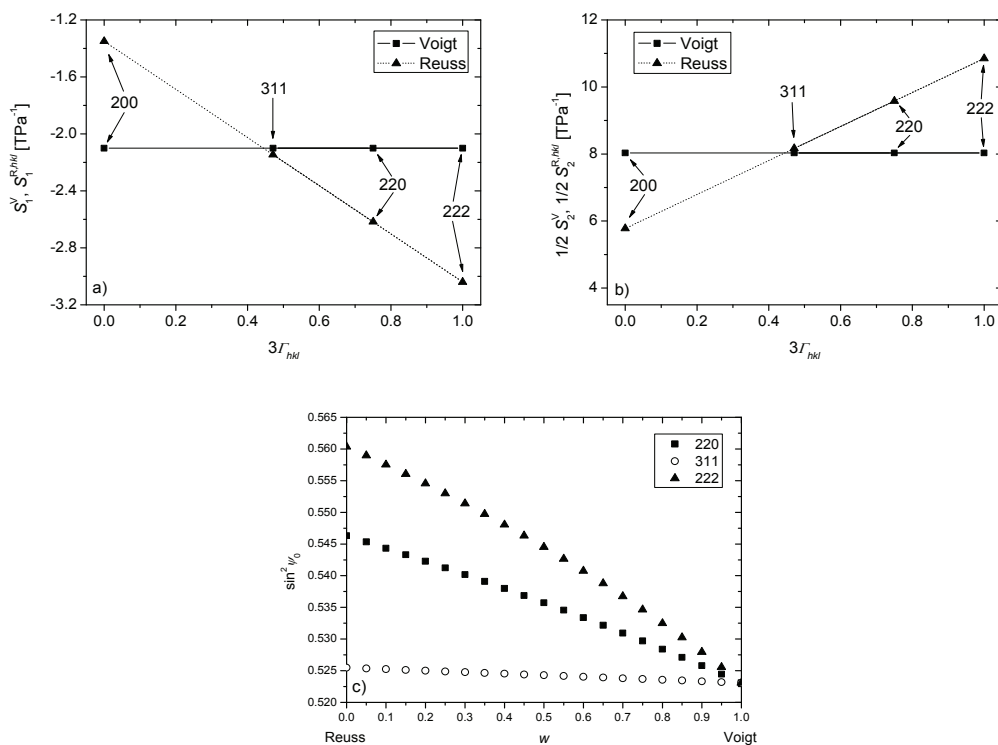


**Figure 5.5.** a) and b) Calculated values of the XECs,  $S_1^{hkl}$  and  $1/2 S_2^{hkl}$ , according to the Voigt and Reuss models versus  $3\Gamma_{hkl}$ . c) Strain-free direction versus grain-interaction parameter for the 220, 311 and 222 reflections.

It is evident from Figure 5.5 a and Figure 5.5 b that among all XECs those pertaining to the 311 planes remain nearly unchanged upon a variation in grain interaction between the two extremes given by the Voigt and Reuss models. Hence, among the investigated reflections, the strain-free direction as derived from the 311 reflection proves to be least sensitive to a variation of grain interaction (see Figure 5.5 c). Therefore, as the type of grain interaction can change with depth, the lattice-parameter gradient as derived from the 311 reflection is considered the most reliable one.

It also follows from the above that correct values for the strain-free directions,  $\sin^2 \psi_0$ , of the 110 and 111 lattice planes can be obtained by varying the XECs of the 220 and 222 reflections, i.e. by varying the grain-interaction parameter  $w$  (cf equation (5.3)), such that the strain-free lattice-parameter data determined from the 220 and 222 reflections fit the strain-free lattice-parameter value deduced from the 311 reflection. By performing this procedure for every penetration/information depth, the dependence of  $w$  on depth is revealed. The thus obtained strain-free directions and values of  $w$  are shown in Figure 5.6 for the synchrotron measurements.

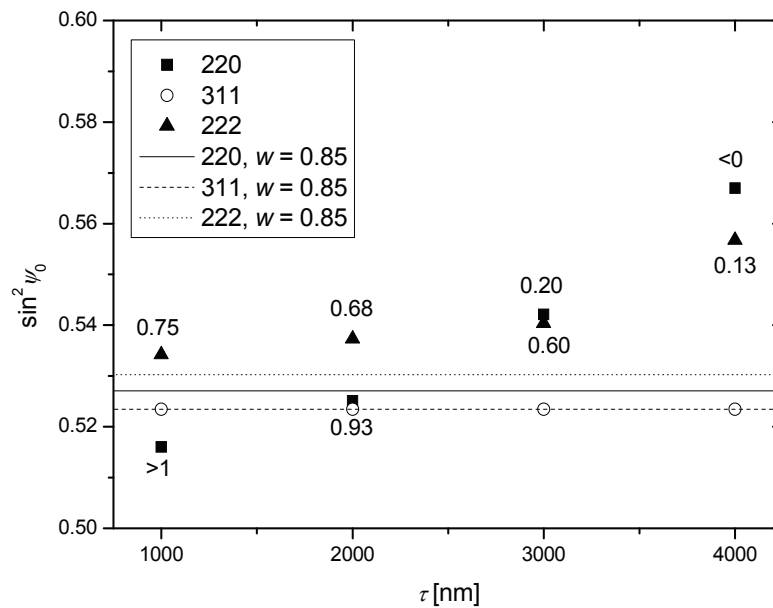


**Figure 5.6.** Strain-free directions obtained for coincidence of the measured lattice-parameter depth profiles, derived from the 220, 311 and 222 reflections as described in the text. The corresponding values for  $w$  for the 222 (near top) and 220 (near bottom) reflections are shown for each penetration depth. The solid, dashed and dotted lines indicate the strain-free directions corresponding to the 220, 311 and 222 reflections for  $w = 0.85$ , as initially used for the calculation of the XECs (see Table 5.1).

It follows that the type of grain interaction changes from Voigt- ( $w = 1$ ) to Reuss-type ( $w = 0$ ) with increasing depth. This may be understood as follows: The  $\gamma'$  layer has grown *into* the  $\alpha$ -Fe substrate and the interface between  $\gamma'$  and  $\alpha$  shows a considerable roughness (see chapter 5.4.1). Provided that the substrate is more compliant than the layer, it is suggested that the  $\gamma'$  crystallites can deform relatively independently from each other during the nitriding treatment. Due to the volume misfit between  $\gamma'$  and  $\alpha$  an equal in-plane stress (Reuss-type interaction) rather than an equal in-plane strain (Voigt-type interaction) is conceivable.

Finally, in order to extract the lattice-parameter depth profile in real space (Figure 5.7 (left)) from the one in Laplace space (Figure 5.7 (right)) the procedure described in chapter 5.2.3 has been adopted. For the reasons stated above, the lattice-parameter depth profile derived from the 311 planes has been selected for determination of the real-space lattice-parameter depth profile. The thus obtained real-space profile and the comparison of calculated and measured Laplace-space profile are provided by Figure 5.7.

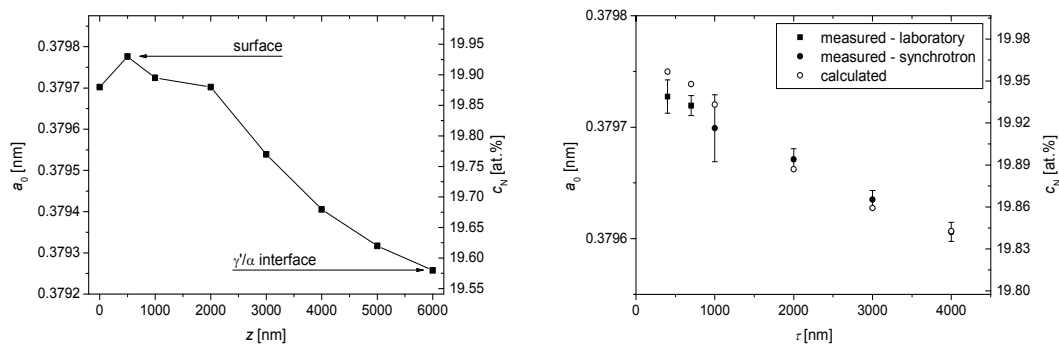


**Figure 5.7.** Real-space lattice-parameter and nitrogen-concentration depth profile (left) including indications for the thermodynamically calculated local equilibrium nitrogen concentrations at the surface and at the  $\gamma'/\alpha$  interface (arrows), and measured and calculated Laplace-space depth profiles (right) for the 311 reflection.

It follows that the Laplace-space profile calculated from the real-space profile fits well with the measured Laplace-space profile. Moreover, the nitrogen concentrations at the surface and at the  $\gamma'/\alpha$  interface as derived from the real-space lattice-parameter depth profile agree well with the thermodynamically calculated local equilibrium nitrogen concentrations (see arrows in Figure 5.7 (left)). The slight decrease in

nitrogen concentration in the surface-adjacent region is due to the formation of pores at the surface (cf. Ref. [16]).

#### 5.4.2.2. Residual stress depth profile

Here only the results derived from the 311 reflection will be discussed: it has been shown in chapter 5.4.2.1 that the data derived from the 220 and 222 reflections are unreliable because of incorrect values for the XECs used. The residual stress values as derived in  $\sin^2\psi$  evaluations (cf. equation (5.1)) of the 311 reflection has been plotted in Figure 5.8 (right) versus the penetration depth (i.e. *in Laplace space*). Applying a procedure analogous to the one used for the strain-free lattice-parameter depth profiles (chapters 5.4.2.1 and 5.2.3) the real-space residual stress depth profile has been derived from the Laplace-space residual stress depth profile. The result is shown in Figure 5.8.

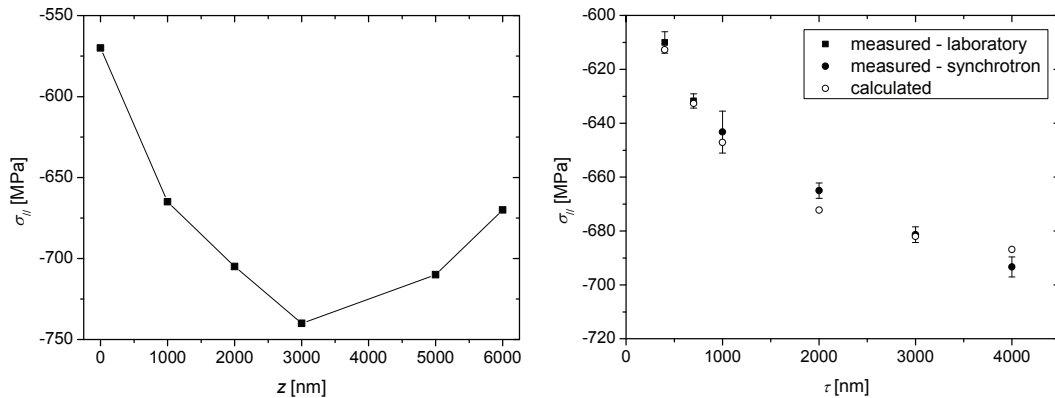


**Figure 5.8.** Real-space residual stress depth profile (left) and measured and calculated Laplace-space stress depth profiles (right); results derived from 311-reflection measurement.

Evidently a good agreement between measured and calculated Laplace-space stress-depth profiles has been achieved. The thus extracted real-space depth profile (Figure 5.8 (left)) shows an increase in absolute value of compressive stress with increasing depth due to stress relaxation near the surface; the layer exhibits a compressive stress maximum at half of the layer thickness; and finally decrease in compressive stress towards the  $\alpha/\gamma'$  interface is observed. This stress-depth behaviour can be discussed as follows.



The compressive nature of the residual stress in the  $\gamma'$  layer has two different origins [16]: (i) Thermal compressive stress, constant over the layer thickness, is built up in the layer during cooling from the nitriding temperature (823 K) to room temperature as a consequence of the difference of the coefficients of thermal expansion  $\alpha$  of layer ( $\alpha_{\gamma'-\text{Fe}_4\text{N}_{1-x}} = 7.62 \times 10^{-6} \text{ K}^{-1}$ ) [51] and substrate ( $\alpha_{\alpha-\text{Fe}} = 11.8 \times 10^{-6} \text{ K}^{-1}$  at 293 K,  $14.8 \times 10^{-6} \text{ K}^{-1}$  at 823 K) [52]. (ii) Compressive stress varying over the layer thickness due to elastic accommodation of the nitrogen concentration-depth profile. The magnitude of the compressive stress is expected to decrease with increasing depth as the nitrogen concentration (and thus the strain-free  $\gamma'$  lattice parameter) decreases with increasing depth (see Figure 5.7). Superimposed on this behaviour is a stress relaxation close to the specimen surface due to pore and (by coalescence of pores) channel formation along grain boundaries.<sup>b</sup> As a result, the magnitude of residual compressive stress *in real space* should first increase, then pass through a maximum and subsequently decrease with increasing depth.

## 5.5. Conclusions

- For the first time a *non-destructive* X-ray diffraction method to determine *simultaneously* both the composition depth profile and the residual stress depth profile, by measurements at constant penetration/information depths, has been applied successfully to a  $\gamma'$ -Fe<sub>4</sub>N<sub>1-x</sub> layer on top of an  $\alpha$ -Fe substrate.
- The 311 reflection has been used to determine the depth profiles of the strain-free lattice parameter (and thus the nitrogen concentration) and the residual stress, because this reflection has been shown to be insensitive to the type and variation of grain interaction. By tuning the strain-free direction of the 220 and 222 reflection such that they yield the same strain-free lattice parameter as the 311 reflection the depth dependence of the grain interaction has been determined.

---

<sup>b</sup> Such pore/channel formation is a consequence of the thermodynamic instability of  $\gamma'$  iron nitride with respect to the decomposition in Fe and N<sub>2</sub> gas (especially at grain boundaries) [16].

- The thus obtained nitrogen-concentration depth profile satisfies the thermodynamic, local equilibrium boundary conditions at the layer surface and at the  $\gamma'/\alpha$  interface.
- The residual stress depth profile as derived from the 311 reflection can be interpreted as the result of stress buildup by thermal misfit and the nitrogen concentration increasing with decreasing depth and stress relaxation in the surface-adjacent region due to pore/channel formation.

### **Acknowledgements**

The assistance of Dr T. Gressmann, Dr C. Baehtz and Mr D. Trots during the synchrotron measurements at DESY Hasylab beamline B2 is gratefully acknowledged.

## References

- [1] Knerr, C.H., Rose, T.C. & Filkowski, J.H. (1991). *Gas Nitriding*, in: *ASM Handbook*, edited by S. R. Lampman & T. B. Zorc, Vol. 4, pp. 387. ASM.
- [2] Jack, K.H. (1948). *Proc. R. Soc. London, A* **195**, 34.
- [3] Jacobs, H., Rechenbach, D. & Zachwieja, U. (1995). *J. Alloys Compd.* **227**, 10.
- [4] Kooi, B.J., Somers, M.A.J. & Mittemeijer, E.J. (1996). *Metall. Mater. Trans. A* **27A**, 1063.
- [5] Wriedt, H.A., Gokcen, N.A. & Nafziger, R.H. (1987). *Bull. Alloy Phase Diagr.* **8**, 355.
- [6] Mittemeijer, E.J. & Somers, M.A.J. (1997). *Surf. Eng.* **13**, 483.
- [7] Coey, J.M.D. & Smith, P.A.I. (1999). *J. Magn. Magn. Mater.* **200**, 405.
- [8] Borsa, D.M., Grachev, S., Boerma, D.O. & Kerssemakers, W.J. (2001). *Appl. Phys. Lett.* **79**, 994.
- [9] Costa-Krämer, J.L., Borsa, D.M., García-Martín, J.M., Martín-González, M.S., Boerma, D.O. & Briones, F. (2004). *Phys. Rev. B: Condens. Matter* **69**, 144402.
- [10] Bradley Easton, E., Buhrmester, Th. & Dahn, J.R. (2005). *Thin Solid Films* **493**, 60.
- [11] Gressmann, T., Wohlschlögel, M., Shang, S., Welzel, U., Leineweber, A., Mittemeijer, E.J. & Liu, Z.-K. (2007). *Acta Mater.* **55**, 5833.
- [12] Rozendaal, H.C.F., Mittemeijer, E.J., Colijn, P.F. & van der Schaaf, P.J. (1983). *Metall. Trans. A* **14A**, 395.
- [13] Somers, M.A.J. & Mittemeijer, E.J. (1995). *Metall. Mater. Trans. A* **26A**, 57.
- [14] Liapina, T., Leineweber, A. & Mittemeijer, E.J. (2006). *Metall. Mater. Trans. A* **37A**, 319.
- [15] Schaaf, P. (2002). *Prog. Mater. Sci.* **47**, 1.
- [16] Somers, M. A. J. & Mittemeijer, E. J. (1990). *Metall. Trans. A* **21A**, 189.
- [17] Somers, M.A.J. & Mittemeijer, E.J. (1990). *Metall. Trans. A* **21A**, 901.
- [18] Macherauch, E. & Müller, P. (1961). *Z. Angew. Physik* **13**, 305.
- [19] Welzel, U. & Mittemeijer, E.J. (2003). *J. Appl. Phys.* **93**, 9001.

- [20] Welzel, U., Ligot, J., Lamparter, P., Vermeulen, A.C. & Mittemeijer, E.J. (2005). *J. Appl. Cryst.* **38**, 1.
- [21] Voigt, W. (1910). *Lehrbuch der Kristallphysik*. Leipzig: Teubner.
- [22] Reuss, A. (1929). *Z. Angew. Math. Mech.* **9**, 49.
- [23] Neerfeld, H. (1942). *Mitt. K.-Wilh.-Inst. Eisenforschg.* **24**, 61.
- [24] Hill, R. (1952). *P. Phys. Soc. Lond. A* **65**, 349.
- [25] SAE (2003). *Residual Stress Measurement by X-Ray Diffraction*. Report HS-784. SAE. Warrendale, PA.
- [26] Azanza Ricardo, C.L., D'Incau, M. & Scardi, P. (2007). *J. Appl. Cryst.* **40**, 675.
- [27] Kämpfe, A., Eigenmann, B. & Löhe, D. (2000). *Z. Metallkd.* **91**, 967.
- [28] Behnken, H. & Hauk, V. (2001). *Mater. Sci. Eng. A* **300**, 41.
- [29] Predecki, P., Ballard, B. & Zhu, X. (1993). *Adv. X-Ray Anal.* **36**, 237.
- [30] van Acker, K., de Buyser, L., Celis, J.P. & van Houtte, P. (1994). *J. Appl. Cryst.* **27**, 56.
- [31] Genzel, Ch. (1997). *Phys. Status Solidi A* **159**, 283.
- [32] Genzel, C. (2005). *Mater. Sci. Technol.* **21**, 10.
- [33] Hauk, V. (1997). Editor. *Structural and Residual Stress Analysis by Nondestructive Methods*, Amsterdam: Elsevier.
- [34] Bein, S., Le Calvez, C. & Lebrun, J.-L. (1998). *Z. Metallkd.* **89**, 289.
- [35] Skrzypek, S.J., Baczmanski, A., Ratuszek, W. & Kusior, E. (2001). *J. Appl. Cryst.* **34**, 427.
- [36] Kumar, A., Welzel, U. & Mittemeijer, E. J. (2006). *J. Appl. Cryst.* **39**, 633.
- [37] Serruys, W., van Houtte, P. & Aernoudt, E. (1987). *X-ray measurement of residual stresses in textured materials with the aid of orientation distribution functions*, in: *Residual stresses in science and technology*, edited by E. Macherauch & V. Hauk, Oberursel: Deutsche Gesellschaft für Metallkunde.
- [38] Serruys, W., Langouche, F., van Houtte, P. & Aernoudt, E. (1989). *Calculation of X-ray elastic constants in isotropic and textured materials*, in: *Proceedings of ICRS 2*, edited by G. Beck, S. Denis & A. Simon, Vol. pp. 166. London: Elsevier Applied Science.
- [39] Welzel, U., Leoni, M. & Mittemeijer, E.J. (2004). *Diffraction elastic constants and stress factors; grain interaction and stress in macroscopically elastically anisotropic solids; the case of thin films*, in: *Diffraction Analysis of the*

- Microstructure of Materials*, edited by E. J. Mittemeijer & P. Scardi, p. 363. Berlin: Springer.
- [40] Kumar, A., Welzel, U. & Mittemeijer, E.J. (2006). *J. Appl. Phys.* **100**, 114904.
- [41] Leverenz, T., Eigenmann, B. & Macherauch, E. (1996). *Z. Metallkd.* **87**, 616.
- [42] Delhez, R., de Keijser, Th. H. & Mittemeijer, E. J. (1987). *Surf. Eng.* **3**, 331.
- [43] Colijn, P.F., Mittemeijer, E.J. & Rozendaal, H.C.F. (1983). *Z. Metallkd.* **74**, 620.
- [44] Wells, A. (1985). *J. Mater. Sci.* **20**, 2439.
- [45] Somers, M.A.J. & Mittemeijer, E.J. (1987). *Surf. Eng.* **3**, 123.
- [46] Creagh, D.C. (2004). *X-ray absorption spectra*, in: *International Tables for Crystallography*, edited by E. Prince, Vol. C, p. 213. Dordrecht: Kluwer.
- [47] Chantler, C.T., Olsen, K., Dragoset, R.A., Chang, J., Kishore, A.R., Kotochigova, S.A. & Zucker, D.S. (2005). *X-ray Form Factor, Attenuation, and Scattering Tables (version 2.1)*, <http://physics.nist.gov/ffast> (February 27th, 2008). National Institute of Standards and Technology, Gaithersburg, MD.
- [48] Knapp, M., Baetz, C., Ehrenberg, H. & Fuess, H. (2004). *J. Synchrotron Rad.* **11**, 328.
- [49] Sonneveld, E. J., Delhez, R., De Keijser, Th. H. & Mittemeijer, E. J. (1991). *Mater. Sci. Forum* **79-82**, 85.
- [50] Welzel, U., Lamparter, P., Leoni, M. & Mittemeijer, E.J. (2000). *Mater. Sci. Forum* **347-349**, 405.
- [51] Somers, M.A.J., van der Pers, N.M., Schalkoord, D. & Mittemeijer, E.J. (1989). *Metall. Trans. A* **20A**, 1533.
- [52] Touloukian, Y. S., Kirby, R. K., Taylor, R. E. & Desai, P. D. (1975). *Thermal Expansion, Metallic Elements and Alloys*. New York: IFI/Plenum.



## **6. Application of a single-reflection collimating multilayer optic for X-ray diffraction experiments employing parallel-beam geometry**

*M. Wohlschlägel, T.U. Schüllli, B. Lantz and U. Welzel*

### **Abstract**

Instrumental aberrations of a parallel-beam diffractometer equipped with a rotating anode X-ray source, a single-reflection collimating multilayer optic and a parallel-plate collimator in front of the detector have been investigated on the basis of standard measurements (i.e. employing stress and texture-free isotropic powder specimens exhibiting small or negligible structural diffraction line broadening). It has been shown, that a defocusing correction, which is a major instrumental aberration for diffraction patterns collected with divergent-beam (focusing) geometries, is unnecessary for this diffractometer.

The performance of the diffractometer equipped with the single-reflection collimating multilayer optic (a.k.a. single-reflection mirror) is compared with the performance of the diffractometer equipped with a Kirkpatrick-Baez optic (a.k.a. cross-coupled Göbel mirror) on the basis of experimental standard measurements and ray tracing calculations. The results indicate that the use of the single-reflection mirror provides a significant gain in photon flux and brilliance.

A high photon flux, brilliance and a minimal divergence of the incident beam make the setup based on the single-reflection mirror particularly suitable for grazing-incidence diffraction, and thus for the investigation of very thin films (yielding low diffracted intensities) and stress and texture (requiring the acquisition of large measured data sets, corresponding to the variation of the orientation of the diffraction vector with respect to the specimen frame of reference).

A comparative discussion of primary optics which can be used to realize parallel-beam geometry shows the range of possible applications of parallel-beam diffractometers and indicates virtues and disadvantages of the different optics.



## 6.1. Introduction

As the microstructure of materials is generally macroscopically anisotropic and/or inhomogeneous, its characterization by X-ray diffraction (XRD) analysis requires variation of the orientation of the diffraction vector with respect to the specimen frame of reference (see, for example, Ref. [1]). For this purpose diffractometers employing parallel-beam geometry are particularly suitable since they can provide invariant instrumental broadening, i.e. instrumental broadening which is independent of the orientation of the diffraction vector with respect to the specimen frame of reference; instrumental aberrations as defocusing occurring upon tilting the specimen in a diffractometer based on a focusing geometry are significantly reduced. Furthermore, parallel-beam diffractometers are insensitive to defocusing and peak shift occurring upon specimen misalignment with respect to the diffractometer axes, rough specimen surface or specimen transparency (see, for example, Refs. [2-4]). However, as the primary beam is not perfectly parallel but exhibits a small residual divergence ('quasi-parallel beam'), these aberrations are not generally totally removed [5].

There are two types of primary optics which can be used to realize a (quasi-)parallel-beam geometry in laboratory diffractometers: *Polycapillary optics* (also called '*X-ray lenses*'; see, for instance, Refs. [5-8]) and *multilayer optics* (also called '*X-ray mirrors*'; see, for instance, Refs. [9,10]).

An X-ray lens consists of millions of hollow glass fibres. The X-rays produced by the source are guided through these capillaries by multiple total reflections at their inner walls. Typical diameters of beams emerging from commercially available *collimating* lenses range from 5 mm to 10 mm. Depending on the length and diameter of the capillaries and on the critical angle for total reflection a (quasi-) parallel beam with a divergence of approximately  $0.3^\circ$  can be created (for Cu  $K\alpha$  radiation). Note that the beam divergence is a function of the energy of the radiation: For lower energies the divergence becomes larger, for larger energies the divergence becomes smaller (see, for example, Ref. [11]). The actual size of the incident beam is commonly adjusted by slits or pinholes at the lens exit (see, for example, Refs. [12,13]).

X-ray multilayer optics with parabolic shape and a thickness gradient in one plane (one-dimensional mirrors) have been introduced in the 1990's as a tool to

collimate a divergent X-ray beam by Bragg diffraction in this plane [9]. To achieve horizontal and vertical collimation of the X-ray beam, as it is particularly desired in X-ray diffraction analyses operated in point focus configuration, up to now a serial arrangement (called Kirckpatrick-Baez (K-B) optic [14]) or a side-by-side arrangement (called Montel optic [15]) consisting of two mirrors oriented perpendicular to each other had to be employed and thus the X-rays had to be reflected twice. The single-reflection collimating multilayer optic employed in this work is of parabolic shape with respect to two mutually perpendicular planes (i.e. paraboloidal) and thus can collimate the X-ray beam both horizontally and vertically using only a single instead of two subsequent Bragg reflections. This feature yields a significant gain in primary beam flux compared to the K-B optic due to two advantages: Firstly, in a K-B optic the mirror further away from the source has, particularly for a small source, a much lower collection angle (i.e. the solid angle of the beam created in the source which is seen by the mirror) than the mirror closer to the source [10]. This leads to a reduction in photon flux after passage of the K-B optic as compared to a single-reflection optic. Secondly, utilizing only one reflection instead of two reflections to collimate X-rays both horizontally and vertically leads to a reduction of the flux loss generally caused by imperfections of the mirror.

## **6.2. Background**

The first part of this chapter contains all geometry conventions used in this work including definitions of the frames of reference and all instrumental and measurement angles. In the second part instrumental aberrations occurring in parallel beam geometry are discussed. The third part of this chapter is dedicated to the functional principle of the single-reflection collimating X-ray mirror employed in this work.

### **6.2.1. Geometry conventions**

#### **6.2.1.1. Frames of reference**

For the diffraction analysis of the microstructure of materials it is necessary to define the following Cartesian frames of reference.

*The specimen reference frame (S):* The  $S_3$  axis is oriented perpendicular to the specimen surface and the  $S_1$  and  $S_2$  axes lie in the surface plane.

*The laboratory reference frame (L):* The  $L_3$  axis is chosen such that it coincides with the diffraction vector. The direction of the diffraction vector with respect to the specimen surface normal ( $S_3$  axis) is characterized by the angles  $\varphi$  and  $\psi - \varphi$  describing the rotation of the diffraction vector around the specimen surface normal and  $\psi$  describing the inclination of the diffraction vector with respect to the specimen surface normal. For  $\varphi = \psi = 0$ , the laboratory frame of reference coincides with the specimen frame of reference.

### 6.2.1.2. Diffraction geometry

In order to investigate by X-ray diffraction a set of crystal lattice planes with a certain orientation within the specimen, it is necessary to bring these planes into diffraction condition by aligning the lattice plane normal with the diffraction vector ( $L_3$  axis of the laboratory system L). In a diffractometer this can be achieved by appropriate adjustment of instrumental angles. These instrumental angles should be distinguished from the angles  $\varphi$  and  $\psi$  which describe the orientation of the diffraction vector with respect to the specimen system S (see chapter 6.2.1.1). The instrumental angles are defined as follows (see also Ref. [16]).

$2\theta$ : Diffraction angle. This angle is set by the detector position. In the following the angle  $\theta$  is strictly used as half of the diffraction angle (Bragg angle, i.e. the angle between the incident and diffracted beams, respectively, and the diffracting crystal lattice planes).

$\omega$ : Angle of rotation of the specimen around an axis perpendicular to the diffraction plane and parallel to the  $2\theta$  axis. For symmetric diffraction condition it holds:  $\omega = \theta$ .

$\chi$ : Angle of rotation of the specimen around an axis defined by the intersection of the diffraction plane and the specimen surface. This axis is perpendicular to the  $\omega$  and  $2\theta$  axes.

$\phi$ : Angle of rotation around the normal of the plate of the sample stage. Usually the sample is mounted on the stage such that the  $\phi$  and  $\varphi$  axes coincide and both axes are then simply related by a constant rotational offset.

In order to select a certain set of crystal lattice planes with the orientation  $(\varphi, \psi)$  with respect to the specimen system S for a diffraction measurement one has to set the desired combination  $(\varphi, \psi)$  by appropriate adjustment of the instrumental angles  $\omega$ ,  $\chi$  and  $\phi$ . The angle  $\varphi$  can simply be set by adjusting  $\phi$  taking into account the constant rotational offset (see above). The selection of the angle  $\psi$  is generally accomplished in three different ways: by setting  $\chi = 0$  and adjusting  $\omega$  ( $\omega$  mode; also called iso-inclination method), by setting  $\omega = \theta$  and adjusting  $\chi$  ( $\chi$  mode; also known as side-inclination method) or by combinational setting of  $\omega$  and  $\chi$  (combined  $\omega/\chi$  mode). For details about the described modes and their benefits and drawbacks the reader is referred to Ref. [16] and references therein (see also Ref. [17]).

### 6.2.2. Instrumental aberrations in parallel-beam X-ray diffraction

In the following subsections the instrumental aberrations involved in experiments using parallel beam X-ray powder diffraction are described, as they play an important role in the characterization of collimating primary optics. Theoretical treatments of these aberrations can also be found in other literature about instrumental aspects involving parallel-beam geometry (see, for example, Refs. [12,13,18,19]). Additional instrumental aberrations occurring only in focusing geometries (as the Bragg-Brentano or Seeman-Bohlin geometries) are not considered in this work (for details see Ref. [20]).

#### 6.2.2.1. Illuminated and detected areas

The following treatment is only valid for polycrystalline specimens (for more details, see, for example, Ref. [21]). When the diffractometer is operated in  $\chi$  mode, the area on the specimen illuminated by the X-ray beam is a function of the angles  $\theta$  and  $\psi$  ( $= \chi$ ) and is given by

$$G = \frac{G_0}{\sin \theta \cos \psi}, \quad (6.1)$$

where  $G_0$  is the cross section of the incident beam. To correct for variation of the illuminated area, the measured intensity has to be divided by  $G$ . Note that, for an infinitely thick specimen (i.e. a specimen which has a thickness much larger than the

penetration depth  $\tau$ , see, for example Ref. [22] for a definition of  $\tau$ ), as long as the illuminated area does neither comprise areas outside the specimen nor does the diffracted beam hit areas outside the detector, an intensity increase due to a larger illuminated area on the specimen upon tilting is compensated by an intensity decrease due to absorption (see, for example, Ref. [12]). However, if areas outside the specimen are illuminated or if a part of the diffracted beam is not registered by the detector, equation (6.1) is not longer valid and additional corrections for these aberrations, which will be referred to as instrumental intensity loss hereafter, are necessary. These corrections have been discussed in detail for parallel-beam geometry realized by an X-ray lens elsewhere [12].

#### **6.2.2.2. Defocusing**

Because in parallel-beam geometry a focusing condition does not exist, the instrumental aberration of defocusing strictly speaking cannot occur. Therefore, the shape of a measured diffraction line in parallel-beam geometry should be independent of specimen tilt and rotation. However, as in reality the collimated primary beam exhibits a small residual divergence (quasi-parallel beam; see chapter 6.5.1) and the diffracted beam optics also accept a small residual divergence (acceptance angle; see chapter 6.4) the defocusing phenomenon requires special attention. For a parallel-beam geometry realized by an X-ray lens this kind of (also experimental) consideration has already been performed [12,13].

#### **6.2.3. Functional principle of a single-reflection collimating X-ray mirror**

Multilayer mirrors are applied as X-ray optics due to their high efficiency. Furthermore, as compared to monochromator crystals, their layer periodicity can be arbitrarily chosen and even their density profile can be tuned according to the reflective and dispersive requirements. The possibility to grow graded multilayers opened the way to produce such optics on large curved surfaces [9]. The curvature, ellipsoidal or parabolic, determines whether the mirror is focusing or collimating the beam. In its simplest form, such a multilayer mirror is deposited on a Si-wafer bent into one dimension. It is thus a reflective optic that is uniquely shaping the beam in the diffraction plane.

### 6.2.3.1. Two dimensional beam shaping by mirror optics

The first graded multilayer mirrors were used for line-focus geometries, typically in X-ray reflectometry and coplanar diffraction. For point-focus geometries, double focusing or collimation is required and thus systems that imply two reflections are generally used. One possibility is the Kirkpatrick-Baez geometry, where two crossed one-dimensional mirrors are simply mounted in a serial way [14]. The other possibility is a Montel geometry, where the mirrors are mounted side-by-side [15]. The main advantage of the latter is that both mirrors are identical, as their distance to the source and the sample is the same for both. New technologies of polishing and shaping substrates offer nowadays the possibility to produce graded multilayer mirrors that obtain two-dimensional effects with one single reflection. This obviously leads to a significant increase in flux compared to a serial arrangement of two one-dimensional mirrors, due to the flux loss caused by imperfections of X-ray optics. A further increase of the photon flux can be obtained via a larger collection angle or a better source size acceptance obtained in the single-reflection geometry.

The shape of a multilayer mirror is adapted to the requirements it is made for. It can be either ellipsoidal for focusing, or parabolic for collimation, as obtained either by bending or by polishing. The multilayer gradient has to be adapted accordingly in order to match the Bragg reflection condition on every position on the mirror. The sketch in Figure 6.1 shows the (enlarged) gradient that adapts the Bragg condition to the mirror shape and hence the change in angle of incidence.

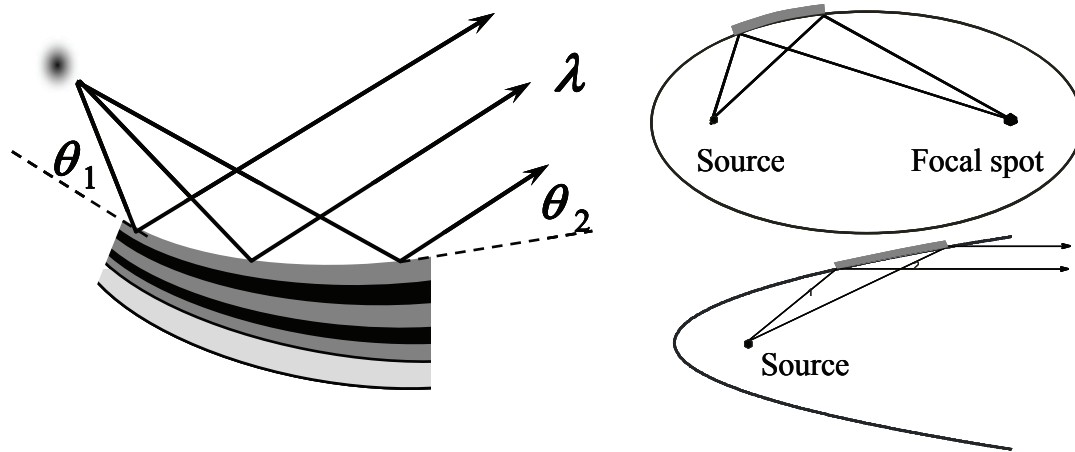


**Figure 6.1.** Left: Sketch of a graded parabolic multilayer mirror for beam collimation.  $\theta_1$  and  $\theta_2$  are Bragg angles at different spots on the mirror for radiation with wavelength  $\lambda$ . Upper right: for focusing geometries, the mirror is of ellipsoidal shape; source and focal point lay in the foci of the corresponding ellipsoid. Lower right: the equivalent situation for a parabolic, collimating mirror.

With simple geometrical considerations it becomes clear that all definitions for the multilayer shape are defined for a point source. Any spatial extension will either be rejected by the mirror or will produce “imperfections” in the reflected signal. These are a magnification of the focal spot for focusing geometries or a corresponding intrinsic divergence of the collimated beam. The source size acceptance of the mirror is directly linked to the local angular acceptance of the incident beam, i.e. to the rocking curve width  $\Delta\alpha$  of the multilayer Bragg peak (see, for example, Ref. [10]).

### 6.2.3.2. Single-reflection mirrors

Single-reflection mirrors obtain point focusing or two-dimensional collimation from point sources by one single reflection. This is obtained by a doubly curved mirror surface with a gradient in one dimension as sketched in Figure 6.1. The focusing or collimation in the scattering plane is thus completely equivalent to one dimensional mirrors. Purely the shape of the substrate determines the saggital focusing in the direction perpendicular to the scattering plane and thus no two-dimensional gradient is necessary (see Figure 6.2).

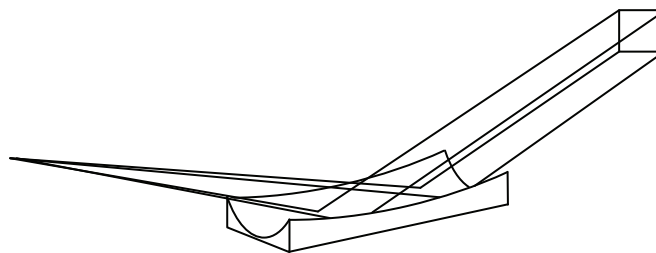


**Figure 6.2.** Schematic of single-reflection mirror. X-rays are emerging from a point source (left).

As an important consequence, the source size acceptance is only in one dimension limited by the rocking curve width. In the saggital direction the source size tolerance can be bigger and thus allows for a higher photon flux. The main advantages of a single-reflection geometry, besides gain in flux, are the possibility of high collection angles and source size acceptance, significantly easier mirror alignment and compact optic design as compared to double reflection geometries. The collimating FOX2D single-reflection mirror regarded here, has a source size acceptance of 0.1 mm at a focal length of 120 mm from the source. In the setup considered in this article, the effective source size in point focus geometry was  $0.1 \times 0.1 \text{ mm}^2$  and thus the resulting collimated beam was expected to have symmetrical beam conditions at the mirror exit.

### 6.3. Ray-tracing simulations

For modelling beam divergence, shape and intensity distribution of the primary beam as conditioned by the single-reflection mirror analytically (see also chapters 6.5.1 and 6.5.2), ray-tracing simulations have been performed employing the commercially available software ZEMAX-EE (ZEMAX Development Corporation). For comparison, the same simulations have also been performed for a K-B optic composed of the same multilayer materials as the single-reflection mirror. A two-dimensional, monochromatic ( $\text{Cu K}\alpha$  ( $E = 8.041 \text{ keV}$ )) Gaussian source with a size of  $100 \mu\text{m} \times 100 \mu\text{m}$  (full width at half maximum intensity) radiating in a cone angle of  $1.2^\circ$  has been assumed. The simulations have been conducted considering two cases: (i) primary beam as conditioned by the optics without pinhole collimator and (ii) primary beam as conditioned by the optics and a pinhole collimator in front. In Table



6.1 geometric measures necessary for the ray-tracing simulations are listed for both primary optics.

**Table 6.1.** Geometric measures of the primary optics used in the ray-tracing simulations.

geometric measure	FOX 2D	K-B optic
focal length [mm]	120	84 <sup>c</sup> /154 <sup>d</sup>
mirror length [mm]	60	40 <sup>1</sup> /60 <sup>2</sup>
incidence angle at mirror centre [°]	1.3	
distance source – pinhole [mm]	367	
pinhole diameter [mm]	0.8	

The mirror reflectivity has been taken into account adopting the source size and the shape of the mirror's Bragg peak, which varies with the gradient of the multilayer thickness. The obtained mean reflectivity (averaged over the whole illuminated mirror surface) is 42 % for the single-reflection collimating mirror.<sup>e</sup> For the K-B optic the reflectivity of the first mirror (closer to the source) has been obtained as 34 % – that of the second mirror as 49 %; as this mirror is situated farther away from the source it collects a larger part of the beam at high reflectivity. Thus, the mean reflectivity of the K-B optic is 17 % ( $0.34 \times 0.49 \approx 0.17$ ).

In Figure 6.3 and Figure 6.4 images of the beam profile as conditioned by the single-reflection mirror and the K-B optic at the mirror exit resulting from ray-tracing simulations of case (i) (see above) are shown. The sagittal direction is plotted horizontally; the tangential direction is plotted vertically. The image size is  $3 \times 3 \text{ mm}^2$  and the mesh used is  $100 \times 100$  pixels. The numbers pertaining to the colour code

<sup>c</sup> first mirror, closer to the source

<sup>d</sup> second mirror, farther away from the source

<sup>e</sup> The geometry of the single reflection mirror, which is 60 mm long and has its centre at a distance of 120 mm from the source, leads to a significant variation of the incident beam divergence along the mirror. As the source size of 0.1 mm is responsible for this divergence, it thus amounts to 0.1/90 radians  $\sim 0.064^\circ$  at the mirror entrance and to 0.1/150 radians  $\sim 0.038^\circ$  at the mirror exit. Having a finite angular acceptance, the mirror reflectivity varies with the incident divergence. For a double bent mirror, this incident divergence only has an effect in the reflection plane, where the Bragg condition is responsible for the angular acceptance. In the sagittal direction this acceptance limit does not apply. Thus, there is a linear increase of the reflectivity as a function of distance from the source. The radiation density decreases with the square of the distance, and thus still leads to reduction of the reflected intensity for the parts of the mirror that are further away from the source. In a numerical simulation, all parameters mentioned above have to be collected for every point on the mirror in order to calculate the mean reflectivity.

indicate the fraction of reflected rays at a point of the beam cross section. The term ‘efficiency’ given in the figure captions denotes the percentage of rays reflected by the optical system inside the source cone angle (see above).

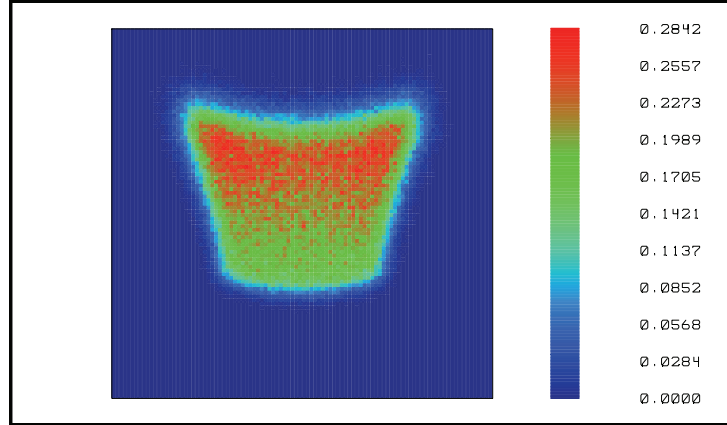


**Figure 6.3.** Calculated beam profile as conditioned by the single-reflection mirror; case (i). The efficiency is 44.8 %.

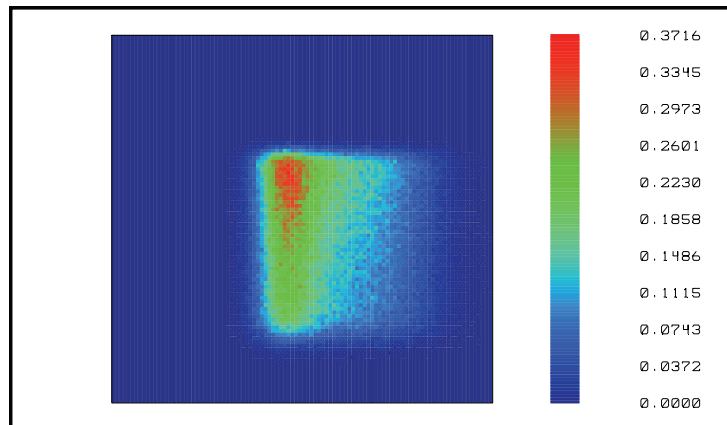


**Figure 6.4.** Calculated beam profile as conditioned by the K-B optic, case (i). The efficiency is 30.4 %.

The collection angle of the single-reflection mirror is 1.5 times larger than the one of the K-B optic. For a single-reflection mirror and a K-B optic composed of the same multilayer materials the geometrical gain in photon flux follows from the ratio of collection angle multiplied by the ratio of reflectivity. In case (i) one obtains

$$1.5 \times \frac{0.42}{0.17} = 3.7 \quad (6.2)$$

in favour of the single-reflection mirror.

The mean beam divergence resulting from the single-reflection mirror is visualized in Figure 6.5.

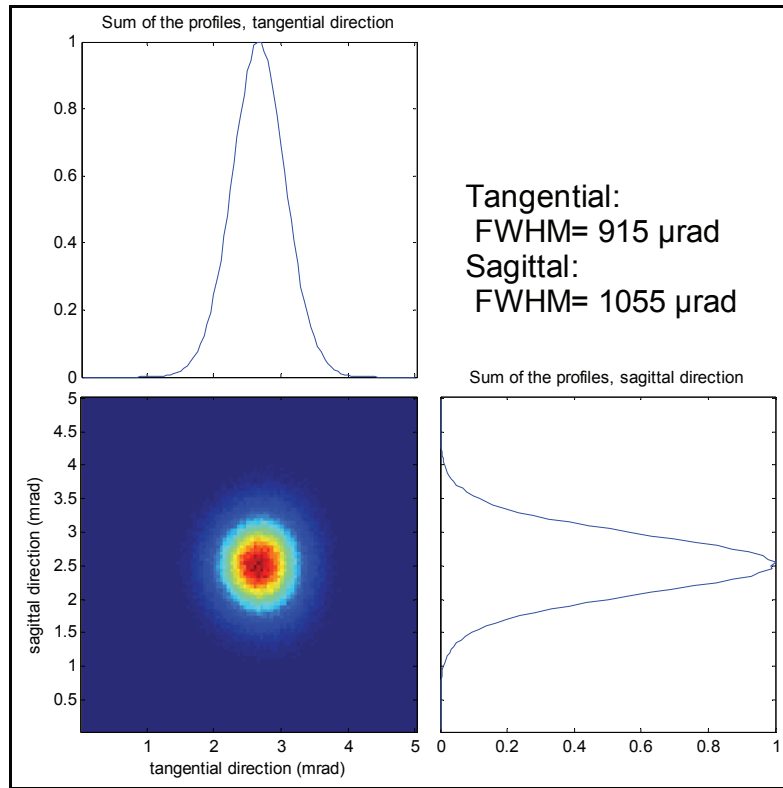


**Figure 6.5.** Mean beam divergence resulting from the single-reflection mirror, case (i).

In Figure 6.6 and Figure 6.7 the calculated beam profiles for case ii) (see above) at a distance of 300 mm away from the pinhole are shown. For a description of picture details see the description of Figure 6.3 and Figure 6.4.

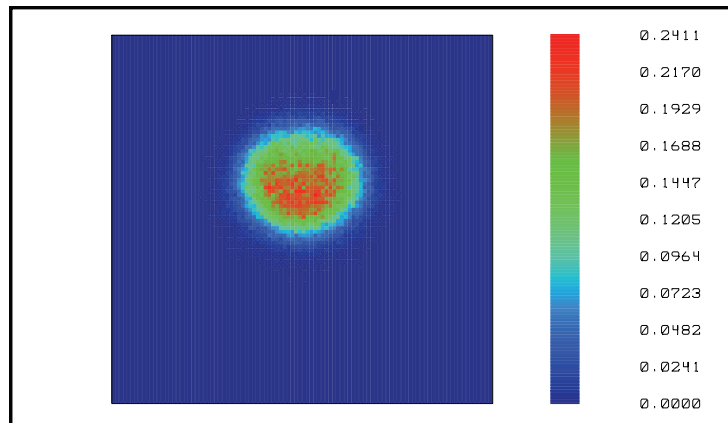


**Figure 6.6.** Calculated beam profile as conditioned by the single-reflection mirror; case (ii). The efficiency is 11.1 %.

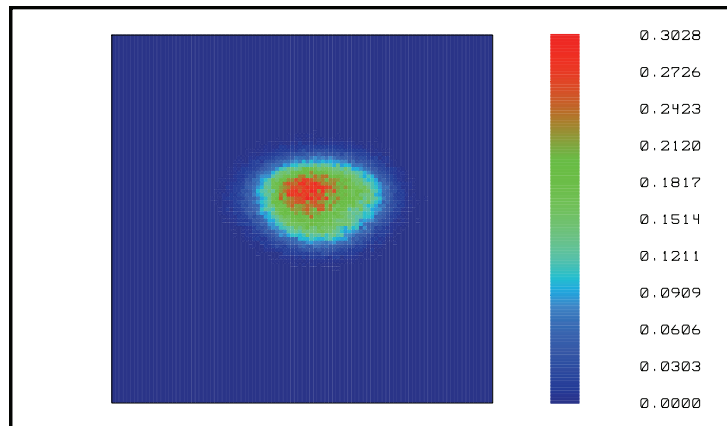


**Figure 6.7.** Calculated beam profile as conditioned by the K-B optic, case (ii). The efficiency is 10.4 %.

Geometrically, the number of rays passing through the pinhole collimator is only 5 % larger for the single-reflection mirror than for the K-B optic. Thus, analogous to equation (6.2), the geometrical gain in photon flux in case (ii) amounts to

$$1.05 \times \frac{0.42}{0.17} = 2.6 \quad (6.3)$$

in favour of the single-reflection mirror.

## 6.4. Experimental

A Bruker AXS D8 Discover X-ray diffractometer equipped with an Eulerian cradle (four-circle goniometer) has been used. Cu K $\alpha$  radiation emerging from the focus (0.1 mm  $\times$  1 mm) of a rotating anode source (Bruker AXS Turbo X-ray source) operating at 50 kV and 20 mA has been converted into a quasi parallel beam by a single-reflection collimating X-ray mirror (XENOCs FOX2D CU 12\_INF). As the mirror has been mounted under a takeoff angle of 6° the beam cross section seen by the optic is 0.1 mm  $\times$  0.1 mm. The size of the beam at the mirror exit was approximately 1 mm  $\times$  1 mm. For a comparison of the intensity in the diffracted signal applying different primary optics, also a K-B optic (Bruker AXS) has been mounted as collimating primary optic under the same takeoff angle. The size of the beam conditioned by the K-B optic was slightly smaller than the size of the beam conditioned by the single-reflection mirror (see also chapter 6.3). The divergence of the primary beam as conditioned by the K-B optic is given by the manufacturer as 0.05° for Cu K $\alpha$  radiation. The diffracted beam passed a parallel-plate collimator (acceptance angle 0.23°) before being detected by a scintillation counter.

To measure the residual divergence of the (quasi-)parallel beam a <100> cut single crystal silicon wafer (area 14 mm  $\times$  20 mm, thickness 0.5 mm) has been used. The measurements of the intensity in the diffracted beam have been done employing an alumina intensity standard (NIST SRM 1976; area 45 mm  $\times$  44 mm, thickness 1.7 mm). A powder specimen obtained by filling a square cavity cut in an aluminium disk with tungsten powder (from Merck, area 14 mm  $\times$  14 mm) has been used to investigate the instrumental effects in XRD stress and texture analysis employing parallel-beam geometry.

Diffraction patterns have been evaluated by fitting split Pearson VII functions (for a definition of the profile function, see Ref. [23]). Peak positions, peak heights, half-widths at half maximum (HWHM) values and shape parameters have been refined. The K $\alpha_2$  component has been taken into account by fitting two profile functions, one for each radiation component. A K $\alpha_2$  to K $\alpha_1$  intensity ratio of 0.5 has been assumed. For each diffraction peak a linear background has been fitted. The measurement ranges have been chosen such as to cover an adequate amount of points for a complete description of peak tails and background.

Images of the primary beam have been collected employing a marcam CCD-camera for X-ray alignment. The camera has been placed in the primary beam path at a distance of approximately 6 cm away from the mirror exit.

The photon flux has been measured with a Forvis XPD100 X-ray pin diode detector system placed on the sample stage in the path of the primary beam.

## 6.5. Experimental results and discussion

### 6.5.1. Beam divergence and beam shape

The residual divergence of the beam conditioned by the single-reflection mirror has been measured employing a  $\langle 100 \rangle$  cut single crystal silicon wafer as standard specimen. A rocking curve of the Si (400) reflection has been recorded without any optical components except a Cu attenuator foil in the path of the diffracted beam (see Figure 6.8). The difference between the full width at half-maximum (FWHM) of the measured rocking curve and the intrinsic line width of the radiation used can be taken as an estimate for the residual divergence of the incident beam. The diffraction line width due to mosaicity of the employed silicon wafer is one order of magnitude smaller and thus has not been taken into account. The FWHM of the  $\alpha_1$  component of the recorded peak has been determined as  $0.072^\circ$  by fitting a double Lorentzian Peak to the measured data points. The intrinsic line width of the Cu  $K\alpha_1$  line at the considered angle has been taken from literature as  $0.012^\circ$  [24]. Due to the fact that the  $\alpha_1$  component of the measured peak can be reasonably well approximated by a Lorentz function and the intrinsic shape of the Cu  $K\alpha_1$  line is Lorentzian [24], the FWHM's can be subtracted linearly from each other. Thus, the residual divergence of the incident beam has been determined as  $0.060^\circ$  or 1 mrad.

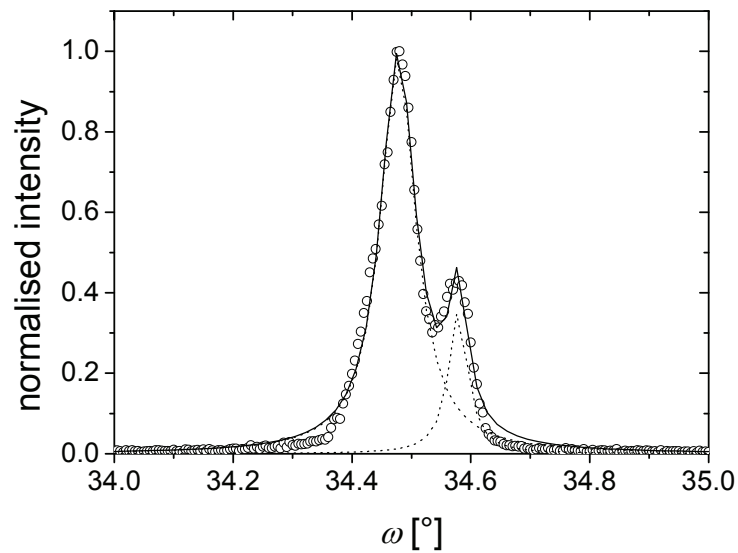


**Figure 6.8.** Rocking curve of the Si 400 reflection without any optical components except a Cu attenuator in the diffracted beam path; measured data points (circles), fitted double-Lorentzian peak (line) and individual Lorentzian peaks for the  $\alpha_1$  and the  $\alpha_2$  component (dotted line).

The measured divergence of the incident beam lies only slightly above the value of 0.8 mrad given by the manufacturer.

The beam shape has been recorded with a marcam CCD X-ray camera. The resulting beam shape is shown in Figure 6.9.

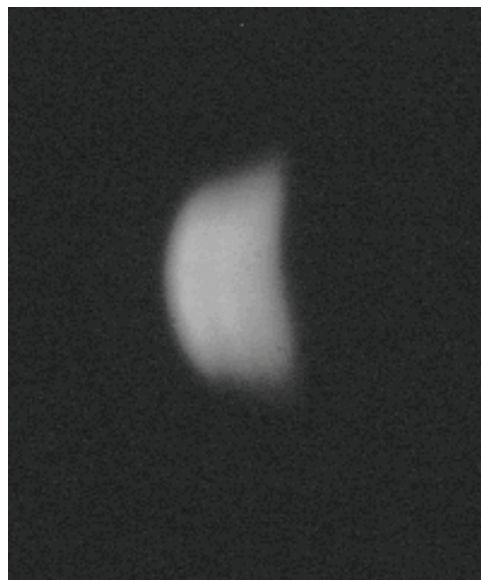


**Figure 6.9.** Beam shape as recorded with the marcam X-ray camera.

It follows that the primary beam produced by the single-reflection mirror has a curved rectangular shape with a height to width ratio of approximately 1.7 : 1. Its cross section is about 1.2 mm x 0.7 mm. The intensity of the beam is slightly reduced at its edges.

### 6.5.2. Primary beam intensity and brilliance

To compare the intensity obtained employing either the single-reflection mirror or the previously mounted K-B optic diffraction lines were collected from an alumina intensity standard employing both primary optics. The diffraction patterns obtained for the  $\text{Al}_2\text{O}_3$  012 and 226 reflections have been presented in Figure 6.10.



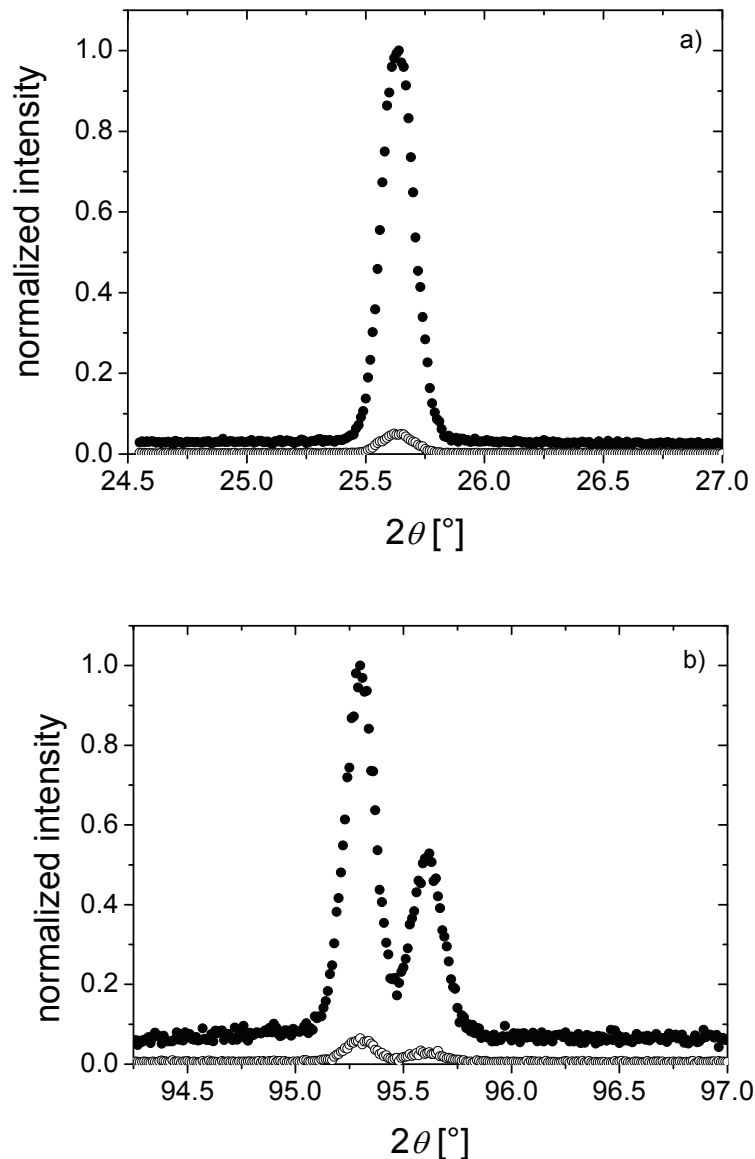


**Figure 6.10.** Intensity in the diffracted signal from the  $\text{Al}_2\text{O}_3$  012 (a) and 226 (b) reflections obtained with the Kirkpatrick-Baez optic (open circles) and with the single-reflection mirror (filled circles).

The measured diffraction lines show that there is a large gain in peak intensity of a factor of 14 to 20 by using the single-reflection mirror as compared to the K-B optic. Figure 6.11 shows the integrated intensity determined by peak fitting obtained with the single-reflection mirror and the K-B optic for four measured  $\text{Al}_2\text{O}_3$  diffraction lines and confirms the intensity gain. Differences in the gain factors in integrated intensity obtained from different diffraction lines stem from relatively poor crystallite statistics of the standard specimen. The actual photon flux in the collimated beam realized by the combination of rotating anode operating with a micro focus and

single-reflection mirror has been measured by placing a pin diode on the sample stage and is of the order of  $10^9$  photons per second.

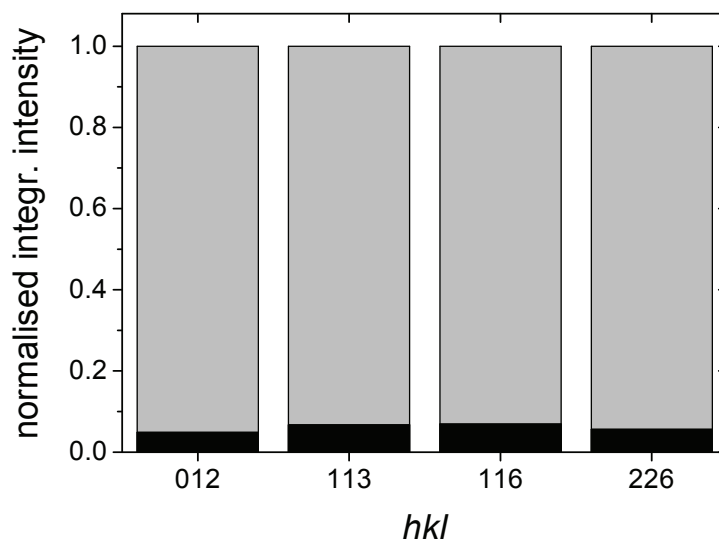


**Figure 6.11.** Normalised integrated intensity of four  $\text{Al}_2\text{O}_3$  diffraction lines measured with the Kirkpatrick-Baez optic (black columns) and with single-reflection mirror (gray columns).

The comparably low intensity obtained with the K-B optic is caused by the mirror positioned further away from the source, having a lower collection angle than the mirror positioned closer to the source, which reduces the photon flux in the collimated beam significantly with respect to the single-reflection mirror (see chapter 6.2.3.2). Additionally, the materials used for the fabrication of the multilayers of the mirrors and their ageing – thus causing imperfections – can be reasons for the measured intensity difference.

It has to be noted that the above discussed measurements do not provide a direct comparison of the brilliance. An estimate for the difference in brilliance (i.e. photon flux divided by beam size, divergence and bandwidth) can be obtained as follows (as Cu  $K\alpha$  radiation is used for both optics, the bandwidth is not taken into account in the following comparison): Assuming for the single-reflection mirror in comparison to the K-B optic a flux gain of factor 14 (see above), a beam size twice as large (see chapter 6.4 and note that this is a conservative estimate in favour of the K-B optic) and a beam divergence being 1.2 times larger (see chapters 6.3, 6.4 and 6.5.1) in the tangential as well as in the saggital direction, the gain factor in brilliance can be estimated as

$$\frac{14}{2 \times 1.2^2} \approx 4.9. \quad (6.4)$$

### 6.5.3. Instrumental effects in XRD experiments employing parallel-beam geometry

In the absence of any instrumental aberrations both the diffraction line shape and the integrated intensity of a texture-free powder specimen should be independent of the orientation of the diffraction vector with respect to the specimen frame of reference (see chapter 6.2.1.1). This means, any change of the diffraction line shape and/or (integrated) intensity or upon tilting and/or rotating this specimen corresponds to an instrumental aberration which should be corrected for.

#### 6.5.3.1. Peak shape

To find out if there is any influence of the orientation of the diffraction vector, with respect to the specimen frame of reference, on peak shape, the peak parameters diffraction line width HWHM, shape parameter  $\eta$  and asymmetry  $\alpha$  of the 110 and 310 reflections of a stress- and texture-free tungsten powder standard have been investigated as a function of the specimen orientation  $\varphi$  (rotation) and  $\psi$  (tilt) in  $\chi$  mode (see chapter 6.2.1.2). The results obtained for the peak parameters as a function of  $\psi$  for the tungsten 110 ( $2\theta \approx 40^\circ$ ) and 310 ( $2\theta \approx 100^\circ$ ) reflections are shown in Figure 6.12. The results for the peak parameters of the tungsten 310 reflection as a function of  $\varphi$  are shown for two different tilt angles ( $\psi = 0^\circ$ ;  $\psi = 80^\circ$ ) in Figure 6.13. It follows that the investigated parameters show no dependence on  $\varphi$  and  $\psi$ . Only for high tilt angles slight deviations of the HWHM and the shape parameter from the trend of the other measured data points occur. As a result it is clear that a defocusing correction is not required for the diffractometer.

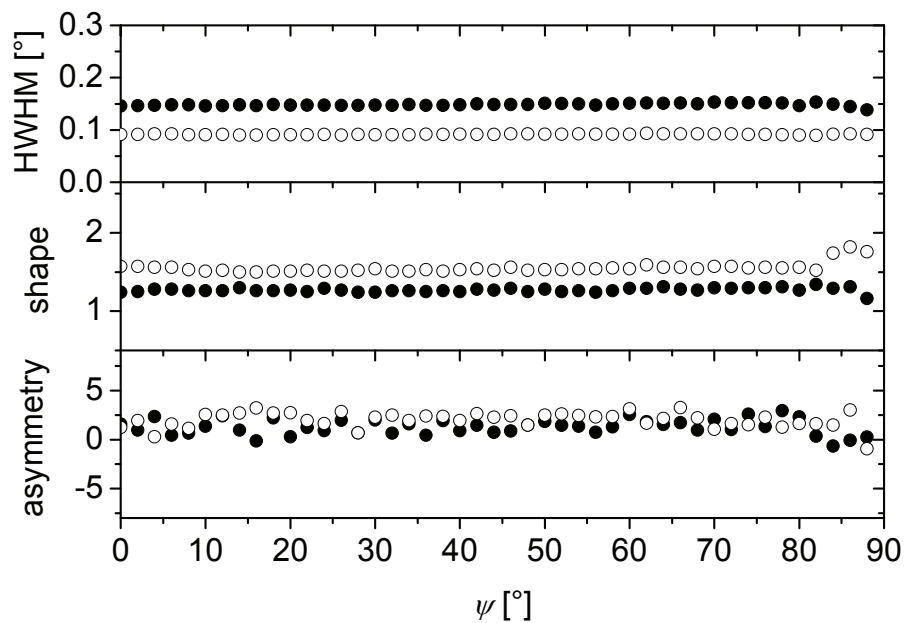


**Figure 6.12.** Peak parameters of the tungsten 110 and 310 reflections (open and filled circles, respectively) as a function of specimen tilt angle  $\psi$ . Error bars have been omitted as their size is of the order of the symbol size.

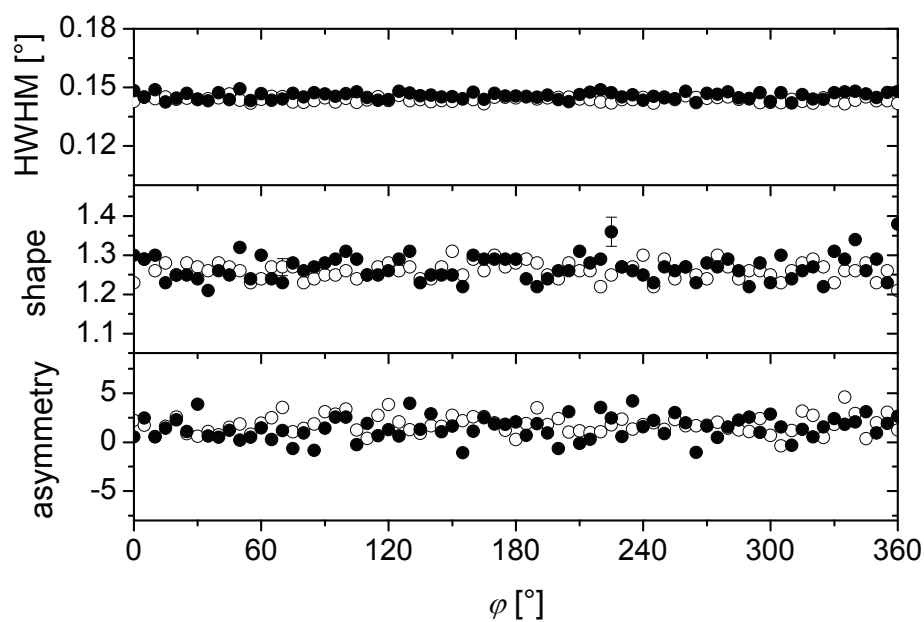


**Figure 6.13.** Peak parameters of the tungsten 310 reflection as a function of specimen rotation angle  $\phi$  for two different tilt angles:  $\psi = 0^\circ$  (open circles) and  $\psi = 80^\circ$  (filled circles). Only representative error bars have been shown for the sake of clarity.

### 6.5.3.2. Peak intensity

The peak intensities of the 110 and 310 diffraction lines have been measured as functions of the specimen tilt angle  $\psi$  for the tungsten powder specimen. The result of this experiment is shown in Figure 6.14.

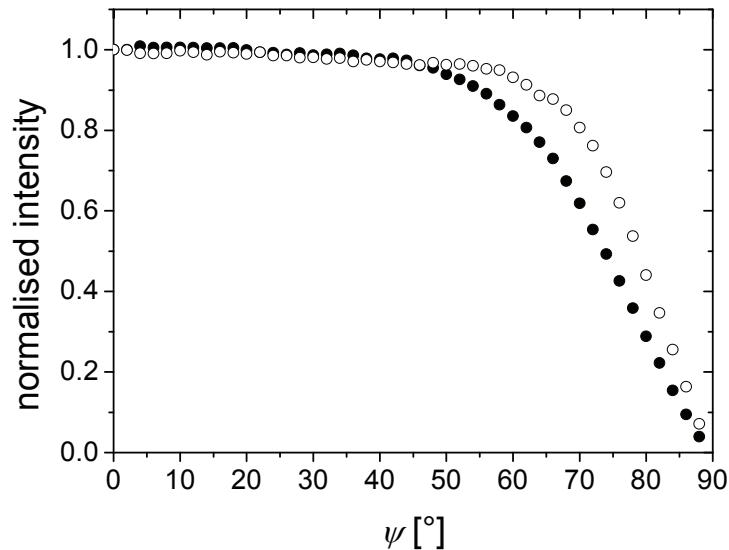


**Figure 6.14.** Peak intensity of the tungsten 110 (filled circles) and 310 (open circles) reflections recorded as a function of specimen tilt angle  $\psi$ . Error bars have been omitted as their size is of the order of the symbol size.

It follows that for each reflection up to a certain tilt angle the intensity stays practically constant. This is due to the compensation of increase in intensity by increase in illuminated specimen area by the decrease in intensity caused by absorption. The intensity decrease at higher tilt angles is caused by instrumental intensity loss. The extent of instrumental intensity loss is decreasing with increasing diffraction angle.

## 6.6. Comparative discussion

### 6.6.1. Simulation versus experiment

The calculated tangential beam divergence resulting from the single-reflection collimating mirror corresponds very well with the experimentally determined beam divergence (cf. chapter 6.5.1). Also the beam shape shown in Figure 6.3 is in good qualitative agreement with the measured beam shape (rotated by 90°; see Figure 6.9).

The experimentally determined gain in diffracted intensity upon substituting the K-B optic by the single-reflection mirror (cf. chapter 6.5.2) surpasses the calculated value (cf. equation (6.2)). This discrepancy can be made plausible considering that: (i) the single-reflection mirror and the K-B optic are not composed of identical multilayer materials, as assumed in the ray-tracing calculation; (ii) different ageing conditions may also contribute to different efficiencies.

### 6.6.2. X-ray mirrors versus X-ray lenses

In principle parallel beam geometry in point-focus configuration can be realized by two kinds of collimating primary optics: X-ray mirrors or X-ray lenses. Both devices have certain advantages and disadvantages depending on the type of measurement to be conducted and the specimen under investigation. They can be compared on the basis of several parameters.

*Photon flux:* When a conventional sealed tube (type KFF - short fine focus or LFF - long fine focus) is employed as X-ray source the photon flux of the primary beam obtained with an X-ray lens is much higher than the flux attained by an X-ray mirror. Because collimation is achieved by multiple total reflections of the X-rays at the inner walls of (millions of) bent hollow glass fibres X-ray lenses have a much larger acceptance for photons produced by the anode than X-ray mirrors, where X-rays are collimated by Bragg reflection of the produced radiation at a graded multilayer system. However, the minimum divergence achievable by capillary lenses is equivalent to twice the critical angle of total external reflection of the lens material. Their beam qualities thus lie far behind those obtained by collimating mirrors. Among X-ray mirrors the serial Kirkpatrick-Baez configuration is accompanied by an additional flux loss, because the second mirror which is further away from the source

has a smaller acceptance for the produced photons than the first mirror which is located closer to the source. In order to improve the photon flux through an X-ray mirror it is necessary to employ a source where a small (point) focus at comparably high power can be realized, i.e. preferably a rotating anode source. If such a source is available photon fluxes of the order of  $10^9$  photons per second can be achieved making the flux in a laboratory diffractometer comparable, however with less angular resolution, with the flux obtained at second generation synchrotron beamlines (see, for example, Ref. [25]).

*Beam size:* The desired cross section of the incident beam depends on the type of specimen and experiment: When diffraction information is required from a large area, X-ray lenses have to be favoured, because they are capable of collimating a beam with typical cross sections between  $5 \times 5 \text{ mm}^2$  and  $10 \times 10 \text{ mm}^2$ , whereas X-ray mirrors for laboratory diffractometers produce collimated beams with cross sections of only about  $1 \times 1 \text{ mm}^2$ . A problem, which can arise when such a small cross section of the incident beam is employed, is the statistics of the diffracting crystallites. For coarse grained specimens, such small beam sizes cause statistical problems in the diffracted signal as the number of crystallites contributing to the diffraction signal becomes too low (this drawback can be partly compensated by oscillating or spinning the specimen). However, if diffraction information from a small spot on the specimen is required (known as microdiffraction), X-ray mirrors in combination with a microfocus source should be the choice.

*Beam divergence:* Similar to beam size the desired beam divergence depends on the specimen under investigation and the type of experiment to be carried out. A collimating X-ray mirror typically produces a beam with a divergence of about 0.8 mrad employing Cu  $K\alpha$  radiation. Particularly for grazing incidence experiments this amount of divergence is well acceptable. In measurements with controlled penetration depth the divergence of the incident beam should be minimal because the incident beam angle is one of the parameters determining the penetration depth. The same problem concerning the statistics of the diffracting crystallites, which can arise when a small beam cross section is employed, occurs when the divergence of the incident beam is very low. Also in this case only a limited number of crystallites are in diffraction condition and the shape of the measured diffraction line can become affected and/or the measured diffraction signal is not representative for the specimen.

However, if the specimens investigated are limited to fine-grained materials as polycrystalline thin films, the crystallite sizes are generally low enough so that crystallite-statistic problems do not occur.

The divergence of an X-ray lens is about one order of magnitude higher than that of a collimating X-ray mirror. This feature makes X-ray lenses especially suitable for experiments employing specimens with a large crystallite size. In this case it is necessary to collect diffraction information from a larger crystallite orientation range to improve crystallite statistics.

*Monochromatisation:* Due to collimation by diffraction, X-ray multilayer mirrors also serve as monochromators. Commonly they are adjusted such that the  $K\beta$  components as well as Bremsstrahlung are (sufficiently) suppressed by the mirror and the collimated beam then largely consists of the  $K\alpha$  components of the employed radiation.

When an X-ray lens is utilized it is necessary to install additionally either a filter or a monochromator to separate Bremsstrahlung,  $K\beta$  and other parasitic radiation components (as tungsten L lines resulting from a contamination of the anode), which results in an additional loss of photon flux.

*Angular resolution:* In a parallel beam diffractometer the angular resolution depends on two main factors: the divergence of the incident beam collimated by the primary optic and the acceptance angle of the secondary optic. For the same secondary optic the parallel beam laboratory diffractometer has – owing to the residual divergence of the collimated beam – a better angular resolution if an X-ray mirror is employed rather than if a lens is employed.

Generally speaking the resolution of a state-of-the-art parallel beam laboratory diffractometer is lower than the resolution of a laboratory diffractometer employing a focusing geometry as long the specimen is not tilted, i.e. as long as  $\psi = 0$ . However, as mentioned before, for the investigation of the microstructure of materials by X-ray diffraction it is necessary to perform XRD analyses also at several angles  $\psi$  different from zero. For such analyses parallel beam diffractometers should be favoured in any case, as in focusing geometries tilting the specimen leads to additional instrumental broadening (i.e. defocusing) and thus to a significant reduction in angular resolution.



For a given type of application the user thus can decide on the basis of the here discussed advantages and disadvantages which type of diffraction geometry and primary optic has to be employed.

## **6.7. Summary**

The use of a single-reflection two-dimensional collimating X-ray mirror in a laboratory diffractometer results in the following features:

- A curved rectangular shaped collimated primary beam with a residual divergence of  $0.06^\circ$  (1 mrad). The actual photon flux realized by the mirror in the given instrumental configuration has been determined as of the order of  $10^9$  photons per second.
- A significant gain in diffracted beam intensity as compared to application of a Kirkpatrick-Baez optic.
- The instrumental broadening has been found independent of the orientation of the diffraction vector with respect to the specimen fame of reference.
- Instrumental aberrations are limited to instrumental intensity loss due to a part of the incident beam not “hitting” the specimen and a part of the diffracted beam not recorded by the detector.

## **Acknowledgements**

The authors would like to thank Prof. Dr. Ir E. J. Mittemeijer for constructive discussions throughout the work and a critical review of the manuscript.

## References

- [1] Welzel, U. & Mittemeijer, E. J. (2005). *Powder Diffr.* **20**, 376.
- [2] Fitch, A.N. (1995). *Nucl. Instrum. Methods Phys. Res., Sect. B* **97**, 63.
- [3] Guinebretière, R., Boulle, A., Masson, O. & Dauger, A. (2005). *Powder Diffr.* **20**, 294.
- [4] Vermeulen, A. C. (2005). *Mater. Sci. Forum* **490-491**, 131.
- [5] Scardi, P., Setti, S. & Leoni, M. (2000). *Mater. Sci. Forum* **321-324**, 162.
- [6] Kumakhov, M.A. & Komarov, F.F. (1990). *Phys. Rep.* **191**, 289.
- [7] Kogan, V.A. & Bethke, J. (1998). *Mater. Sci. Forum* **278-281**, 227.
- [8] Schields, P.J., Gibson, D.M., Gibson, W.M., Gao, N., Huang, H. & Ponomarev, I.Y. (2002). *Powder Diffr.* **17**, 70.
- [9] Schuster, M. & Göbel, H. (1995). *J. Phys. D* **28**, A270.
- [10] Jiang, L., Al-Mosheky, Z. & Grupido, N. (2002). *Powder Diffr.* **17**, 81.
- [11] Sun, T. & Ding, X. (2005). *J. Appl. Phys.* **97**, 124904.
- [12] Welzel, U. & Leoni, M. (2002). *J. Appl. Cryst.* **35**, 196.
- [13] Leoni, M., Welzel, U. & Scardi, P. (2004). *J. Res. Natl. Inst. Stand. Technol.* **109**, 27.
- [14] Kirkpatrick, P. & Baez, A.V. (1948). *J. Opt. Soc. Am.* **38**, 766.
- [15] Montel, M. (1954). *Optica Acta* **1**, 117.
- [16] Welzel, U., Ligot, J., Lamparter, P., Vermeulen, A.C. & Mittemeijer, E.J. (2005). *J. Appl. Cryst.* **38**, 1.
- [17] Kumar, A., Welzel, U. & Mittemeijer, E. J. (2006). *J. Appl. Cryst.* **39**, 633.
- [18] Fitch, A.N., Catlow, C.R.A. & Atkinson, A. (1991). *J. Mater. Sci.* **26**, 2300.
- [19] Vermeulen, A.C. & Götz, D. (2006). *ECRS 7*. Berlin
- [20] Wilson, A. J. C. (1995). Editor. *International Tables for Crystallography*, Dordrecht: Kluwer.
- [21] Bunge, H. J. (1999). *Texture and structure of polycrystals*, in: *Defect and Microstructure Analysis by Diffraction*, edited by R. L. Snyder, J. Fiala & H. J. Bunge, Vol. pp. 405. Oxford University Press.
- [22] Delhez, R., de Keijser, Th. H. & Mittemeijer, E. J. (1987). *Surf. Eng.* **3**, 331.
- [23] Sonneveld, E. J., Delhez, R., De Keijser, Th. H. & Mittemeijer, E. J. (1991). *Mater. Sci. Forum* **79-82**, 85.

- [24] Hölzer, G., Fritsch, M., Deutsch, M., Härtwig, J. & Förster, E. (1997). *Phys. Rev. A* **56**, 4554.
- [25] Eiper, E., Martinschitz, K. J., Gerlach, J. W., Lackner, J. M., Zizak, I., Darowski, N. & Keckes, J. (2005). *Z. Metallkd.* **96**, 1069.



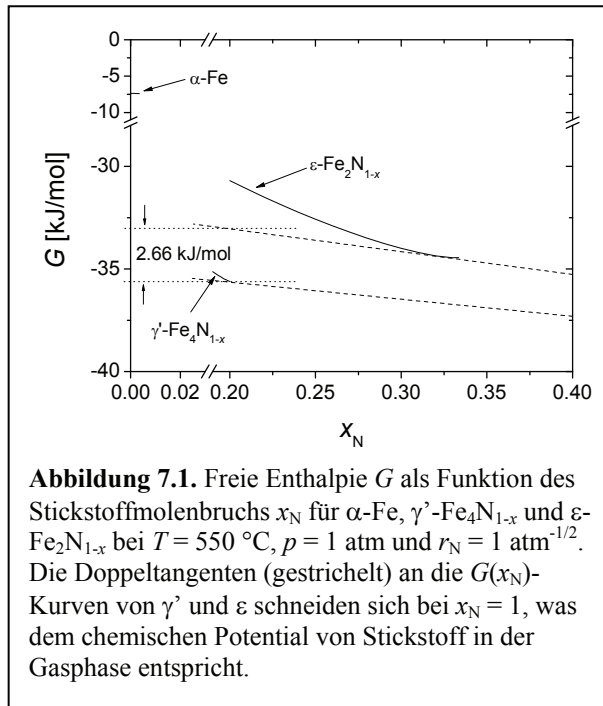
## **7. Kurzfassung der Dissertation in deutscher Sprache**

### **7.1. Einleitung**

Wichtige Eigenschaften von dünnen Schichten, die Einfluss auf die physikalischen Eigenschaften haben, sind die Mikrostruktur und der Eigenspannungszustand. So kann zum Beispiel eine nanokristalline Mikrostruktur dazu führen, dass Phasengleichgewichte beeinflusst werden, oder dass sich der thermische Ausdehnungskoeffizient verändert. Eigenspannungen in dünnen Schichten können im Extremfall zum mechanischen Versagen eines Systems aus dünner Schicht und Substrat durch Delamination (im Fall von Druckeigenspannungen) oder durch Reißen (im Falle von Zugeigenspannungen) der Schicht führen. Ziel dieser Arbeit ist es, Einflüsse der Mikrostruktur auf die Eigenschaften von dünnen Schichten, insbesondere auf den Eigenspannungszustand, anhand ausgewählter Beispiele aufzuzeigen und zu analysieren.

### **7.2. Unerwartete Bildung von $\epsilon$ -Eisennitrid beim Gasnitrieren nanokristalliner $\alpha$ -Fe-Schichten**

Die Phasenbildung beim Gasnitrieren nanokristalliner Eisenschichten (Dicke ca. 200 nm) auf inerten Substraten ( $\alpha$ -Al<sub>2</sub>O<sub>3</sub>-Wafer) wird im zweiten Kapitel der Arbeit untersucht. Es wurde bei der Untersuchung der gebildeten Eisennitridschichten festgestellt, dass sich die Phase  $\gamma'$ -Fe<sub>4</sub>N<sub>1-x</sub>, welche bei den eingestellten Bedingungen die nach dem allgemein akzeptierten „Lehrerdiagramm“ [1,2] zu erwartende Phase darstellt, gebildet hat. Überraschenderweise bildete sich jedoch darüber hinaus bei einer Probe mit einer sehr geringen durchschnittlichen lateralen Kristallitgröße von etwa 80 nm (durchschnittliche Kristallitgröße der Schichten die nur  $\gamma'$ -Fe<sub>4</sub>N<sub>1-x</sub> bilden: ca. 400 nm) zusätzlich die Phase  $\epsilon$ -Fe<sub>2</sub>N<sub>1-x</sub>, welche unter den eingestellten Nitrierbedingungen nicht zu erwarten gewesen wäre.



Diese Beobachtung legt nahe, dass eine nanoskalige Korngröße der Grund für die Bildung des  $\epsilon$ -Eisennitrids sein könnte. Die Berechnung der freien Enthalpie  $G$  der Phasen  $\alpha$ ,  $\epsilon$  und  $\gamma'$  als Funktion des Stickstoffmolenbruchs  $x_N$  unter Zuhilfenahme thermodynamischer Daten aus [3-6] zeigt (siehe Abbildung 7.1), dass ein Anstieg der freien Enthalpie von  $\gamma'$  um 2,66 kJ/mol notwendig ist, damit die  $\epsilon$ -Phase unter den oben genannten

Bedingungen stabil ist. Dieser Anstieg kann durch den Gibbs-Thomson-Effekt verursacht werden:  $\Delta G = (2\gamma V_m)/r$ , wobei  $\gamma$  für die Grenzflächenenergie,  $V_m$  für das molare Volumen und  $r$  für den Radius eines nanokristallinen Partikels einer bestimmten Phase stehen [7]. Als Radius der  $\gamma'$ -Kristallite, die sich während des Nitrierens bilden, können 40 nm abgeschätzt werden (siehe Kapitel 2). Daraus folgt, dass die Grenzflächenenergie der Phase  $\gamma'$  ungefähr 1,6 J/m<sup>2</sup> beträgt, was einen durchaus realistischen Wert darstellt [7]. Damit konnte gezeigt werden, dass die Thermodynamik des Systems Eisen-Stickstoff signifikant durch Kristallitgrößeneffekte beeinflusst werden kann.

### 7.3. Kristallitgrößenabhängigkeit des thermischen Ausdehnungskoeffizienten von Metallen

In der Literatur findet man mehrere widersprüchliche Beobachtungen bezüglich einer möglichen Kristallitgrößenabhängigkeit des thermischen Ausdehnungskoeffizienten (ThAK) [8-10]. Unter Zuhilfenahme aktueller methodischer Entwicklungen kann die Kristallitgrößenabhängigkeit des ThAK mittels temperaturabhängiger in-situ Röntgendiffraktometrie verfolgt werden.

In den Experimenten wurden Cu und Ni Dünnschichten (die nominellen Dicken waren jeweils 50 nm) auf Si-Wafern verwendet, die bei Raumtemperatur mittels Gleichstrom-Magnetronspütern abgeschieden wurden.

Röntgenbeugungsmessungen wurden an einem Diffraktometer, das mit einer auf einer Eulerwiege montierten Heiz-/Kühlkammer ausgerüstet war, durchgeführt (siehe Kapitel 3.2 für Details der Röntgenbeugungsmessungen).

Zunächst wurden aus temperaturabhängigen röntgenographischen in-situ Eigenspannungsmessungen im Temperaturbereich  $-100^{\circ}\text{C}$  bis  $25^{\circ}\text{C}$  spannungsfreie Gitterebenenabstände der Cu und Ni Schichten ermittelt. Die ThAKs werden aus den Steigungen der Ausgleichsgeraden in den Auftragungen von thermischer Dehnung,  $\varepsilon_{\text{th}}$  ( $= \Delta d/d_0$ , wobei  $d_0$  der Abstand bestimmter Gitterebenen bei Raumtemperatur und  $\Delta d$

**Tabelle 7.1.** Gegenüberstellung der Ausdehnungskoeffizienten  $\alpha$  und Kristallitgrößen der untersuchten Kupfer- und Nickelschichten vor und nach der Wärmebehandlung. Zum Vergleich wurden auch Literaturwerte für die Ausdehnungskoeffizienten von Kupfer und Nickel angegeben [11,12].

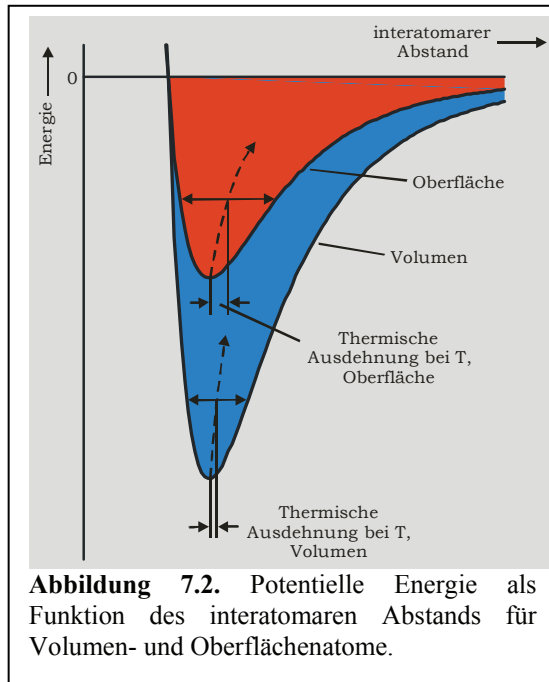
	$\alpha$ von Ni [ $10^{-6}/^{\circ}\text{C}$ ]	$\alpha$ von Cu [ $10^{-6}/^{\circ}\text{C}$ ]
Nach der Herstellung	$13.7 \pm 0.4$	$18.8 \pm 0.4$
Nach der Wärmebehandlung	$12.6 \pm 0.2$	$17.4 \pm 0.4$
Literaturwert für grobkristalline Materialien	12.4	15.7

	Korngröße $D$ von Ni [nm]	Korngröße $D$ von Cu [nm]
Nach der Herstellung	37	26
Nach der Wärmebehandlung	59	41

die Änderung des Gitterebenenabstands bei einer Temperaturänderung um  $\Delta T$  ist), gegen Temperatur,  $T$ , bestimmt. Es wurde beobachtet, dass die ThAKs der nanokristallinen Cu- und Ni-Schichten direkt nach der Herstellung signifikant größer sind als Werte, die für grobkristallines Cu- und Ni-Volumenmaterial erhalten werden. Es hat sich als sehr wichtig erwiesen, dass die

Messungen der ThAK bei Temperaturen unterhalb der Raumtemperatur durchgeführt werden konnten. Es konnte nämlich durch in-situ Röntgenbeugungsmessungen gezeigt werden, dass bei Temperaturen oberhalb der Raumtemperatur sehr schnell eine Vergrößerung der Kornstruktur einsetzt. Nach dieser Vergrößerung ergeben sich die für grobkristalline Vielkristalle erwarteten Ausdehnungskoeffizienten (Tabelle 7.1).



Die Abhängigkeit des ThAK von der Kristallitgröße kann verstanden werden, wenn man die Bindungsverhältnisse an Korngrenzen und Oberflächen betrachtet. Atome an der Oberfläche eines Kristalls oder an einer (inkohärenten) Grenzfläche (Korngrenze) sind im Bezug auf ihren Bindungszustand ungesättigt; ihre Koordinationszahl ist geringer als die der Atome im Volumen. In Folge dessen ergeben sich entsprechend unterschiedliche Potentialverläufe

(Energie gegen interatomaren Abstand; siehe Abbildung 7.2). Für Atome an Oberflächen zeigt die Potentialkurve ein weniger tiefes Minimum und verläuft asymmetrischer als für Atome im Volumen. Gleiche thermische Energien führen durch die Asymmetrie der Potentialverläufe nun zu unterschiedlichen thermischen Ausdehnungen für Atome an Oberflächen und im Volumen. Je kleiner ein Kristallit ist, desto größer ist das Verhältnis der Anzahl der Oberflächenatome zur Anzahl der Atome im Volumen. Folglich ist die *mittlere* thermische Ausdehnung eines Kristallites umso größer, je kleiner der Kristallit ist.

## 7.4. Bestimmung von Gradienten effektiver

### Kornwechselwirkung und Spannung in dünnen Cu-Schichten

Das vierte Kapitel der Arbeit beschäftigt sich mit der röntgenographischen Ermittlung tiefenabhängiger Verläufe von effektiver Kornwechselwirkung und Eigenspannungen in Cu-Schichten, bei deren Herstellung die Abscheidebedingungen zur Erzeugung eines Eigenspannungsgradienten variiert wurden: Die Ermittlung der Gradienten wurde mittels Röntgenbeugungsmessungen bei konstanter Eindringtiefe durchgeführt (für weitere Details zur Messmethode und der ihr zugrunde liegenden Einschränkungen siehe Kapitel 4.2.1 und [13]). Auf diese Weise wurden pro Eindringtiefe mehrere Beugungslinien  $hkl$  über den jeweils zugänglichen  $\psi$ -Bereich



aufgenommen. Die Absorption des untersuchten Materials wurde durch Variation der Energie  $E$  der Röntgenstrahlen so eingestellt, dass ein möglichst großer Eindringtiefenbereich abgedeckt werden konnte. Dazu wurden Messungen an einem Labordiffraktometer ( $E = 8.048$  kV) und an einer Synchrotron-Strahlquelle („Surface Diffraction Beamline“, Ångströmquelle Karlsruhe (ANKA),  $E = 9.996$  kV) durchgeführt (zu Details der Röntgenbeugungsmessungen siehe Kapitel 4.3.4). Bei der Verwendung kleiner Einfalls-(oder Austritts-)winkel ( $< 2,5^\circ$ ) ist der Brechungseffekt zu berücksichtigen: Dieser bewirkt bei einer ideal glatten Oberfläche eine Veränderung des Einfalls- und Austrittswinkels der Röntgenstrahlen und somit eine Veränderung des gemessenen Beugungswinkels. Es ist daher notwendig, die so gemessenen Beugungswinkel unter Anwendung einer Brechungskorrektur zu korrigieren (zu Details siehe [14] und Kapitel 4.2.2). Weist die Probe eine gewisse Oberflächenrauigkeit auf, reduziert sich dadurch der Brechungseffekt, was dazu führt, dass der mittels Brechungskorrektur berechnete Fehler des gemessenen Beugungswinkels überschätzt wird (siehe [15] und Kapitel 4.2.2).

Die Auswertung der gemessenen Netzebenenabstände erfolgte auf Basis der  $f(\psi, hkl)$ -Methode (siehe [16-18] und Kapitel 4.2.3). Mit Hilfe dieser Methode ist es möglich, einen Gewichtungparameter  $w$ , welcher effektive röntgenographische elastische Konstanten (REK) nach  $S_{1,2}^{hkl} = wS_{1,2}^{hkl,V} + (1-w)S_{1,2}^{hkl,R}$  definiert, einzuführen, wobei die hochgestellten Buchstaben „V“ und „R“ für das Voigt- bzw. das Reuss-Modell der elastischen Kornwechselwirkung stehen. Auf diese Weise gelingt es, effektive REK durch eine Anpassung auf Basis der kleinsten Quadrate mit  $w$  als anzupassenden Parameter als Funktion der Eindringtiefe/Informationstiefe zu erhalten (zu weiteren Details siehe Kapitel 4.2.3).

Die ca. 4  $\mu\text{m}$  dicken Cu-Schichten wurden mittels Magnetronspütern in einer Ultrahochvakuumkammer auf einen thermisch oxidierten,  $\langle 100 \rangle$ -orientierten Si-Wafer mit einer Dicke von 500  $\mu\text{m}$  abgeschieden. Dabei wurde die erste Hälfte der Schichtdicke bei einer Substrattemperatur von 400  $^\circ\text{C}$  aufgebracht, und die Probe anschließend auf Raumtemperatur abgekühlt. Anschließend wurde die zweite Hälfte der Schichtdicke abgeschieden. Das Ziel dieser Zwei-Stufen-Abscheidung war die Erzeugung eines Eigenspannungsgradienten in der dünnen Schicht. Zu weiteren Details der Probenherstellung siehe Kapitel 4.3.1.

Eine Untersuchung der Mikrostruktur mittels fokussierender Ionenstrahlmikroskopie ergab, dass die Schicht sowohl aus kolumnaren als auch aus globularen Körnern besteht (siehe Abbildung 4.2 in Kapitel 4.4.1). Die Oberflächenrauigkeit der Schicht wurde mittels Rasterkraftmikroskopie untersucht und es wurden die folgenden Rauigkeitswerte bestimmt (zu Details siehe Kapitel 4.3.3):  $R_a = 63,9(4)$  nm;  $R_{ms} = 80,9(6)$  nm. Dieses Maß an Oberflächenrauigkeit reduziert den Brechungseffekt, welcher bei der Verwendung kleiner Einfalls- (oder Austritts-)winkel auftritt, sodass die Anwendung einer Brechungskorrektur bei kleinen Einfalls- (oder Austritts-)winkeln zu fehlerhaften Ergebnissen führt [15].

In Abbildung 7.3 sind Ergebnisse für die Gradienten effektiver Kornwechselwirkung und Eigenspannung dargestellt. Es zeigt sich, dass bei der untersuchten Probe sowohl die Anwendung als auch die Vernachlässigung der Brechungskorrektur bei Messungen mit kleinem Einfallswinkel zu fehlerhaften Ergebnissen bezüglich effektiver Kornwechselwirkung wie auch Eigenspannung führt. Der Grund hierfür ist die oben besprochene Oberflächenrauigkeit, welche den Brechungseffekt reduziert und somit weder korrigierte noch unkorrigierte Messungen

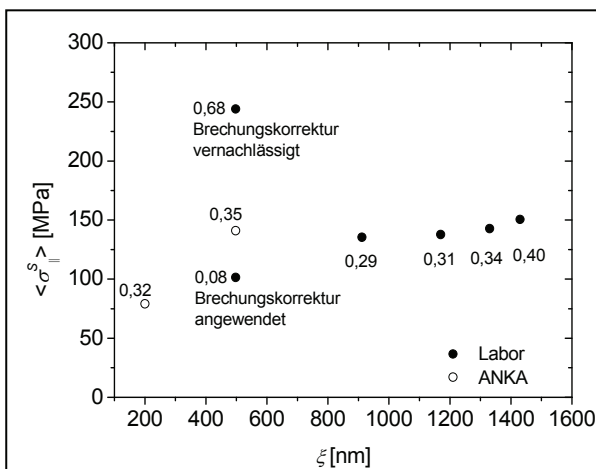


**Abbildung 7.3.** Mechanische Eigenspannung  $\langle \sigma_{\parallel}^S \rangle$  (Punkte) und Kornwechselwirkungsparameter  $w$  (Zahlen über den Datenpunkten) als Funktion der Informationstiefe. Die Auswertung der Labormessung bei der kleinsten Tiefe wurde zweimal durchgeführt: einmal unter Berücksichtigung und einmal ohne Berücksichtigung der Brechungskorrektur. Fehlerbalken sind nicht dargestellt, da sie in etwa der Symbolgröße entsprechen.

realistische Werte hervorbringen. Es wird daher vorgeschlagen, auf die Verwendung kleiner Einfalls- (oder Ausfalls-)winkel ( $< 2,5^\circ$ ) zu verzichten und stattdessen die Absorption durch Wahl geeigneter Photonenenergie so einzustellen dass geringe Eindringtiefen bei entsprechend großen Einfalls- (oder Ausfalls-)winkeln untersucht werden können. Die beobachtete Kornwechselwirkung ist über den gesamten untersuchten Tiefenbereich eher Reuss-artig als Voigt-artig (Abbildung 7.3). Mit

abnehmender Probentiefe tendiert der Kornwechselwirkungscharakter eher noch weiter in Richtung Reuss-artige Wechselwirkung. Dies ist mit der Mikrostruktur der dünnen Schicht zu erklären: Die Mikrostruktur der Schicht besteht sowohl aus

kolumnaren als auch aus globularen Körnern. Bei dünnen Schichten ist für beide Kornmorphologien zu erwarten dass der Reuss-Charakter der Kornwechselwirkung mit zunehmender Annäherung an die Probenoberfläche zunimmt (zu weiteren Details siehe Kapitel 4.4.4). In Abbildung 7.3 ist zu erkennen, dass die angewendete Zwei-Stufen-Abscheidung zu einer Spannungsvariation von 80 MPa nahe der Probenoberfläche bis 150 MPa nahe der Probenmitte geführt hat. Zur weiteren Diskussion der tiefenabhängigen Kornwechselwirkungs- und Eigenspannungsverläufe siehe Kapitel 4.4.4.

## **7.5. Tiefenprofile von Eigenspannung und dehnungsfreiem Gitterparameter in einer $\gamma'$ -Fe<sub>4</sub>N<sub>1-x</sub>-Schicht**

Die Variation von Eigenspannung und Gitterparameter mit der Probentiefe in einer  $\gamma'$ -Fe<sub>4</sub>N<sub>1-x</sub>-Schicht, welche durch Gasnitrieren eines  $\alpha$ -Fe-Substrates hergestellt wurde, ist Gegenstand des fünften Kapitels der Arbeit. Wie im vorhergehenden Kapitel wurde als Messmethode röntgenographische Eigenspannungsanalyse bei konstanter Eindringtiefe angewendet. Verfügt man über genaue Kenntnis der röntgenographischen elastischen Konstanten (REK), so ermöglicht diese Methode zusätzlich die Bestimmung des spannungsfreien Gitterparameters als Funktion der Probentiefe. Aus der Variation des spannungsfreien Gitterparameters lässt sich die Variation der Stickstoffkonzentration unter Zuhilfenahme einer direkten Beziehung beider Größen [19] ausrechnen.

Die durchschnittliche Dicke der durch Gasnitrieren (zu den Nitrierparametern siehe Kapitel 5.3.1) hergestellten  $\gamma'$ -Eisennitridschicht beträgt 6  $\mu\text{m}$  (zu Details der metallographischen Untersuchung siehe Kapitel 5.3.2). Weil die Schicht während der Herstellung ins Substrat hinein wächst, zeichnet sich die Schicht durch eine ebene Oberfläche, aber eine raue Grenzfläche zum Substrat, aus.

Die röntgenographische Phasenanalyse (zu Details siehe Kapitel 5.3.3 und 5.4.1) bestätigte, dass die hergestellte Schicht ausschließlich aus  $\gamma'$ -Fe<sub>4</sub>N<sub>1-x</sub> besteht. Zur Analyse der Tiefenprofile von Eigenspannung und spannungsfreiem Gitterparameter wurden Röntgenbeugungsmessungen bei konstanter Eindringtiefe [13] nach der  $\sin^2\psi$ -Methode [18] durchgeführt. Dabei wurden zwei verschiedene Wellenlängen (Messungen an einem Labordiffraktometer und an einer Synchrotron-

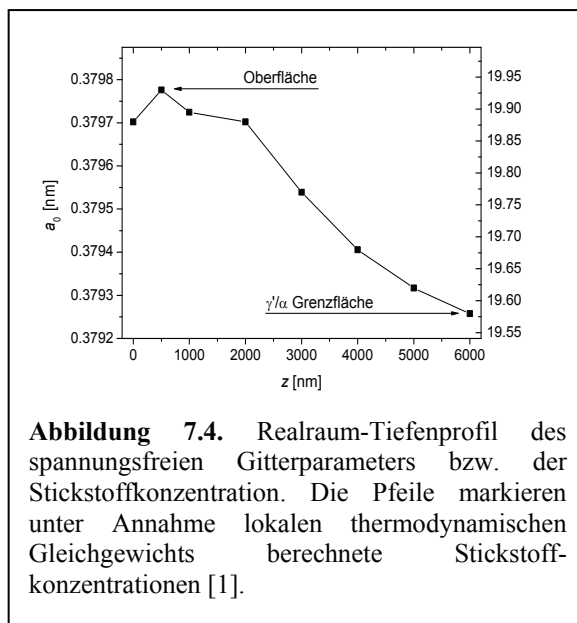
Strahlungsquelle; zu Details siehe Kapitel 5.3.3) verwendet, um den für die Messung zugänglichen Probentiefenbereich zu erweitern.

Es stellte sich heraus, dass der 311-Reflex am besten für die vorgesehenen röntgenographischen Analysen geeignet ist, da die REK der 311-Netzebenen am unempfindlichsten gegenüber einer möglichen Variation der Kornwechselwirkung mit Probentiefe sind (siehe Abbildung 5.5 in Kapitel 5.4.2.1).

Um aus den gemessenen Tiefenprofilen im Laplaceraum die entsprechenden Profile im Realraum zu erhalten wurde eine iterative Prozedur angewendet, bei der das Tiefenprofil im Realraum sukzessive angenähert wird (zu Details siehe Kapitel 5.2.3). Die aus den Röntgenbeugungsmessungen des 311-Reflexes bei konstanter Eindringtiefe erhaltenen Tiefenprofile von spannungsfreiem Gitterparameter bzw. Stickstoffkonzentration sind in Abbildung 7.4 dargestellt.

Das Tiefenprofil des spannungsfreien Gitterparameters zeigt eine Abnahme des Gitterparameters, und damit auch der Stickstoffkonzentration, mit zunehmender Tiefe. Dabei fällt auf, dass nahe der Oberfläche und an der  $\gamma'/\alpha$  Grenzfläche die ermittelten Stickstoffkonzentrationen den unter Annahme lokalen thermodynamischen Gleichgewichts berechneten Stickstoffkonzentrationen [1] entsprechen.

Das Tiefenprofil der Eigenspannung (siehe Abbildung 5.8 in Kapitel 5.4.2.2)



weist generell Druckeigenspannungen auf. Diese entstehen als Konsequenz der Überlagerung von thermischen Druckeigenspannungen (konstant über die Schichtdicke) und Druckeigenspannungen, die durch die sich über die Probentiefe verändernde Stickstoffkonzentration hervorgerufen werden (variierend über die Schichtdicke) [20]. Die Eigenspannung zeigt folgenden Verlauf: Der Spannungsbetrag nimmt mit zunehmender Probentiefe zunächst

zu, läuft durch ein Maximum und nimmt anschließend zur  $\gamma'/\alpha$  Grenzfläche hin wieder ab. Dieser Verlauf kann wie folgt erklärt werden: Nahe der Oberfläche erfolgt eine Spannungsrelaxation durch die Bildung von Poren und (durch die Koaleszenz

von Poren) Kanälen entlang von Korngrenzen. Mit zunehmender Probentiefe nimmt der Eigenspannungsbetrag durch die zur  $\gamma'/\alpha$  Grenzfläche hin abnehmende Stickstoffkonzentration ebenfalls ab. Zu weiteren Einzelheiten über die geschilderten Tiefenprofile siehe Kapitel 5.4.2.

## **7.6. Anwendung einer kollimierenden Einfachreflektions-Multilagenoptik für Röntgenbeugungsexperimente in Parallelstrahlgeometrie**

Im letzten Kapitel der Arbeit werden die Eigenschaften einer speziellen Röntgenoptik (Einfachreflektions-Röntgenspiegel (ERS); Xenocs FOX2D CU 12\_INF), welche aufgrund ihrer paraboloiden Form einen divergenten Röntgenstrahl mit nur einer Reflektion sowohl horizontal als auch vertikal parallelisieren kann (zu Details siehe Kapitel 6.2.3), sowohl theoretisch (auf der Basis von 'Ray-tracing'-Berechnungen) als auch experimentell (auf der Basis von Messungen an untexturierten Referenzproben) untersucht. Die Eigenschaften werden mit den Eigenschaften einer Kirkpatrick-Baez (K-B)-Optik (zwei hintereinander angeordnete, um  $90^\circ$  gegeneinander verdrehte parabolische Röntgenspiegel [21]), verglichen.

Dabei wurden zunächst die Primärstrahlquerschnitte, die Primärstrahldivergenzen, und der zu erwartende Intensitätsgewinn der ERS-Optik gegenüber der K-B-Optik ermittelt (siehe Kapitel 6.3). Es ergab sich ein um einen Faktor von ca. 4 (Gleichung 6.2) höherer Photonenfluss (ohne die Anwendung zusätzlicher Primärstrahlkollimatoren) bei vergleichbarer Strahldivergenz für die ERS-Optik.

Im Experimententeil wurde die Leistung des ERS in einem Parallelstrahldiffraktometer (Bruker AXS D8 Discover, zu den Details siehe Kapitel 6.4) ausführlich untersucht und mit der Leistung einer K-B-Optik verglichen. Dazu wurde der Querschnitt des Primärstrahls mittels einer Röntgenkamera visualisiert und seine Divergenz unter Anwendung des ERS mittels Rockingkurven am Reflex einer einkristallinen Siliziumprobe gemessen. Anschließend wurde die Intensität des diffraktierten Signals einer  $\text{Al}_2\text{O}_3$ -Standardprobe, wie sie aus der Verwendung des ERS resultiert, mit der Intensität, wie sie aus der Verwendung der K-B-Optik resultiert, verglichen. Es zeigte sich, dass bei vergleichbarer Strahldivergenz und ähnlichem Strahlquerschnitt die Intensität des diffraktierten Signals unter

Verwendung des ERS um einen Faktor 14 bis 20 höher ist als die Intensität unter Verwendung der K-B-Optik (siehe Kapitel 6.5.1 und 6.5.2).

Weiterhin wurden die instrumentelle Aberrationen (Abhängigkeit von Form und Intensität von Beugungslinien von der Orientierung des Beugungsvektors) des mit dem ERS ausgerüsteten Parallelstrahldiffraktometers mittels einer texturfreien Wolfram-Standardpulverprobe untersucht (zur Theorie siehe Kapitel 6.2.2) untersucht. Es zeigte sich, wie für die Parallelstrahlgeometrie theoretisch erwartet (siehe auch [22]), dass alle die Form einer Beugungslinie beschreibenden Peakparameter unabhängig von der Orientierung des Beugungsvektors bezüglich des Probenkoordinatensystems sind (siehe Abbildung 6.12 und Abbildung 6.13 in Kapitel 6.5.3.1) und sich die theoretisch erwartete Abhängigkeit der Intensität einer gemessenen Beugungslinie vom Kippwinkel zwischen dem Beugungsvektor und der Oberflächennormalen der Probe ergab (siehe auch [22] und Kapitel 6.5.3.2).

In einer vergleichenden Diskussion wurden zunächst Simulationen und Experimente gegenübergestellt. Dabei ergab sich, dass sowohl berechneter Strahlquerschnitt als auch berechnete Primärstrahldivergenz sehr gut mit den entsprechenden gemessenen Charakteristika übereinstimmen. Der experimentell bestimmte Intensitätsgewinn übertrifft den theoretisch berechneten Gewinn. Dies kann dadurch erklärt werden, dass einerseits ERS und K-B-Optik nicht – wie in den Simulationen angenommen – aus den gleichen Materialien aufgebaut sind und andererseits in Realität unterschiedliche Alterungszustände der beiden Optiken vorlagen.

## 8. Summary

### 8.1. Introduction

Microstructure and residual stress state are important properties of thin films which have a significant influence on the physical properties. As an example, a nanocrystalline microstructure can have an impact on phase equilibria or on the coefficient of thermal expansion. Residual stresses in thin films can lead to mechanical failure of a system composed of thin film and substrate due to delamination (in case of compressive residual stresses) or cracking (in case of tensile residual stresses) of the film. The aim of this work is to investigate interrelations of the microstructure and the properties of thin films, particularly the residual stress state, utilizing selected examples.

### 8.2. Unexpected formation of $\epsilon$ -iron nitride by gas nitriding of nanocrystalline $\alpha$ -Fe films

In the second chapter of this thesis the phase formation during gas nitriding of nanocrystalline iron thin films on inert substrates ( $\alpha$ -Al<sub>2</sub>O<sub>3</sub> wafers) is investigated. Qualitative phase analysis of the produced iron-nitride films revealed that the phase  $\gamma'$ -Fe<sub>4</sub>N<sub>1-x</sub>, which is expected to form according to the generally accepted „Lehrer diagram“ [1,2] under the conditions applied, indeed has formed. However, strikingly, the phase  $\epsilon$ -Fe<sub>2</sub>N<sub>1-x</sub>, which was not expected to form under the nitriding parameters applied, has formed additionally for a specimen exhibiting a very low average lateral crystallite size of about 80 nm (the average lateral crystallite size of films forming exclusively  $\gamma'$ -Fe<sub>4</sub>N<sub>1-x</sub> is about 400 nm).

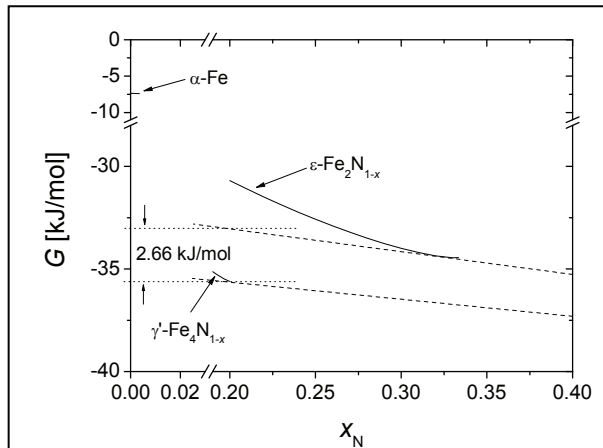


**Figure 8.1.** Gibbs free energy  $G$  as function of the atom fraction nitrogen  $x_N$  for  $\alpha$ -Fe,  $\gamma'$ -Fe<sub>4</sub>N<sub>1-x</sub> and  $\epsilon$ -Fe<sub>2</sub>N<sub>1-x</sub> at  $T = 550$  °C,  $p = 1$  atm and  $r_N = 1$  atm<sup>-1/2</sup>. The double tangents (dashed) to the  $G(x_N)$  curves of  $\gamma'$  and  $\epsilon$  intersect at  $x_N = 1$ , which corresponds to the chemical potential of nitrogen in the gas phase.

This observation leads to the assumption that a nanoscale grain size may be the reason for the formation of  $\epsilon$  iron nitride. The calculation of Gibbs energies,  $G$ , of the phases  $\alpha$ ,  $\epsilon$  and  $\gamma'$  as functions of atom fraction nitrogen,  $x_N$ , making use of thermodynamic data from Refs. [3-6] (see Figure 8.1) shows that an increase of 2.66 kJ/mol of the Gibbs energy of  $\gamma'$  is necessary, so that the  $\epsilon$  phase is stable. This

increase can be caused by the Gibbs-Thomson-Effect:  $\Delta G = (2\gamma V_m)/r$ , where  $\gamma$  is the interfacial energy,  $V_m$  the molar volume and  $r$  the radius of a nanocrystalline particle of a certain phase [7]. For the radius of the  $\gamma'$  crystallites, which form during nitriding a value of 40 nm can be estimated (cf. chapter 2). It follows that the interfacial energy of the phase  $\gamma'$  is about 1.6 J/m<sup>2</sup>, which indeed represents a realistic value [7]. It could thus be shown that the thermodynamics of the system iron-nitrogen can be significantly influenced by a nanoscale crystallite size.

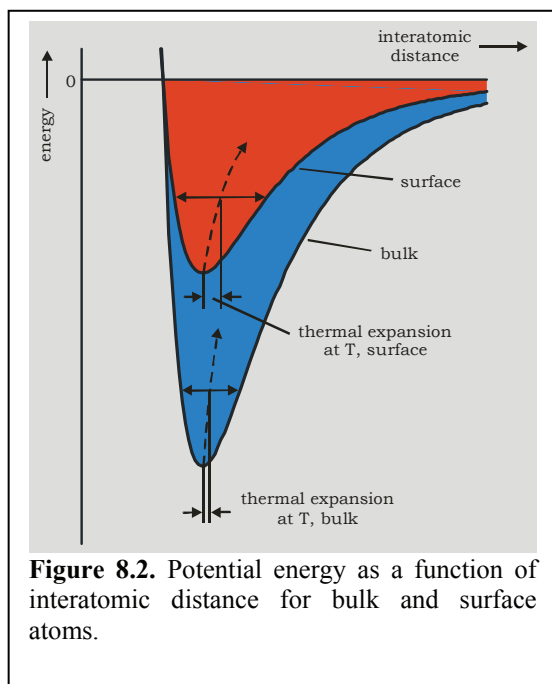
### 8.3. Crystallite-size dependence of the coefficient of thermal expansion of metals

In literature several contradictory findings concerning a possible crystallite-size dependence of the coefficient of thermal expansion (CTE) were obtained [8-10]. The crystallite-size dependence can be monitored by temperature-dependent in-situ X-ray diffraction (XRD) measurements making use of actual methodological developments.

In the experiments performed in this study Cu and Ni thin films (nominal thickness 50 nm each) deposited onto Si wafers by DC magnetron sputtering at room temperature were employed as specimens. XRD measurements were performed using a diffractometer equipped with a heating/cooling chamber mounted on an Eulerian cradle (cf. chapter 3.2 for details of the XRD measurements).

Firstly, the strain-free lattice parameters of the Cu and Ni films were determined from temperature-dependent in-situ XRD residual stress analysis in the





range between  $-100\text{ }^{\circ}\text{C}$  and  $25\text{ }^{\circ}\text{C}$ . The CTEs were determined from the slopes of plots of thermal strain,  $\varepsilon_{\text{th}} (= \Delta d/d_0$ , where  $d_0$  is the lattice plane spacing at room temperature and  $\Delta d$  is the change of lattice spacing due to a change of temperature  $\Delta T$ ), versus temperature,  $T$ . It has been found that the CTEs of the as-deposited nanocrystalline Cu and Ni films were significantly larger than the CTEs obtained for the corresponding coarse-grained bulk materials. It has turned out that it is very important to

perform the CTE measurements at temperatures below room temperature, because at temperatures above room temperature the nanocrystalline microstructure coarsens very quickly as could be shown by in-situ XRD measurements. After this coarsening has taken place, the CTEs of the corresponding bulk material are obtained. (Table 7.1).

The dependency of the CTE on crystallite size can be understood considering the states of bonding at grain boundaries and surfaces. Atoms at the surface of a crystal or at an (incoherent) interface (grain boundary) are not saturated with respect

**Table 8.1.** The measured CTE values of the Ni and Cu thin films and the corresponding literature values [11,12]. TF: Thin film specimen, CG: Coarse-grained specimen.

	CTE of Ni [ $10^{-6}/^{\circ}\text{C}$ ]	CTE of Cu [ $10^{-6}/^{\circ}\text{C}$ ]
As-deposited (TF)	$13.7 \pm 0.4$	$18.8 \pm 0.4$
After heat treatment (TF)	$12.6 \pm 0.2$	$17.4 \pm 0.4$
Literature value (CG)	12.4	15.7
	Crystallite size $D$ of Ni [nm]	Crystallite size $D$ of Cu [nm]
As-deposited (TF)	37	26
After heat treatment (TF)	59	41

to their state of bonding: their coordination number is less than for bulk atoms. As a consequence different potential curves (potential energy versus interatomic distance; see Figure 8.2) follow. For surface/interface atoms the potential curve shows a less deep minimum well and exhibits a larger asymmetry than for bulk atoms. Due to this

asymmetry the same thermal energy leads to different thermal expansion for surface/interface and bulk atoms. The smaller a crystallite, the larger the ratio of the number of surface/interface atoms and the number of bulk atoms. Thus, the smaller a crystal, the larger its *average* CTE.

#### 8.4. Determination of gradients of effective grain interaction and stress in Cu thin films

The investigation of the depth dependence of effective grain interaction and residual stresses in Cu thin films by XRD is subject of the fourth chapter of the thesis. In order to create a residual stress gradient the deposition parameters were changed during thin film production. The gradients were analysed by XRD measurements at constant penetration depth (for further details about this method and the corresponding limitations see chapter 4.2.1 and Ref. [13]). Thus, for each penetration depth several diffraction lines  $hkl$  were recorded over the corresponding accessible  $\psi$  range. The absorption of the investigated material was adjusted by variation of the X-ray energy,  $E$ , such that a maximum range of penetration depth could be covered. Therefore measurements were performed at a laboratory diffractometer ( $E = 8.048$  kV) and at a synchrotron beamline („Surface Diffraction Beamline“, Ångströmquelle Karlsruhe (ANKA),  $E = 9.996$  kV) (for details of the measurements see chapter 4.3.4). Upon employing small incidence or exit angles ( $< 2,5^\circ$ ) the effect of refraction has to be considered: For an ideally flat surface this effect leads to a change of incidence or exit beam angles and thus to a change of measured diffraction angle. It is thus necessary to correct the measured diffraction angles employing a refraction correction (for details see Ref. [14] and chapter 4.2.2). If the specimen exhibits a certain surface roughness the effect of refraction is reduced, which leads to an overestimation of the refraction-induced error of the measured diffraction angle (see Ref. [15] and chapter 4.2.2).

The evaluation of the measured lattice spacings was performed on the basis of the  $f(\psi, hkl)$  method (see Refs. [16-18] and chapter 4.2.3). Adopting this method it is possible to introduce a weighting parameter,  $w$ , which defines effective X-ray elastic constants (XECs) according to  $S_{1,2}^{hkl} = wS_{1,2}^{hkl,V} + (1-w)S_{1,2}^{hkl,R}$ , where the superscripts „V“ and „R“ denote the Voigt and Reuss models of elastic grain interaction, respectively. Thus, effective XECs can be determined as function of penetration/information depth by least-squares fitting with  $w$  as fit parameter (for further details see chapter 4.2.3).

The Cu thin films (thickness about 4  $\mu\text{m}$ ) were deposited by magnetron sputtering in an ultra-high vacuum chamber onto a thermally oxidised  $\langle 100 \rangle$ -oriented Si wafer (thickness 500  $\mu\text{m}$ ). The first half of the film thickness was deposited at a substrate temperature of 400  $^{\circ}\text{C}$  and subsequently the specimen was cooled to room temperature. Thereafter the second half of the film thickness was deposited. The aim of this two-step deposition process was the creation of a residual stress gradient in the thin film. For further details of the specimen production see chapter 4.3.1.

The investigation of the microstructure employing focused ion beam microscopy revealed that the thin film is composed of columnar and globular grains (see Figure 4.2 in chapter 4.4.1). The surface roughness of the film was investigated by atomic force microscopy and the following roughness values were determined (for details see chapter 4.3.3):  $R_a = 63,9(4)$  nm;  $R_{ms} = 80,9(6)$  nm. This amount of surface roughness reduces the refraction effect, which occurs when small incidence (or exit) angles are employed, such that the application of a refraction correction for small incidence (or exit) angles leads to erroneous results [15].

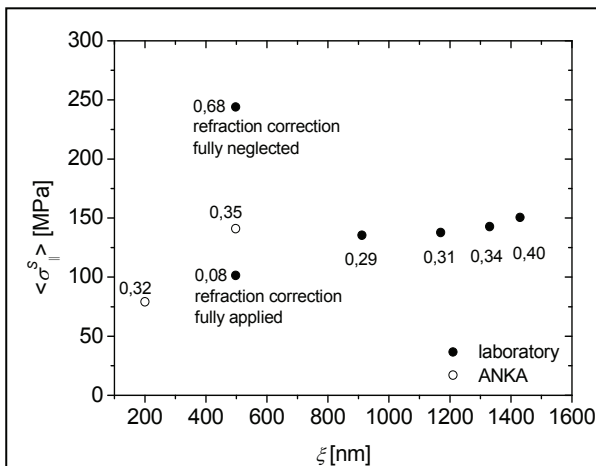


**Figure 8.3.** Mechanical residual stress,  $\langle \sigma_{||}^s \rangle$  (dots), and grain interaction parameter,  $w$  (numbers at the data points) as function of the information depth. The evaluation of the laboratory measurement at the smallest depth was performed twice: fully applying and fully neglecting the refraction correction. Error bars have been omitted as their size is of the order of the symbol size.

In Figure 8.3 the results obtained for the gradients of effective grain interaction and residual stress are shown. It follows that for the specimen investigated both fully applying and fully neglecting the refraction correction for measurements at small incidence angles ( $\xi = 500$  nm) leads to erroneous results for effective grain interaction as well as for residual stress. The reason for this is the above-mentioned surface roughness, which reduces the refraction effect and thus neither corrected nor

uncorrected measurements lead to realistic values. It is thus proposed to avoid small incidence (or exit) angles ( $< 2.5^{\circ}$ ) but rather to adjust absorption by the choice of suitable photon energy such that small penetration depths can be investigated using

large incidence (or exit) angles. For the entire investigated depth range the observed grain interaction is more of Reuss-type than of Voigt-type (Figure 8.3). With decreasing depth the Reuss-type of the grain interaction is even increasing. This can be explained considering the microstructure of the thin film: The microstructure is composed of both columnar and globular grains. For thin films both grain morphologies lead to an increase of the Reuss-character of grain interaction with decreasing distance to the specimen surface (for further details see chapter 4.4.4). Figure 8.3 reveals that the employed two-step deposition process has led to a stress variation from 80 MPa close to the specimen surface to 150 MPa close to the middle of the specimen depth. For further discussion of the depth dependences of grain interaction and residual stress see chapter 4.4.4.

### **8.5. Residual stress and strain-free lattice parameter depth profiles in a $\gamma'$ -Fe<sub>4</sub>N<sub>1-x</sub>-layer**

The variation of residual stress and lattice parameter with specimen depth in a  $\gamma'$ -Fe<sub>4</sub>N<sub>1-x</sub> layer, which was produced by gas nitriding of a  $\alpha$ -Fe substrate is discussed in the fifth chapter of the thesis. As in the preceding chapter XRD stress analysis at constant penetration depth was employed as measurement method. If the XECs of a material are well-known this method additionally allows the determination of the strain-free lattice parameter as function of depth. From the variation of the strain-free lattice parameter the variation of nitrogen concentration can be calculated using a direct relationship between these two figures [19].

The average thickness of the  $\gamma'$  iron nitride layer produced by gas nitriding (for the nitriding parameters see chapter 5.3.1) is 6  $\mu\text{m}$  (for details of the metallographic investigations see chapter 5.3.2). Because during the production process the layer is growing into the substrate, the layer exhibits a flat surface but a rough interface with the substrate.

XRD phase analysis (for details see chapter 5.3.3 and chapter 5.4.1) proved that the produced layer consists exclusively of  $\gamma'$ -Fe<sub>4</sub>N<sub>1-x</sub>. For the analysis of the depth profiles of residual stress and strain-free lattice parameter XRD measurements at constant penetration depth [13] were performed according to the  $\sin^2\psi$  method [18]. Two different wavelengths (measurements at a laboratory diffractometer and at a

synchrotron beamline; for details see chapter 5.3.3) were employed in order to extend the specimen depth range accessible for the investigation.

It was found that the 311 reflection is best suitable for the intended XRD analyses, because the XECs of the 311 lattice planes are least sensitive to a possible variation of grain interaction with depth (see Figure 5.5 in chapter 5.4.2.1).

In order to obtain real-space profiles from the measured Laplace-space profiles an iterative procedure was adopted, which successively approximates the depth profile in real space (for details see chapter 5.2.3). The depth profiles of strain-free lattice parameter and nitrogen concentration, respectively, resulting from the XRD measurements of the 311 reflection at constant penetration depth are shown in Figure 8.4.

The depth profile of the strain-free lattice parameter shows a decrease of the lattice parameter, and thus of the nitrogen concentration, with increasing depth. It is remarkable that the determined nitrogen concentrations close to the surface and at the  $\gamma'/\alpha$  interface agree with calculated nitrogen concentrations adopting local thermodynamic equilibrium [1].

The depth profile of residual stress (see Figure 5.8 in chapter 5.4.2.2)

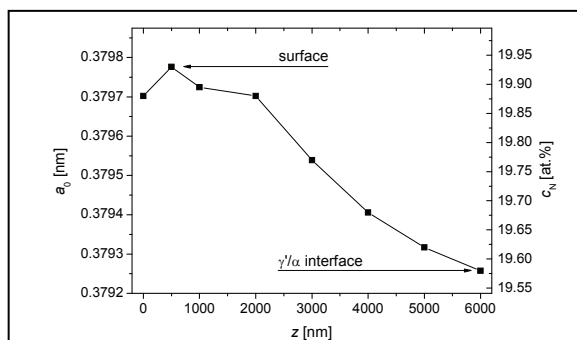


**Figure 8.4.** Real-space depth profile of strain-free lattice parameter and nitrogen concentration, respectively. The arrows mark calculated nitrogen concentrations assuming local thermodynamic equilibrium [1].

generally exhibits compressive residual stresses. These are created as a consequence of the superposition of thermal compressive residual stresses (constant over the layer thickness) and compressive residual stresses which are caused by the nitrogen concentration changing over specimen depth (varying over the layer thickness) [20]. The residual stress shows the following trend over depth:

Firstly, the stress magnitude increases with increasing specimen depth, passes through a maximum and subsequently decreases towards the  $\gamma'/\alpha$  interface. This trend can be explained as follows: Close to the surface stress relaxation takes place due to the formation of pores and (by coalescence of pores) channels along grain boundaries. With increasing specimen depth the residual stress magnitude decreases again due to

the decreasing nitrogen concentration towards the  $\gamma'/\alpha$  interface. For further details about the described depth profiles see chapter 5.4.2.

## **8.6. Application of a collimating single-reflection multilayer optic for X-ray diffraction experiments in parallel-beam geometry**

In the last chapter of the thesis the performance of a special X-ray optic (single-reflection mirror; Xenocs FOX2D CU 12\_INF), which, due to its paraboloidal shape, can collimate a divergent X-ray beam both horizontally and vertically by a single reflection (for details see chapter 6.2.3), are investigated both theoretically (on the basis of ray-tracing calculations) and experimentally (on the basis of measurements of untextured reference samples). The performance is compared to the performance of a Kirkpatrick-Baez (K-B) optic (two serially arranged, mutually rotated by 90°, parabolic X-ray mirrors [21]).

Firstly the primary beam cross sections, divergences and the expected intensity gain of the single-reflection mirror compared to the K-B optic were determined theoretically (see chapter 6.3). An increase in photon flux by a factor of approximately 4 in favour of the single-reflection mirror (equation 6.2; without employing additional primary beam collimators) at a comparable beam divergence has been obtained.

In the experimental part the performance of the single-reflection mirror used with a parallel beam diffractometer (Bruker AXS D8 Discover, for details see chapter 6.4) was extensively studied and compared to the performance of a K-B optic. Therefore the cross section of the primary beam was visualized employing an X-ray camera and its divergence adopting the single-reflection mirror was measured by rocking curves of the reflection of a single-crystalline silicon specimen. Subsequently, the intensity of the diffracted signal from an  $\text{Al}_2\text{O}_3$  standard specimen resulting from the single-reflection mirror was compared to the intensity resulting from the K-B optic. It followed that at comparable beam divergence and similar beam cross section the intensity of the diffracted signal using the single-reflection mirror is by a factor of 14 to 20 larger than the intensity using the K-B optic (see chapter 6.5.1 and chapter 6.5.2).

Moreover, the instrumental aberrations (dependence of shape and intensity of diffraction lines on the orientation of the diffraction vector) of the parallel-beam diffractometer equipped with the single-reflection mirror were investigated employing a texture-free tungsten standard powder specimen (for theory see chapter 6.2.2). It followed that, as for the parallel-beam geometry theoretically expected (see also Ref. [22]), all peak parameters describing the shape of a diffraction line are independent of the orientation of the diffraction vector with respect to the specimen frame of reference (see Figure 6.12 and Figure 6.13 in chapter 6.5.3.1) and the theoretically expected dependence of the intensity of a measured diffraction line from the tilt angle between the diffraction vector and the specimen surface normal is obtained (see also Ref. [22] and chapter 6.5.3.2).

A discussion firstly focused on a comparison of results obtained by simulations and experiments. It followed that both calculated beam cross section and divergence match very well with the according measured characteristics. The experimentally determined intensity gain surpasses the theoretically calculated gain. This can be explained on the one hand by the fact that single-reflection mirror and K-B optic are not – as assumed in the calculations – composed of the same material and on the other hand by different aging conditions of both optics.

## References/Literatur

- [1] Mittemeijer, E.J. & Somers, M.A.J. (1997). *Surf. Eng.* **13**, 483.
- [2] Lehrer, E. (1930). *Z. Elektrochem.* **36**, 383.
- [3] Fernández Guillermet, A. & Du, H. (1994). *Z. Metallkd.* **85**, 154.
- [4] Lehrstuhl für Theoretische Hüttenkunde RWTH Aachen (1999). Editors.  
*Thermodynamic Properties of Inorganic Materials compiled by SGTE*, Berlin: Springer.
- [5] Lehrstuhl für Theoretische Hüttenkunde RWTH Aachen (1999). Editors.  
*Thermodynamic Properties of Inorganic Materials compiled by SGTE*, Berlin: Springer.
- [6] Kooi, B.J., Somers, M.A.J. & Mittemeijer, E.J. (1996). *Metall. Mater. Trans. A* **27A**, 1063.
- [7] Porter, D.A. & Easterling, K.E. (2001). *Phase Transformations in Metals and Alloys*. Cheltenham, UK: Nelson Thornes.
- [8] Harada, J. & Oshima, K. (1981). *Surf. Sci.* **106**, 51.

- [9] Lee, J.-G. & Mori, H. (2005). *Eur. Phys. J. D* **34**, 227.
- [10] Fang, W. & Lo, C.-Y. (2000). *Sensor Actuat. A-Phys.* **84**, 310.
- [11] Touloukian, Y. S., Kirby, R. K., Taylor, R. E. & Desai, P. D. (1975). *Thermal Expansion, Metallic Elements and Alloys*. New York: IFI/Plenum.
- [12] Altman, H.W., Rubin, T. & Johnston, H.L. (1954). *Cryogenic Laboratory Report OSU-TR-267-27*. Ohio State University. Columbus, OH.
- [13] Kumar, A., Welzel, U. & Mittemeijer, E. J. (2006). *J. Appl. Cryst.* **39**, 633.
- [14] Genzel, C. (2005). *Mater. Sci. Technol.* **21**, 10.
- [15] Ott, M. H. & Löhe, D. (2002). *Mater. Sci. Forum* **404-407**, 25.
- [16] Quaeyhaegens, C., Knuyt, G. & Stals, L. M. (1995). *Surf. Coat. Technol.* **74-75**, 104.
- [17] Kamminga, J.-D., de Keijser, Th. H., Mittemeijer, E.J. & Delhez, R. (2000). *J. Appl. Cryst.* **33**, 1059.
- [18] Welzel, U., Ligot, J., Lamparter, P., Vermeulen, A.C. & Mittemeijer, E.J. (2005). *J. Appl. Cryst.* **38**, 1.
- [19] Somers, M.A.J., van der Pers, N.M., Schalkoord, D. & Mittemeijer, E.J. (1989). *Metall. Trans. A* **20A**, 1533.
- [20] Somers, M. A. J. & Mittemeijer, E. J. (1990). *Metall. Trans. A* **21A**, 189.
- [21] Schuster, M. & Göbel, H. (1995). *J. Phys. D* **28**, A270.
- [22] Welzel, U. & Leoni, M. (2002). *J. Appl. Cryst.* **35**, 196.



## List of publications

1. Wohlschlägel, M., Welzel, U., Maier, G. & Mittemeijer, E. J. (2006). Calibration of a heating/cooling chamber for X-ray diffraction measurements of mechanical stress and crystallographic texture, *J. Appl. Cryst.* **39**, 194.
2. Wohlschlägel, M., Baumann, W., Welzel, U. & Mittemeijer, E.J. (2006). Mechanical stress gradients in thin films analyzed employing X-ray diffraction measurements at constant penetration/information depths, *Mater. Sci. Forum* **524-525**, 19.
3. Sobiech, M., Wohlschlägel, M., Welzel, U., Mittemeijer, E.J., Leineweber, A., Hügel, W. & Kirchner, V. (2006). Investigation of mechanical stress gradients of Sn thin films, *HasyLab Annual Report* **1**, 591.
4. Kuru, Y., Chakraborty, J., Welzel, U., Wohlschlägel, M. & Mittemeijer, E.J. (2006). Interdiffusion and Stress Development in Thin Film Diffusion Couples, *Mater. Sci. Forum* **524-525**, 801.
5. Kumar, A., Welzel, U., Wohlschlägel, M., Baumann, W. & Mittemeijer, E.J. (2006). An X-ray diffraction method to determine stress at constant penetration/information depth, *Mater. Sci. Forum* **524-525**, 13.
6. Majewski, P., Roy Choudhury, N., Spori, D., Wohlfart, E. & Wohlschloegel, M. (2006). Synthesis and characterisation of star polymer / silicon carbide nanocomposites, *Mater. Sci. Eng. A* **434**, 360.
7. Wohlschlägel, M., Welzel, U. & Mittemeijer, E.J. (2007). Unexpected formation of  $\epsilon$ -Fe<sub>3</sub>N<sub>1+x</sub> by gas nitriding of  $\alpha$ -Fe thin films, *Appl. Phys. Lett.* **91**, 141901. Chapter 2 of the thesis.
8. Wohlschlägel, M., Schüllli, T.U., Maier, G., Welzel, U. & Mittemeijer, E.J. (2007). Characterization of a high performance laboratory parallel-beam diffractometer – bridging the gap to the synchrotron, *Z. Kristallogr. Suppl.* **26**, 147.
9. Kuru, Y., Wohlschlägel, M., Welzel, U. & Mittemeijer, E. J. (2007). Crystallite size dependence of the coefficient of thermal expansion of metals, *Appl. Phys. Lett.* **90**, 243113. Chapter 3 of the thesis.
10. Gressmann, T., Wohlschlägel, M., Shang, S., Welzel, U., Leineweber, A., Mittemeijer, E.J. & Liu, Z.-K. (2007). Elastic anisotropy of  $\gamma'$ -Fe<sub>4</sub>N and elastic

grain interaction in  $\gamma'$ -Fe<sub>4</sub>N<sub>1-y</sub> layers on  $\alpha$ -Fe: First-principles calculations and diffraction stress measurements, *Acta Mater.* **55**, 5833.

11. Wohlschlägel, M., Schüllli, T.U., Lantz, B. & Welzel, U. (2008). Application of a single-reflection collimating multilayer optic for X-ray diffraction experiments employing parallel-beam geometry, *J. Appl. Cryst.* **41**, 124. Chapter 6 of the thesis.
12. Kuru, Y., Wohlschlägel, M., Welzel, U. & Mittemeijer, E.J. (2008). Coefficients of thermal expansion of thin metal films investigated by non-ambient X-ray diffraction stress analysis, *Surf. Coat. Technol.* **202**, 2306.
13. Kuru, Y., Wohlschlägel, M., Welzel, U. & Mittemeijer, E.J. (2008). Non-ambient X-ray diffraction residual stress analysis of thin films: tracing nanosize-related effects on thermoelastic constants and identifying sources of residual stresses, *J. Appl. Cryst.* **41**, 428.
14. Kuru, Y., Wohlschlägel, M., Welzel, U. & Mittemeijer, E.J. (2008). Interdiffusion and stress development in Cu-Pd thin film diffusion couples, *Thin Solid Films* **516**, 7615.
15. Wohlschlägel, M., Welzel, U. & Mittemeijer, E.J. (2008). Residual stress and strain-free lattice-parameter depth profiles in a  $\gamma'$ -Fe<sub>4</sub>N<sub>1-x</sub> layer on an  $\alpha$ -Fe substrate measured by X-ray diffraction stress analysis at constant information depth, *J. Mater. Res.* submitted. Chapter 5 of the thesis.
16. Wohlschlägel, M., Baumann, W., Welzel, U. & Mittemeijer, E.J. (2008). Determination of depth gradients of grain interaction and stress in Cu thin films, *J. Appl. Cryst.* submitted. Chapter 4 of the thesis.

# Danksagung

Die vorliegende Arbeit wurde am Institut für Metallkunde der Universität Stuttgart und am Max-Planck-Institut für Metallforschung, Stuttgart, angefertigt. An dieser Stelle möchte ich all denen danken, die zum Gelingen der Arbeit beigetragen haben.

An erster Stelle möchte ich Herrn Prof. Dr. Ir. E. J. Mittemeijer dafür danken, dass er mich in seine Abteilung aufgenommen hat, mir dieses überaus interessante Thema überlassen hat und mich stets mit seinem Vertrauen bestärkte. Sein außergewöhnliches Engagement bei der Betreuung der Arbeit durch die regelmäßigen wissenschaftlichen Diskussionen und durch seine stetige Bereitschaft zum freien Gedankenaustausch haben maßgeblich zum Erfolg der Arbeit beigetragen.

Herrn Prof. Dr. F. Aldinger danke ich für die freundliche Übernahme des Mitberichts, sowie Herrn Prof. Dr. E. Roduner für die Bereitschaft den Prüfungsvorsitz zu übernehmen.

Besonders herzlich möchte ich mich bei meinem täglichen Betreuer, Herrn Dr. Udo Welzel, für die uneingeschränkte Unterstützung und Förderung sowie für die unzähligen wissenschaftlichen Diskussionen bedanken. Sein wertvoller Rat und sein breites Fachwissen waren unerlässliche Wegbereiter der vorliegenden Arbeit.

Allen Mitarbeitern des Max-Planck-Instituts für Metallforschung, insbesondere den Kollegen der Abteilung Mittemeijer, gilt mein herzlicher Dank für die vertrauensvolle Zusammenarbeit und die angenehme Arbeitsatmosphäre. Namentlich möchte ich mich bei Dr. Yener Kuru und Wolfgang Baumann für die Zusammenarbeit, sowie bei Ute Schestag für die Unterstützung bei speziellen Computerproblemen bedanken.

Nicht zuletzt möchte ich mich besonders herzlich bei meinen Eltern, sowie bei meiner Freundin Elisabeth für den starken persönlichen Rückhalt bedanken.



# Curriculum Vitae

## Persönliche Daten

Name	Markus Albin Wohlschlögel
Geburtsdatum	17.04.1979
Geburtsort	Frankfurt/M.
Staatsangehörigkeit	deutsch

## Schulbildung

1985 – 1989	Grundschule Hösbach
1989 – 1998	Hanns-Seidel-Gymnasium Hösbach
	Abschluß: Abitur

## Hochschulbildung

1999 – 2004	Studium der Werkstoffwissenschaft an der Universität Stuttgart
08/2004 – 01/2005	Diplomarbeit am Institut für Metallkunde, Lehrstuhl I, Universität Stuttgart Thema: „Kalibrierung einer Heiz-/Kühlkammer für Röntgenbeugungsmessungen; Kornwechselwirkung in dünnen Schichten“ Hauptberichter: Prof. Dr. Ir. E.J. Mittemeijer
01/2005	Abschluß: Diplom-Ingenieur

## Promotion

2005 – 2008	Max-Planck-Institut für Metallforschung, Stuttgart und Institut für Metallkunde, Universität Stuttgart Thema: „Microstructural effects on stress in thin films“ Hauptberichter: Prof. Dr. Ir. E.J. Mittemeijer
-------------	---